Quantum Mechanical Investigations of Adsorbate Interactions inside Nanopores of 2D Poly(heptazine imide) Salts and a Novel Approach for Calculating Transport Coefficients

Doktorarbeit (Dr. rer. nat.)
dem Department Chemie der Fakultät für Naturwissenschaften
der Universität Paderborn
vorgelegt von

Julian Joachim Heske
Matrikelnummer: 701 20 32

Paderborn, den 17.05.2022

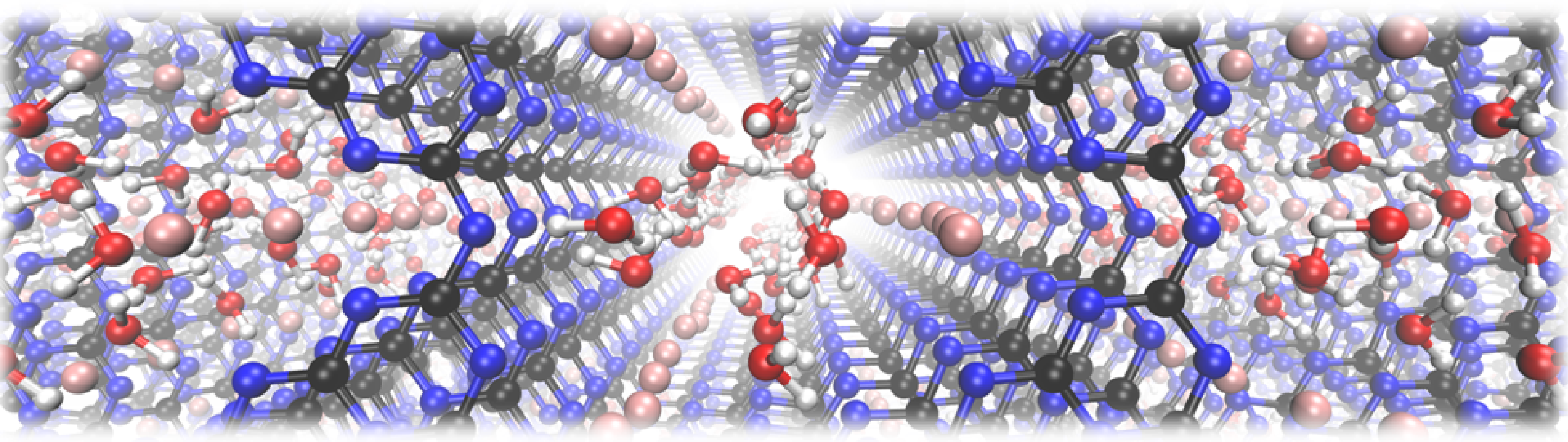

Bearbeitungszeitraum: 01.05.2019 - 17.05.2022

Betreuer:

Prof. Dr. Thomas D. Kühne
Universität Paderborn, Paderborn

Prof. Dr. Dr. h.c. Markus Antonietti
Max-Planck-Institut für Kolloid-
und Grenzflächenforschung, Potsdam

Eidesstattliche Erklärung

Hiermit versichere ich, dass ich die vorliegende Arbeit selbstständig verfasst und keine anderen als die angegebenen Quellen und Hilfsmittel benutzt habe. Alle Ausführungen, die fremden Quellen wörtlich oder sinngemäß entnommen wurden, sind kenntlich gemacht. Die Arbeit war in gleicher oder ähnlicher Form noch nicht Bestandteil einer Studien- oder Prüfungsleistung.

Paderborn, den 17. Mai 2022 Julian Joachim Heske

Zusammenfassung

Kaliumpoly(heptazinimid) (K-PHI) ist ein vielversprechender Photokatalysator für verschiedene chemische Reaktionen. Die Ladungstrennung zwischen den Kationen innerhalb der Nanoporen eines anionischen zweidimensionalen Kohlenstoffnitridgerüsts führt zu einer spannenden Adsorptionsumgebung für verschiedene Adsorbate. In dieser Arbeit werden Berechnungen auf der Grundlage der Dichtefunktionaltheorie durchgeführt, um die Struktur und die Adsorptionseigenschaften von K-PHI und seinen kationenausgetauschten Analoga, X-PHI, zu untersuchen. Diese Materialien sind mögliche Kandidaten für die Heliumspeicherung, da sich die Heliumadsorption in allen untersuchten Systemen als thermodynamisch günstig erweist (bis zu ΔE_{ads}=-5,5 kJ/mol in Cs-PHI). Außerdem wurde eine bemerkenswerte Adsorptionsenergie von ΔE_{ads}=-95 kJ/mol für ein einzelnes Wassermolekül in K-PHI gefunden und ΔE_{ads}=-83 kJ/mol pro H_2O bei maximaler Wasseraufnahme (14 wt%). Diese Wechselwirkungen gehen über die typische Physisorption hinaus und haben ihren Ursprung in der Tatsache, dass Wasser an Kaliumionen koordiniert ist und gleichzeitig Wasserstoffbrückenbindungen mit den negativen PHI-Schichten in den begrenzten Nanoporen von K-PHI bildet. Die Wichtigkeit der Ladungstrennung in den Nanoporen der Materialien wird für beide Adsorbate durch die berechneten atomaren Nettoladungen und die Energiezerlegungsanalyse bestätigt. Neben der dominierenden Coulomb-Wechselwirkung trägt auch der Ladungstransfer erheblich zu diesen Wechselwirkungen bei. Da zu erwarten ist, dass Wasser bereits bei niedrigen Partialdrücken adsorbiert, wird der Einfluss von Wasseranwesenheit auf die Heliumadsorption untersucht. Interessanterweise ist die Heliumadsorptionsaffinität durch Wassermoleküle auf bestimmten Adsorptionsplätzen leicht erhöht, jedoch verschwindet die Verbesserung bei höheren Aufnahmen schnell aufgrund der Konkurrenz um die Adsorptionsplätze auf dem begrenzten Raum. Daher weisen PHI-Materialien interessante Eigenschaften und ein großes Potenzial für verschiedene Anwendungen auf, bei denen extreme Wechselwirkungen zwischen Adsorbat und Adsorptionsmittel erwünscht sind, wie z. B. bei der Adsorbataktivierung in der Katalyse.

Abstract

Potassium poly(heptazine imide) (K-PHI) is a promising photocatalyst for various chemical reactions. The charge separation between cations within the nanopores of an anionic two-dimensional carbon nitride framework yields an exciting adsorption environment for various adsorbates. In this work, density functional theory-based calculations are employed to study the structure and adsorption properties of the K-PHI and their cation exchanged analogues, X-PHI. These materials are possible candidates for helium storage as helium adsorption is found to be thermodynamically favorable in all studied systems (up to ΔE_{ads}=-5.5 kJ/mol in Cs-PHI). Furthermore, a remarkable adsorption energy of ΔE_{ads}=-95 kJ/mol was found for a single water molecule in K-PHI and ΔE_{ads}=-83 kJ/mol per H_2O at maximum water uptake (14 wt%). This interactions are beyond typical physisorption and originate from water being coordinated to potassium ions and at the same time forming hydrogen bonds with the negative PHI layers in the confined nanopores of K-PHI. The importance of charge separation inside the nanopores of the materials are confirmed for both adsorbates by calculated net atomic charges and energy decomposition analysis. Beside dominating Coulomb interaction, charge transfer also contributes significantly to these interactions. As water is expected to be adsorbed already at low partial pressures, the impact of water presence on the helium adsorption is investigated. Interestingly, water molecules on specific adsorption sites slightly increase the helium adsorption affinity, however, the enhancement quickly vanishes at higher uptakes due to competition for the adsorption sites in the confined space. Hence, PHI materials exhibit interesting properties and a huge potential for various applications where extreme interactions between adsorbate and adsorbent are desired, such as for adsorbate activation in catalysis.

Contents

1 Introduction

Carbon nitride (CN) materials with different stoichiometric compositions have been known for a long time [1], however, they attracted emerging attention in the scientific community in the recent years. Because of their versatile properties combined with cost efficiency, they are suitable candidates for a wide range of applications in catalysis [2–6], gas storage [7] and battery research [8–10]. Two-dimensional carbon nitrides exhibit outstanding photocatalytic properties [11–13]. For example, graphitic carbon nitrides (g-C_3N_4) are shown to be efficient photocatalysts. Due to their bandgap of 2.7 eV corresponding to a wavelength absorption threshold of 460 nm and a suitable conduction band potential, they are especially able to perform water reduction [3, 14, 15], but also other photocatalytic reactions [16–18]. Moreover, CN materials can store electrons in a long-lived photoreduced state [19–21], which allows a temporal separation of light adsorption and the catalytic conversion under dark conditions (”dark photocatalysis” [19]) and also make them a candidate for solar batteries [22].

Recently, a novel type of porous two-dimensional CN materials, poly(heptazine imides) (PHI), was synthesized. Due to their metastability, improved conductivity and high crystallinity, the hydrogen evolution reaction (HER) rates reach up to four times higher than those of the mesoporous g-C3N4 [23, 24]. Furthermore, it is not only interesting for HER, but due to a higher valence band potential than other carbon nitrides, it is also capable of photocatalytic water oxidation in the absence of any-metal based co-catalyst under visible light [25]. These PHI materials can be synthesized ionothermally with either starting from the melon polymer [12, 26] or by condensation of well-organized molecular precursors [23, 24]. In all cases, the usage of salt melts seems to be crucial and yields different products as obtained by high-temperature solid-state synthesis [12, 23, 24, 26]. The structure of the potassium containing PHI salt, K-PHI, has been studied by various experimental techniques [23]. K-PHI contains an extended planar network out of tri-s-triazine (heptazine) units connected via imide bridges and intercalated potassium ions.

The chemical structure of a defect-free K-PHI layer is shown in Fig. 1.1. The PHI layers exhibit a tight packing in these materials with an interlayer distance of 0.32 nm [23]. The potassium ions in K-PHI are located in channels that are different from the PHI layers, which means that the cations are organized inside the pores by means of ionic self assembly [27]. This charge separation between the negative organic framework and the positive ions inside these materials is one of their exciting features.

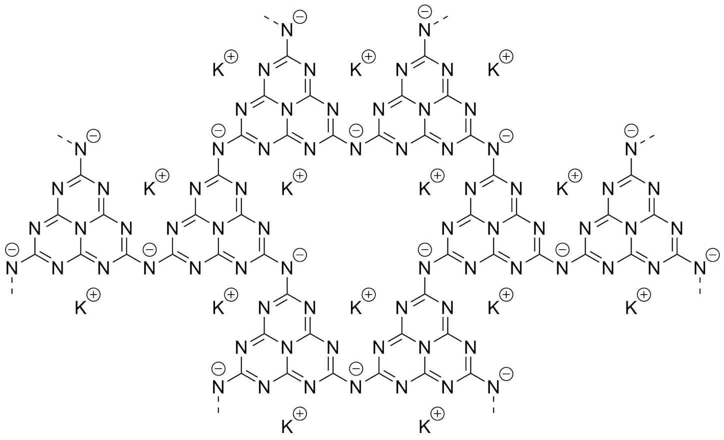

Figure 1.1: Idealized structure of the two-dimensional K-PHI, where the potassium ions are in the pores of the CN framework

K-PHI was the first synthesized PHI salt which was directed by choice of the eutectic salt melt (LiCl/KCl) as reaction medium. However, Savateev *et al.* [23] demonstrated that the potassium ions inside K-PHI can be exchanged with other cations while essentially preserving the crystal structure of the materials, which allows to tune their properties post-synthetically. This exchange with other cations ($X^{+/2+}$) is schematically shown in Fig. 1.2, where the CN framework remains unchanged. The authors obtained a wide range of different PHI salts containing alkali (Li, Na, Cs), alkaline earth (Mg, Ca) and transition metals (Ni, Co, Ag, Zn) and further studied their catalytic reactivity and conductivity. The highest photocatalytic activity for the visible-light-driven hydrogen evolution reaction was found in the case of the Mg-PHI salt. The fact that the cations can be easily exchanged in these materials is not trivial. Insertion and exchange of ions in solid-state porous crystalline frameworks are usually possible rather in inorganic frameworks. Examples are the redox intercalation of Li-ions into CoO_2 as happening at the cathode of a lithium battery [28, 29] and the exchange of ions within a charged zeolite framework changing its catalytic activity and size selectivity [24]. In organic frameworks, ion insertion or exchange are rare and primarily based on extended polymer frameworks [30]. Therein, the solubility of the materials in salt melts as well as the strength of interaction with the salt ions play a crucial role. Hence, the salt melt acts as a high-temperature solvent and as a structure-directing agent [31–33]. The choice of the ion define the structure, crystallinity and hence the properties of the resulting materials [24]. In the case of a similar material, poly(triazine imide) (PTI), divalent metal ions like Sn stay inside the final polymer because they exhibit strong nitrogen-metal donor acceptor bonds [34, 35].

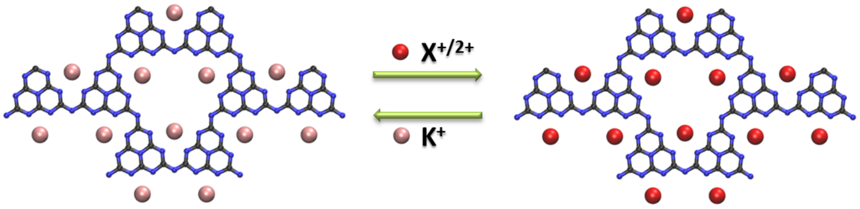

Figure 1.2: Schematic exchange of the potassium (K^+; pink) cations of K-PHI with other cations ($X^{+/2+}$; red) while maintaining the organic framework along the lines of Ref. [23].

The focus of this work is the theoretical investigation of the interaction of adsorbates inside the nanopores of the poly(heptazine imide) salts. As these materials exhibit structures which offer an interesting adsorption evironment, they are potentially relevant for gas storage, separation, catalysis and many more. It has already been demonstrated that hydrogen gas (H_2) adsorbs on metal-free CN materials [7]. Since H_2 is non-polar and quickly boiling, it usually has to be activated, e. g. in terms of frustrated Lewis pairs in pure organic systems [36–39]. Therefore, K–PHI could be a suitable candidate for non-polar gas adsorption. The most non-polar gas is helium, which has an extremely low boiling point ($\sim$4 K), and liquefying He gas is technologically demanding. Adsorption materials offer an alternative for storage and transportation of He gas. Hence, helium adsorption in K-PHI is investigated in this work. Present adsorption materials usually exhibit only little He adsorption because of its inertness and low solubility [40–45]. High helium uptake was found in magnetron sputtering generated nanoporous silicon [46] and similar obtained titanium alloy films [47] with storage of up to 21 at%.

Beside the extreme non-polar helium, the water adsorption in the highly reactive nanopores of K-PHI is addressed in this work. Interactions between water molecules and surfaces are among the most fundamental and relevant phenomena [48, 49]. Water is omnipresent and essential for example for living organisms [50] and modern energy- and environmental applications, such as gas adsorption, catalysis or adsorptive purification. [51–53] In these applications, the structure and activation of water at the interfaces play a crucial role. Strong interface interactions or confined conditions in the pore can realign the water structure and hence completely change its nature and properties [54]. K-PHI exhibits a definite pore size, high availability of partial charges and hydrophilic sites. Therefore, it is interesting to investigate the structure and thermodynamics of water at these interfaces.

The remainder of this work is organized as follows. In Chapter 2, the theoretical framework is given by briefly explaining the fundamentals of density functional theory as well as the applied energy decomposition analysis based on absolutely localized orbitals. Next, the structure of K-PHI and the cation exchange of K-PHI to other PHI salts and their structures are investigated in Chapter 3. In Chapter 4, the helium adsorption in these materials is studied with a focus on the interactions between adsorbate and PHI material as well as the role of the cation. The interactions of single and multiple adsorbed water in the nanopores of K-PHI is similarly investigated in Chapter 5. This is followed by a discussion about the interplay between water and helium in K-PHI in Chapter 6. After that, the development of an alternative approach for calculating transport coefficients is described and applied to disordered silicon in Chapter 7, which was done as a collaboration with Prof. Emil V. Prodan and Prof. Thomas D. Kühne and published in Ref. [55]. There, E. V. P. and T. D. K. developed the theoretical framework in Section 7.1, 7.2 and 7.3 as well as the implementation (Section 7.4). My contribution to this work is the application (Section 7.5) of the theory to ab-initio molecular dynamics simulations of silicon containing different numbers of atoms (216 and 1000) at different temperatures (300, 600, 900, 1200, 1500, 1800, 2100, 2400, 2700, 3000K). More precisely, I generated workflows for these different systems to calculate the overlap matrices S and the Kohn Sham matrices H_{KS} and calculate the chemical potential as well as the conductivity from these. At the end, Chapter 8 deals with the conclusions of the previous chapters followed by the references and the appendix.

2 Description of a Quantum Mechanical System

This chapter deals with the fundamentals of density functional theory (DFT) starting from the Schrödinger equation (SE). The explanation and the equations are mostly based on Ref. [56] and Ref. [57], however, there are plenty of additional well-written summaries in the literature [58–61]. After that, the energy decomposition analysis (EDA) based on absolutely localized orbitals (ALMO) is briefly introduced, which is used in this work to decompose the DFT interaction energies of adsorbates to gain further chemical insights.

2.1 Schrödinger Equation and Born-Oppenheimer Approximation

To describe a physical system quantum mechanically, most approaches are based on the time-independent, non-relativistic Schrödinger equation [62, 63]

$$\hat{H}\Psi_i(r_1,...,r_N,R_1,...,R_M) = E_i\Psi_i(r_1,...,r_N,R_1,...,R_M), \tag{2.1.1}$$

where $\hat{H}$ is the Hamilton operator for a physical system consisting of M nuclei and N electrons. The wavefunction of the system Ψ completely describes the quantum mechanical system and contains all information which can be known. Subindex i denotes the state of the system and E_i are the corresponding energies. In the absence of magnetic or electric fields, the Hamiltonian

$$\hat{H} = \hat{T}_{nuc} + \hat{T}_{elec} + \hat{V}_{nuc-nuc} + \hat{V}_{nuc-elec} + \hat{U}_{elec-elec} \tag{2.1.2}$$

represents the total energy by the sum of the kinetic energies of electrons T_{elec} and nuclei T_{elec} plus the pair potential potentials $\hat{V}_{nuc-nuc}$,$\hat{V}_{nuc-elec}$ and $\hat{U}_{elec-elec}$.

The Born-Oppenheimer approximation [64] separates the Schrödinger equation into nuclear and electronic contributions, which simplifies the problem enormously. Pictorially, the electrons are assumed to move in a field of fixed nuclei. This is a reasonably good approximation due to the significant mass differences between nuclei and electrons. For the lightest atom of all, hydrogen, the nucleus, which is a single proton, is about 1800 times heavier than its electron and their movements are hence happening on different time scales. For all other atoms, the difference is even multiple times higher. In the electronic SE, the kinetic energy of the nuclei is neglected and as a consequence the total kinetic energy is only determined by the kinetic energy of the electrons T_{elec}. The nuclear repulsion is only a constant and not part of the electronic Hamiltonian. The electronic Hamiltonian then only consists of

$$\hat{H}_{elec} = \hat{T}_{elec} + \hat{V}_{nuc-elec} + \hat{U}_{elec-elec}. \tag{2.1.3}$$

Using DFT, one is usually interested in the electronic structure of atoms, molecules and solids. Its goal is to address the many-body electronic Schrödinger equation

$$\hat{H}_{elec}\Psi_{elec}(r_1, ..., r_N; R_1, ..., R_M) = E_{elec}\Psi_{elec}(r_1, ..., r_N; R_1, ..., R_M), \tag{2.1.4}$$

where the electronic wavefunction Ψ_{elec} now only depends on the N electronic coordinates r_i while the M nuclear coodinates R_k enter only parametrically. The nuclear repulsion

$$E_{nuc} = \sum_{k<l} \frac{Q_k Q_l}{|R_k - R_l|}, \tag{2.1.5}$$

where Q_k and Q_l are the charges of nuclei k and l, respectively, is only a constant and can simply be added to the electronic energy E_{elec} to obtain the total energy of the system

$$E_{tot} = E_{elec} + E_{nuc}. \tag{2.1.6}$$

From now on, only the electronic part of the SE is considered and the subindices are dropped, so that the electronic SE is given as

$$[\hat{T} + \hat{V} + \hat{U}]\Psi(r_1, ..., r_N; R_1, ..., R_M) = E\Psi(r_1, ..., r_N; R_1, ..., R_M), \tag{2.1.7}$$

where the electronic Hamiltonian consists of three parts: First, the electronic kinetic energy $\hat{T}$, which is for any non-relativistic system defined as

$$\hat{T} = -\frac{\hbar^2}{2m}\sum_{i}^{N}\nabla_i^2, \tag{2.1.8}$$

where $\hbar$, m and ∇ are the reduced planck constant, the mass of the electron and the nabla operator, respectively, and secondly $\hat{U}$ which describes the Coulomb interactions of electrons by

$$\hat{U} = \sum_{i<j} U(r_i, r_j) = \sum_{i<j} \frac{q^2}{|r_i - r_j|}, \tag{2.1.9}$$

where q is the charge of an electron. As can be seen, the operators $\hat{T}$ and $\hat{U}$ do not depend on the system and are hence called universal operators. Contrary, the only system dependent (non-universal) operator is

$$\hat{V} = \sum_{i} v(r_i) = \sum_{ik} \frac{Q_k q}{|r_i - R_k|} \tag{2.1.10}$$

which describes the attractive potential exerted on electrons due to the nuclei and its expectation value v(r) is often termed as external potential. The SE for a single electron moving in this potential v(r)

$$\left[-\frac{\hbar^2\nabla^2}{2m} + v(r)\right]\Psi(r) = \varepsilon\Psi(r) \tag{2.1.11}$$

and the many-body SE

$$\left[\sum_{i}^{N}\left(-\frac{\hbar^2\nabla_i^2}{2m} + v(r)\right) + \sum_{i<j} U(r_i, r_j)\right]\Psi(r_1, ..., r_N) = E\Psi(r_1, ..., r_N) \tag{2.1.12}$$

for a system containing multiple electrons can be formulated. The approach is to first specify the system by choosing the potential v(r), constructing the Hamiltonian $\hat{H}$ and obtain the electronic wavefunction Ψ by solving that linear partial differential equation. Knowing the wavefunction, any physical observable O can be calculated as an expectation value ⟨O⟩ with the corresponding operator Ô via

$$\langle\Psi|\hat{O}|\Psi\rangle = \int d^3r_1 \int d^3 ... \int d^3r_N \Psi^*(r_1, r_2, ..., r_N)\hat{O}\Psi(r_1, r_2, ..., r_N) \tag{2.1.13}$$

The schematic procedure can be summed up as

$$v(r) \Rightarrow \hat{H} \xrightarrow{H\Psi=E\Psi} \Psi(r_1, ..., r_N) \xrightarrow{\langle\Psi|\hat{O}|\Psi\rangle} \langle O\rangle. \tag{2.1.14}$$

The wave function itself is not an observable. A physical interpretation is only possible of the electron density, which is related to the square modulus of the wavefunction and is defined as the integral over all but one spatial variables of the electrons. The result is formally the probability of finding a particular electron within a volume element dr_1 - while all other electrons might be anywhere in space. However, because electrons are indistinguishable, it is also the probability of finding any other electron within dr_1. In practice, wave functions are often normalized so that the probability of finding the N electrons anywhere in space is equal to 1. Hence, you get the total probability

$$\rho(r) = N \int d^3r_2 \int d^3 ... \int d^3r_N \Psi^*(r, r_2, ..., r_N)\Psi(r, r_2, ..., r_N) \tag{2.1.15}$$

of finding any electron by multiplication with the total number of electrons N.

2.2 Density Functional Theory

As described in the previous section, obsevables can be calculated using the wavefunction Ψ. Unlike other methods, density functional theory (DFT) defines a way to calculate observables by only using the electron density $\rho(r)$ as key quantity without needing the wavefunction explicitly. This reduces the effort significantly and is the reason for the emergence of DFT. It means that in a closed shell system, the information of $\Psi_0(r_1, ..., r_N)$ depending on N vectorial variables, i. e. 3N coordinates, is contained in the ground state density $\rho_0(r)$, which only depends on one vector r with 3 spatial dimensions. Its legitimacy was shown by Hohenberg and Kohn in 1961 [65]. Nowadays, their evidences are known as the Hohenberg-Kohn theorems.

Hohenberg-Kohn Theorem 1

The first Hohenberg-Kohn theorem proves that the external potential $v(r)$ is (to within a constant) a unique functional of $\rho(r)$. Hence, the ground-state electron density $\rho_0(r)$ indeed uniquely determines the complete Hamilton operator and it is in principle possible to calculate the ground state wavefunction

$$\Psi_0(r_1, ..., r_N) = \Psi_0[\rho_0(r)] \tag{2.2.1}$$

as a functional of $\rho_0(r)$. As a consequence, all properties of the system can also be calculated and are given by the expectation value of its operator $\hat{O}$:

$$O_0 = O[\rho_0] = \langle \Psi[\rho_0] | \hat{O} | \Psi[\rho_0] \rangle. \tag{2.2.2}$$

Noteworthy, although density functional theory is a ground state theory, by having the complete Hamilton operator, all states including the excited states of the system are formally determined by the ground state density $\rho_0(r)$.

Hohenberg-Kohn Theorem 2

The second Hohenberg-Kohn theorem shows that the most important observable, the ground state density

$$E_{v,0} = E_v[\rho_0] = \langle \Psi[\rho_0] | \hat{H} | \Psi[\rho_0] \rangle \tag{2.2.3}$$

can be obtained by applying the variational principle. Every energy $E[\rho']$ is higher or equal to the energy of the ground state density. The lowest energy is obtained if the density is the true ground state density.

$$E_v[\rho_0] \leq E_v[\rho'] \tag{2.2.4}$$

For calculating the ground state energy, the universal energy functional $T[\rho]$ and $U[\rho]$ can be used, which are the expectation values of $\hat{T}$ and $\hat{U}$. Hence, a non-relativistic Coulomb system only differs by their potential v(r), which is the expectation value of

$$V[\rho] = \int d^3 r \rho(r) v(r) \tag{2.2.5}$$

If the system is defined and v(r) is known, the energy in this potential is

$$E_v[\rho] = T[\rho] + U[\rho] + V[\rho] = T[\rho] + U[\rho] + \int d^3r\rho(r)v(r). \tag{2.2.6}$$

The theorems form the theoretical foundation of DFT, however, $T[\rho]$ and $U[\rho]$ are still unknown and the theorems do not provide any practical information on how these functionals actually look like.

2.3 Thomas-Fermi Model

Even before the Hohenberg-Kohn theorems, the first energy functional was given based on a description of Thomas [66] and Fermi [67] for the kinetic energy $T[\rho]$. Therein,

$$T[\rho] \approx T_s^{LDA}[\rho] = \int d^3r t_s^{hom}(\rho(r)), \tag{2.3.1}$$

is described based on a fictitious uniform electron gas with kinetic energy t^{hom}, which is a simple model of constant electron density. Additionally, it is assumed that the kinetic energy of the many-body system can be obtained by summing non-interacting one electron densities, which is also called single-particle approximation (subindex s). Furthermore, $U[\rho]$ is described by classical Coulomb interactions of the electron density. This term is also known as the Hartree energy

$$U[\rho] \approx U_H[\rho] = \frac{q^2}{2} \int d^3r \int d^3r' \frac{\rho(r)\rho(r')}{|r-r'|}. \tag{2.3.2}$$

In these approximations, the resulting total energy

$$E[\rho] \approx E^{TF}[\rho] = T_s^{LDA}[\rho] + U_H[\rho] + V[\rho] \tag{2.3.3}$$

can be calculated only in terms of the electron density without needing the wavefunction. However, molecules in the bound state are not stable and dissociate into their individual atoms having lower energy which makes it practically unusable for any chemist. This is originated from the fact that electron exchange and correlation are completely neglected in this energy functional.

2.4 Kohn-Sham Equations

To make DFT practically usable, more accurate descriptions of $T[\rho]$ and $U[\rho]$ are necessary. Kohn and Sham [68] realized that orbital-based approaches are much more accurate for describing the electronic kinetic energy. Therefore, they introduced a reference system out of non-interacting single electron functions $\Phi_i(r)$, whose density $\rho(r)$ equals exactly the density of the interacting system. $T_s[\rho]$ is expressed in terms of single-particle orbitals Φ_i(r) of a non-interacting system with density ρ as

$$T_s[\{\phi_i[\rho]\}] = \frac{\hbar}{2m} \sum_i^N \int d^3r \phi_i^*(r) \nabla^2 \phi_i(r), \tag{2.4.1}$$

where $T_s[\{\phi_i[\rho]\}]$ is now an explicit orbital functional, but implicit density functional. This means $T_s[\{\phi_i[\rho]\}]$ now depends on the full set of occupied orbitals, each which is a functional of ρ. Furthermore, $U[\rho]$ is still calculated as the hartree energy $U_H[\rho]$ and the differences of these approximations to the exact values for $T[\rho]$ and $U[\rho]$ are added as

$$E_{XC}[\rho] = (T[\rho] - T_s[\rho]) + (U[\rho] - U_H[\rho]) \tag{2.4.2}$$

to obtain a formally exact equation for the total energy

$$E[\rho] = T[\rho] + U[\rho] + V[\rho] = T_s[\phi_i[\rho]] + U_H[\rho] + E_{XC}[\rho] + V[\rho]. \tag{2.4.3}$$

The introduced term $E_{XC}[\rho]$ is called exchange-correlation functional and contains the difference $T[\rho] - T_s[\rho]$ due to electron correlation and $U[\rho] - U_H[\rho]$ due to non-classical effects of self-interaction, exchange and correlation of the electron-electron interaction. It is often decomposed into exchange (E_X, also Fermi correlation) due to the antisymmetry principle, which leads to the Pauli exclusion principle, and reduces the density around other electrons with the same spin; and the correlation due to Coulomb correlation (E_C) which acts on any two electrons. Now, most of the total energy can be computed exactly and everything which is unknown and relatively small, is contained in the exchange-correlation functional, which is also a functional of ρ as guaranteed by the Hohenberg-Kohn theorems. However, it remains unknown and has to be approximated in DFT. Some approximations are given later in Section 2.5.

The kinetic energy $T_s[\{\phi_i[\rho]\}]$ is an improved approximation for the exact $T[\rho]$, however, because it is now an orbital functional, it cannot be directly minimized with respect to the density. Instead, an indirect minimization scheme is employed

$$0 = \frac{\delta E[\rho]}{\delta\rho(r)} = \frac{\delta T_s[\rho]}{\delta\rho(r)} + \frac{\delta V[\rho]}{\delta\rho(r)} + \frac{\delta U_H[\rho]}{\delta\rho(r)} + \frac{\delta E_{XC}[\rho]}{\delta\rho(r)} \tag{2.4.4}$$

As can be seen in Eq. (2.2.5), the $\frac{\delta V[\rho]}{\delta\rho(r)}$ yields the external potential. v_H is the Hartree potential and v_{XC} is the potential of a chosen E_{XC} approximation.

$$0 = \frac{\delta E[\rho]}{\delta\rho(r)} = \frac{\delta T_s[\rho]}{\delta\rho(r)} + v(r) + v_H(r) + v_{XC}(r) \tag{2.4.5}$$

The key step is now to consider a system of non-interacting particles moving in a not yet defined potential v_s. In the absence of interactions, the minimization condition becomes

$$0 = \frac{\delta E_s[\rho]}{\delta\rho(r)} = \frac{\delta T_s[\rho]}{\delta\rho(r)} + v_s(r). \tag{2.4.6}$$

Solving this equation, the electron density $\rho_s(r)$ can be obtained. If the potential v_s is chosen to be

$$v_s(r) = v(r) + v_H(r) + v_{XC}(r) \tag{2.4.7}$$

both minimizations have the same solution, which is $\rho_s(r) = \rho(r)$. As a consequence, the density of the interacting many-body system in potential $v(r)$ described by a many-body SE can be calculated by solving the equations of non-interacting single-body system in potential $v_s(r)$. By solving the single-particle SEs of the non-interacting auxillary system in the effective potential $v_s(r)$

$$\left[-\frac{\hbar^2\nabla^2}{2m} + v_s(r)\right]\phi_i(r) = \varepsilon_i\phi_i(r) \tag{2.4.8}$$

the orbitals are obtained that reproduce the density

$$\rho(r) \equiv \rho_s(r) = \sum_i^N f_i|\phi_i(r)|^2 \tag{2.4.9}$$

of the many-body system and this allows to determine the non interacting kinetic energy $T_s[\{\phi_i[\rho]\}]$. f_i is the occupation of the ith orbital. The last three equations are known as the Kohn-Sham equations, which can be used to obtain the total energy $E[\rho]$ as well as the density $\rho[r]$ of a many-body system can be obtained by solving single-particle equations. Therefore, the effective potential v_s of the one-electron Hamiltonian has to be choosen, so that $\rho(r) = \rho_0(r)$. However, both c_H and v_{XC} depend on ρ, which in return depends on the set of orbitals $\{\phi\}$, which again depend on v_s. So, an initial guess for the density is made, e. g. out of the sum of atomic densities, and the problem is solved iteratively in a so-called self-consistent field cycle.

The ground state energy E_0 can be calculated from the converged ground state density $\rho_0(r)$ considering Eq. (2.4.3) and (2.4.7) as

$$E_0 = \sum_i^N \varepsilon_i - \frac{q^2}{2} \int d^3r \int d^3r' \frac{\rho_0(r)\rho_0(r')}{|r-r'|} - \int d^3r v_{xc}(r)\rho_0(r) + E_{XC}[\rho_0] \quad (2.4.10)$$

As can be seen, E_0 is not simply the sum of the eigenvalues ε_i of the artificial single-electron orbitals (eigenfunctions), which are only introduced to reproduce the correct density. Hence, the electron density is the only thing, which has a strict physical meaning in the Kohn-Sham equations. If the eigenvalues of the orbitals ε_i are used as an approximation for the band structure, the artificial auxillary single-body equation is applied to the many-body SE, which is formally a mean field approch with mean field v_s.

2.5 Approximations of the Exchange and Correlation Functional

Because the contribution of the exchange and correlation to the total energy is relatively small compared to the known parts $T_s[\rho]$, $U_H[\rho]$ and $V[\rho]$, simple approximation already provide useful results. There are several different approaches to approximate the exchange-correlation functional $E_{XC}[\rho]$. First, the simplest is the local density approximation (LDA),

$$E_{XC}^{LDA}[\rho] = \int d^3r e_{XC}^{hom}(\rho(r)), \quad (2.5.1)$$

which is based on the already mentioned homogenous electron gas, for which the exchange is known exactly and the correlation is parameterized regarding highly precise calculations. It has been surprisingly successful, even if the system is far away from an homogenous electron gas. This is due to the fact that LDA typically underestimates the correlation energy E_c and overestimates the exchange energy E_x leading to error cancellation to some extent.

Secondly, the class of semi-local functionals, which accounts for gradient corrections. The generalized gradient approximation, GGA, uses general functions and has the form

$$E_{XC}^{GGA}[\rho] = \int d^3r f(\rho(r), \nabla\rho(r)). \tag{2.5.2}$$

Famous examples are the PBE functional [69], especially in the physics community and the BLYP functional [70, 71] in chemistry. If this formalism is further extended by considering also the Kohn-Sham kinetic energy density

$$\tau(r) = \frac{\hbar}{2m}\sum_i |\nabla\Psi_i(r)|^2, \tag{2.5.3}$$

the functionals of type

$$E_{XC}^{meta-GGA}[\rho] = \int d^3r f(\rho(r), \nabla\rho(r), \tau(r)) \tag{2.5.4}$$

belong to the class of meta-GGA functionals. In general, the accuracy increase, but simultanously the computational effort. An even more accurate description of the $\mathrm{E_{XC}}$ can be made by using hybrid functionals, which are based on GGA functionals, but additionally include part of the exact exchange obtained by the Hartree-Fock formalism, but leads to a further significant increase of the computational cost.

2.6 Energy Decomposition based on Absolutely Localized MOs

To investigate the nature of intermolecular interactions, the energy decomposition analysis (EDA) based on absolutely localized molecular orbitals (ALMO) [72–76] can be applied. In ALMO-EDA, the total interaction energy

$$\Delta E_{tot} = \Delta E_{FRZ} + \Delta E_{POL} + \Delta E_{CT} \tag{2.6.1}$$

is decomposed into chemically meaningful components, such as the frozen interaction term $\Delta\mathrm{E}_{\mathrm{FRZ}}$, which is defined as the energy required to bring isolated molecules into the system without any relaxation of their molecular orbitals (apart from modifications associated with satisfying the Pauli exclusion principle), and the energy lowering due to orbital relaxation. The later quantity is then further decomposed into a polarization term $\Delta\mathrm{E}_{\mathrm{POL}}$ and the charge-transfer contribution $\Delta\mathrm{E}_{\mathrm{CT}}$. The polarization energy $\Delta\mathrm{E}_{\mathrm{POL}}$ is defined as the energy lowering due to the relaxation of each molecule's ALMOs in the electrostatic fields of all other molecules. The charge-transfer energy $\Delta\mathrm{E}_{\mathrm{CT}}$ is calculated as the difference in the energy of the relaxed ALMO state and the state of fully delocalized optimized orbitals. A distinctive feature of the ALMO-EDA is that the charge-transfer contribution can be separated into terms associated with forward- and back-donation for each pair of molecules, as well as a many-body higher-order (induction) contribution $\Delta\mathrm{E}_{\mathrm{HO}}$, which is very small for typical intermolecular interactions. Both, the amount of electron density transferred between a pair of molecules $\Delta\mathrm{Q}_{\mathrm{CT}}$ as well as the corresponding energy lowering $\Delta\mathrm{E}_{\mathrm{CT}}$ can be computed via

$$\Delta E_{CT} = \sum_{x,y>y} \{\Delta E_{x\to y} + \Delta E_{y\to x}\} + \Delta E_{HO} \tag{2.6.2}$$

and

$$\Delta Q_{CT} = \sum_{x,y>y} \{\Delta Q_{x\to y} + \Delta Q_{y\to x}\} + \Delta Q_{HO}. \tag{2.6.3}$$

3 Structures of Poly(heptazine imide) Salts

Experimentalists have already studied the structure of K-PHI, which was the first synthesized PHI salt, using different techniques. High-resolution transmission electron microscopy (HRTEM) and powder x-ray diffraction (PXRD) have proven its hexagonal crystalline nature and identified its lattice parameters, which were used for the model. K-PHI contains stacked heptazine units with potassium ions in different continuous channels [23], however, it is hard to experimentally determine the exact location of the ions due to disorder and stacking defects in the material. Therefore, computational calculations are a good way to further address the structure of K-PHI and the related X-PHI materials.

3.1 Computational Details

All calculations in Chapters 3, 4, 5 and 6 were performed using the here mentioned computational details. The structures of K-PHI as well as their cation exchanged analogues, X-PHI, are modeled using an idealized periodic 2D structure, which is shown on the left hand side of Fig. 3.1. The results of the carried out calculations are visualized using the VMD software [77] as on the right side of Fig 3.1. The parameters of the supercell are chosen to be a=b=12.5, c=12.8, α=β=90.0 and γ=120.0 Å according to the experimental findings.[23, 25]. The supercell contains four optimized and fixed AA-stacked PHI layers.

The energies of all structures were obtained by carrying out periodic density functional theory calculations using the hybrid Gaussian and plane wave approach (GPW), [78] as implemented in the CP2K/Quickstep code.[79] The Kohn-Sham orbitals were described by an accurate molecularly optimized double-zeta basis set with one additional set of polarization function, while the charge density was represented by plane waves with a density cutoff of 500 Ry [80]. Separable norm-conserving pseudopotentials were used to mimic the interactions between the valence electrons and the ionic cores [81, 82]. The B97-3c exchange and correlation

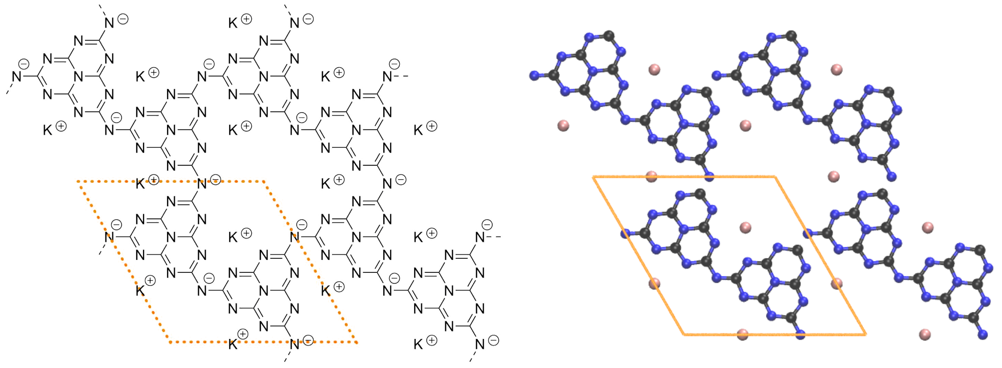

Figure 3.1: Top view of the chemical (left) idealized 2D structure of K-PHI as well as the in this work used representation (right). Atomic colors: C=black; N=blue; K=pink.

functional, which is based on Becke's power-series ansatz, plus a damped atom-pairwise dispersion correction to account for long-range van der Waals interactions was employed [83]. Optimized structures were obtained by minimizing the potential energy by performing geometry optimizations using the Broyden-Fletscher-Goldfarb-Shanno (BFGS) algorithm [84]. To assure obtaining the lowest energy structures, a variety of initial positions and orientations are chosen to cover a wide range of the configurational space for cations and adsorbates.

To investigate the helium and water adsorption inside these materials thermodynamically, the total adsorption energies

$$\Delta E_{ads}^{tot} = E[n\text{AD@X-PHI}] - E[\text{X-PHI}] - n \cdot E[\text{AD}] \tag{3.1.1}$$

and the incremental adsorption energies

$$\Delta E_{ads}^{inc} = E[n\text{AD@X-PHI}] - E[(n-1)\text{AD@X-PHI}] - E[\text{AD}] \tag{3.1.2}$$

are calculated, where E [nAD@X-PHI] is the potential energy of the optimized system when n adsorbates (AD) are adsorbed in X-PHI, whereas E[X-PHI] and E[AD] are the potential energies of isolated X–PHI and an individual AD, respectively. A negative value for the adsorption energy indicates that the adsorption is thermodynamically favorable. In the case of helium adsorption on wet K-PHI, the adsorbent K-PHI already contains adsorbed water molecules and the adsorption energies are calculated for the helium adsorbates. Furthermore, the adsorption energy per molecule

$$\Delta E_{ads}^{mol} = \Delta E_{ads}^{tot}/n \tag{3.1.3}$$

can be calculated by dividing the total adsorption energy by the total number of adsorbates n. To decompose the interaction energies of the adsorbates with the pore walls and further allocate charge transfer contributions, the ALMO-EDA is applied as described in Section 2.6. To obtain further chemical insights, net atomic charges (NAC) are estimated using the Mulliken population analysis [85] and the density derived electrostatic and chemical method (DDEC6) [86, 87], which gives chemically meaningful results. Another useful method to visualize the electron distribution inside the materials is to calculate and plot the isosurface of the electron densities ρ, as well as the electron density difference upon adsorption

$$\Delta\rho = \rho[\mathrm{AD@X-PHI}] - \rho[\mathrm{X-PHI}] - \rho[\mathrm{AD}], \tag{3.1.4}$$

where ρ[AD@X-PHI] is the total electron density of AD@X–PHI, while ρ[X-PHI] and ρ[AD] are the total electron densities of X–PHI and the individual adsorbate, i. e., helium atoms or water molecules.

3.2 Structure of K-PHI

The carried out calculations on the energetically optimized and idealized model of K-PHI suggest that the AA stacking is energetically the most favorable one. Per formally negative charged bridging nitrogen atom, one potassium is intercalated inside the PHI framework, leading to an overall neutral structure. The potassium ions are located between the PHI layers in the pores of K-PHI, where they are vertically directly stacked on top of each other. The Coulomb repulsion between the cations of different layers is hence outdone by the stabilization in the specific locations. Their position in plane is rather in the corner of the triangular-shaped pores and not in direct coordination to the bridging atoms as can be seen in Fig. 3.2. This structural charge separation inside the material can be described as frustrated Coulomb pairs as an analogue to frustrated Lewis pairs known mostly from organic chemistry[38, 39]. This structural environment may be interesting for various adsorptives, such as inert helium and more reactive water molecules, which are studied in this work.

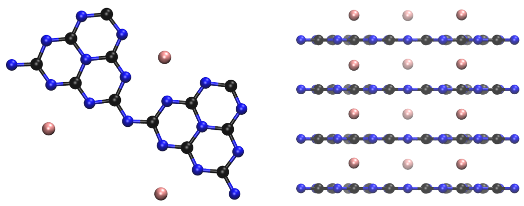

Figure 3.2: Lowest energy structure of K-PHI. Left: top view, right: side view. Atomic colors: C=black; N=blue; H=white; K=pink.

3.3 Exchange of the Cation in K-PHI

The structure of K-PHI containing intercalated potassium ions is a unique feature and may play an important role in explaining their properties. Hence, it is of huge importance to further elucidate these effects. To investigate the importance of cations, the potassiums are exchanged with other cations as well as protons and the corresponding structures are optimized in a similar fashion as done for K-PHI. It has already been shown experimentally that the cations can be exchanged relatively easily whereby the crystalline structure is basically preserved [23]. Therefore, the AA stacking is also assumed for the other cations to investigate the role of the cation in a comparable way. In this work, several alkali (Li^+, Na^+, K^+, Rb^+), alkaline earth (Ca^{2+}, Sr^{2+}, Ba^{2+}) and transition metals (Au^+, Ag^+) salts are studied as well as the proton exchanged H-PHI system. These systems are called X-PHI from now on, where X is the corresponding cation (or hydrogen). The goal is to gain a deeper understanding of the structure and their properties, i. e. the helium adsorption, examine the role of the cation choice and in the case of helium adsorption identify the best candidate.

In the lowest energy structure of H-PHI, the hydrogen atoms are covalently bonded to the bridging nitrogens, which leads to overall neutrally charged planar PHI layers. In this material, there is apparently less charge separation than present in K-PHI and it is therefore a good metal-free reference material out of almost pure carbon nitride with a similar pore size. The structures of the PHI materials containing cations of the first main group (Li^+, Na^+, K^+, Rb^+, Cs^+) are similar to each other. The lowest energy location of the cations of all the materials are in the pores between the layers as already described for K-PHI. This is due to the fact that these elements share the same charge, exhibit similar chemical behavior

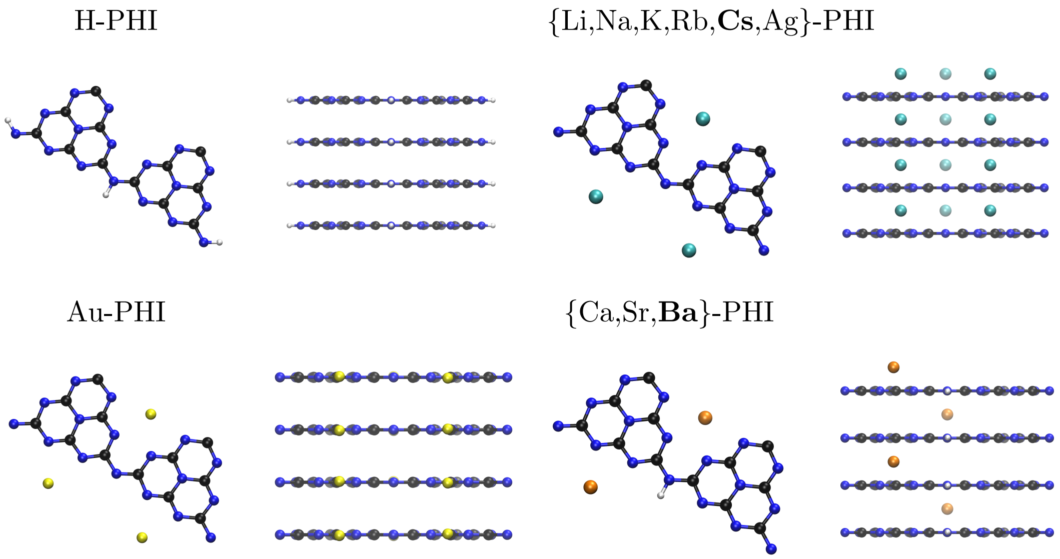

Figure 3.3: Lowest energy structures of the X-PHI materials are divided into four subgroups: covalent H-PHI, X(+1)-PHI having ions between the layers, i. e. Cs-PHI, Au-PHI with gold atoms in the same layer as PHI and Ba-PHI representing X(+2)-PHI. Left: top view, right: side view. Atomic colors: C=black; N=blue; H=white; Cs=cyan; Au=yellow; Ba=orange.

and majorly differ only by their size and reactivity. Although all cations are located between the layers, the final distance between the cation and the PHI layer increases as the cation increases. The distances between the cation and the nearest nitrogen atom vary in the range of 2.27 Å (Li-PHI) to 3.09 Å (Cs-PHI) (Table 3.1). Hence, the biggest distance, and probably the highest Coulomb frustration is expected to be in Cs-PHI containing the biggest cation of the first main group.

In the case of exchange with alkaline earth cations (Ca^{2+}, Sr^{2+}, Ba^{2+}), the total number of cations inside these frameworks is lower due to their increased charge. While there are three cations per pore per layer in the case of alkali metals, the analog for alkaline earth metals would contain on average 1.5 ions per layer. However, to maintain a more homogenous distribution of positive charge through the pores, only one cation per layer per pore is introduced. Therefore, one extra covalent hydrogen atom per layer is added to keep the charge of the structure neutral. They are covalently bonded to one of three bridging nitrogen atoms of the PHI layers as they are present in H-PHI. All studied cations from the second main group of the periodic table have a similar location between the layers in the pores. They are alternatively occupying adsorption sites still in the edges of the pores trying to maximize the occupied space inside these pores. Because of their higher charges, their surrounding electrostatic field is stronger, leading to higher repulsive forces between the cations. The distances of the alkaline earth metals to the PHI layers in the range from 2.57 Å (Ca-PHI) to 2.91 Å (Ba-PHI) follow the same trend as the first main group (3.1) and hence Ba-PHI exhibits the highest separation.

The investigated PHI systems containing transition metals in oxidation state +1 are similar to the alkali metals, which carry the same formal charge. Silver is similarly located in the pores between the layers. With a distance of 2.50 Å, the location of the ions is between the ones found for Li^+ and Na^+. In contrast to all other investigated systems, gold cations are found to be energetically rather located inside the same layer as the PHI than between them. All investigated systems are shown in Fig. 3.3 as four subgroups: H-PHI with covalent hydrogen atoms, X(+1)-PHI and X(+2)-PHI having cations between the layers, as well as Au(+1)-PHI, where the gold ions are in the same layer as the PHI planes. The structures inside a subgroup only differ by their exact horizontal position, because bigger cations are slightly shifted towards the middle of the pore increasing their distance d to the PHI layers.

Noteworthy, in these calculations only the lowest energy state of the materials is considered. The possibility of cation exchange in these materials [23] suggests that the cations are able to move throughout the pore channels.

Table 3.1: Vertical lowest energy position of the cations in X-PHI (Pos. X), average DDEC6 charges q_i, distance d between X and nearest nitrogen of PHI, as well as the product $\mu = q_x \cdot d_{XN}$.

X-PHI	**Pos. X**	q_X [e]	q_C [e]	q_N [e]	d_{XN} [Å]	μ [eÅ]
H-PHI	cov.	0.34	0.53	-0.43	1.00	0.34
Li-PHI	between	0.87	0.55	-0.54	2.27	1.97
Na-PHI	between	0.88	0.56	-0.55	2.79	2.46
K-PHI	between	0.82	0.55	-0.54	2.84	2.34
Rb-PHI	between	0.80	0.56	-0.53	2.99	2.39
Cs-PHI	between	0.77	0.56	-0.53	3.09	2.37
Ca-PHI	between	1.42	0.53	-0.48	2.57	3.64
Sr-PHI	between	1.46	0.53	-0.48	2.73	3.99
Ba-PHI	between	1.44	0.53	-0.48	2.91	4.19
Ag-PHI	between	0.55	0.53	-0.47	2.50	1.37
Au-PHI	in-plane	0.30	0.52	-0.42	2.55	0.78

3.4 Net Atomic Charges and Electron Density

The charge distributions inside the X-PHI materials are assumed to be an important factor in explaining their properties. Therefore, net atomic charges are estimated using the density derived electrostatic method (DDEC6). The average charges for each atomic kind are given in Table 3.1. First of all, these calculations reflect the expected behavior that the cations are positively charged in the range of 0.30 to 1.46. The fact that the partial charge of the cations is lower than the formal oxidation state means that the cation-framework interaction is not solely Coulomb type as it is typical for any chemical system. However, in most cases, the interaction is dominated by Coulomb interactions. Since the total system is neutral, the PHI layers carry the exact amount of negative charges, which are rather located at the more electronegative nitrogen atoms ($q_N \approx -0.5$) than at the on average partial positive carbon atoms ($q_C \approx +0.5$). There are one-third more nitrogen than carbon atoms inside these materials, reflecting the overall negative charge in the PHI layers. Furthermore, the product of the charge of the cation times the nearest distance of it to the PHI layers is calculated to obtain a dipole-like quantity μ in order to have a very simple way to quantify the charge separation in these materials. In H-PHI, only a relatively low charge separation is present due to the absence of cations and only covalently bonded hydrogen atoms (q_H=0.34 e, d_{HN}=1.0 Å, μ=0.34 eÅ). The alkali cations carry positive net atomic charges in the PHI systems between 0.77 (Cs^+) and 0.88 (Na^+). The distance between the cation and the PHI layers naturally depends on the size of the cations and thereby Cs^+ has the highest distance. While the calculated charges and distances for the cations Na^+, K^+, Rb^+ and Cs^+ are close to each other, leading to similar μ (2.34-2.46 eÅ), Lithium is found to be closer to the PHI layers and hence has the smallest μ=1.97 eÅ. The obtained net atomic charges of the alkaline earth metals are logically higher from 1.42 (Ca^{2+}) to 1.46 (Sr^{2+}). Again, the size of the cation is determining, leading to Ba-PHI having the highest Coulomb frustration (μ=4.19 eÅ). The transition metals carry the least positive charged metals inside the materials. Silver has a partial charge of 0.55 while gold has the lowest charge of all (0.30), which is even below the partial charge of the hydrogen atoms in H-PHI. This underlines the typical behavior of gold, which exhibits a significant covalent bonding character assigned to relativistic effects on 5d and 6s orbitals [88]. This also explains the different positions in the PHI plane compared to other cations.

4 Helium adsorption in X-PHI

After determining the optimized structures of the X-PHI materials and analyzing their net charges, helium adsorption inside their pores is addressed in this chapter. Helium is known to be the most inert element of all in the periodical table and hardly undergoes interactions of any kind. Therefore, it is interesting to investigate the interactions of helium inside the highly polarizing environment of these materials and to study the role of cation choice.

4.1 Structure and Energy of Helium Adsorption

A single helium atom is placed inside the nanopores of the X-PHI materials, whose structures were determined in the previous chapter, and the lowest energy adsorption state as well as the corresponding adsorption energy are calculated. Interestingly, helium adsorption is thermodynamically favorable in all studied systems. Even in the metal-free H-PHI system, helium can be adsorbed, releasing an adsorption energy of -2.4 kJ/mol. This is the lowest adsorption energy of all studied systems, however, the fact that helium adsorption is energetically favorable in H-PHI, shows the high adsorption potential of metal-free porous carbon nitrides. The adsorption energy is significantly enhanced in the cation containing X-PHI systems and is in the range of -3.1 kJ/mol to -5.5 kJ/mol. This underlines the importance of charged surroundings for a unique adsorption environment and a thermodynamically increased interaction of helium inside these nanopores. Overall, the highest adsorption energy of -5.5 kJ/mol occurs in the Cs-PHI system, which exhibits a high Coulomb frustration due to the size of the cation. In general, the adsorption energy for alkali metal cation containing PHIs is higher than for the PHIs with alkaline earth metal cations. This might be counter-intuitive due to the fact that alkaline earth metals carry an even higher charge, however, this also lowers the total number of cations in the pores. Additionally, while there are three cations present per pore per layer in the case of +1-charged cations, they are replaced by one +2-charged cation plus one hydrogen atom in the carried out simulations, which leads to a lower total charge per volume. Within both main groups, the trend can be observed, that bigger cations (higher period) lead to higher adsorption energies. They exhibit a higher spatial charge separation and thus, Ba-PHI entails the highest heat of adsorption (-3.4 kJ/mol) for helium in the studied PHI systems containing second main group ions. In PHI containing transition metals, helium adsorption is also energetically favorable, but silver (-3.1 kJ/mol) and gold (-3.6 kJ/mol) do not lead to a energetical increase of the helium interaction inside the PHI materials.

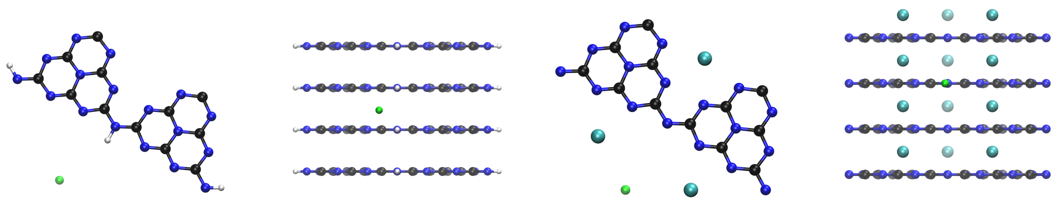

He in H-PHI

He in Cs-PHI

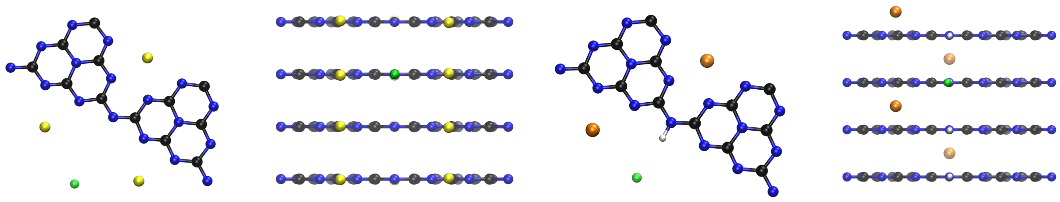

He in Au-PHI

He in Ba-PHI

Figure 4.1: Structures of the lowest energy adsorption state of helium in H-PHI, Cs-PHI, Au-PHI and Ba-PHI. Atomic colors: C=black; N=blue; He=green; H=white; Cs=cyan; Au=yellow; Ba=orange

The lowest energy adsorption sites for the adsorbed helium atoms are in all structures inside the existing pores of the materials. The horizontal position is always near the middle of the pore and hence in the presence of +1 cations in-between the three cations, which are oriented in a triangular shape as determined by the pore geometry. Interestingly, the He atoms can occupy sites, either in the same plane as the PHI layers or between them with only minor changes in the corresponding energy. Hence, at finite temperatures, the helium atoms are expected to diffuse through the pore channels of the materials. Whether the lowest energy adsorption site of the helium atom is in the same layer as the PHI plane or in-between is dependent on the system. The vertical positions of He in all studied systems are given in Table 4.1. Exemplary, the lowest energy structures upon single helium adsorption are shown in Fig. 4.1 for H-PHI, Cs-PHI, Au-PHI, Ba-PHI.

Table 4.1: Vertical lowest energy position of a single helium atom adsorbed in X-PHI (Pos. He), the corresponding adsorption energy E_{ads} as well as the DDEC6 charge of helium q_{He} in the adsorbed state.

X-PHI	**Pos. He**	$\mathbf{E}_{ads}$ [kJ/mol]	$\mathbf{q}_{He}$ [e]
H-PHI	between	-2.40	0.010
Li-PHI	between	-3.79	0.009
Na-PHI	between	-3.59	0.002
K-PHI	in-plane	-4.30	0.006
Rb-PHI	between	-4.82	0.007
Cs-PHI	in-plane	-5.45	0.012
Ca-PHI	between	-2.96	0.006
Sr-PHI	in-plane	-3.10	0.006
Ba-PHI	in-plane	-3.39	0.008
Ag-PHI	in-plane	-3.10	0.006
Au-PHI	in-plane	-3.55	0.002

4.2 Net Atomic Charges and Electron Density

The DDEC6 analysis is also applied to the optimized structures after helium adsorption to determine the charges of the helium atoms in the adsorbed state q_{He} (Table 4.1). Excitingly, the net atomic charges are slightly positive up to 0.012 e (Cs-PHI), which demonstrates that a charge of around 1% of an electron is transferred from the otherwise inert helium to the electron-poor PHI materials. This means that part of the interaction with helium originates from partial charge transfer. The charges of other atoms in the X-PHI systems practically do not change, since the small counter charges of the helium atoms are distributed through the system. Assuming that charge transfer effects due to the charge separation inside these structures are essential for the adsorption environment of helium, this offers an explanation for why the adsorption energies are higher in the systems containing big frustrated cations. Helium carries the highest charge in Cs-PHI, which is the system with also the highest adsorption energy. However, in the calculated charges, there is no evidence for an overall correlation between the exact partial charge of the adsorbed helium and the corresponding heat of adsorption. The role of the charge transfer and its contributions are later studied in more detail using the energy decomposition analysis based on absolutely localized molecular orbitals (ALMO-EDA). For better visualization, the electron density as well as the electron density differences upon helium adsorption are calculated and shown in terms of 3D isosurfaces in Fig. 4.2 for Cs-PHI, which is the thermodynamically best adsorption material. The electron density distribution of pristine Cs-PHI visualizes the results of the DDEC6 analysis and pictures the high electron probabilities (red) at the more electronegative nitrogen atoms of the negative PHI layers. In the case of helium adsorption at Cs-PHI, the isosurfaces of the electron density difference are plotted showing regions of accumulation (green) and depletion (red) of electrons in the presence of adsorbed helium. The helium is located in the middle of the pore where there is a red dot indicating a decreased density as compared to an isolated gas phase helium atom at the same position. Although there are only small amounts of charges involved in the adsorption process, it can be seen that the positive charge of the helium results from interaction with the Cs cations, whose electron distribution is influenced due to charge transfer of the adsorbed helium.

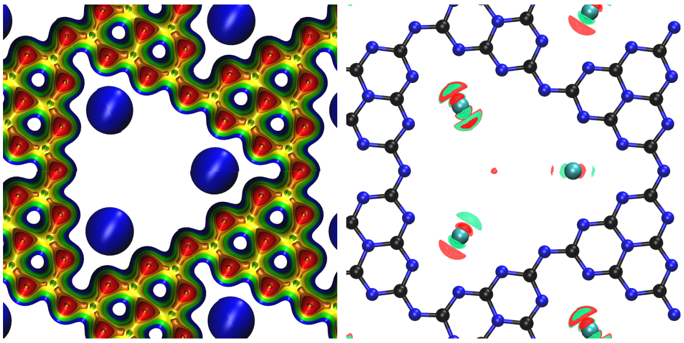

Figure 4.2: Electron density isosurfaces of Cs-PHI (left, isovalues = 0.05/0.1/0.2/0.3/0.4 from blue to red) and the electron density differences upon helium adsorption in Cs-PHI (isovalues = ± 0.001 red(+)/green). Atomic colors: C=black; N=blue; Cs=cyan; He=green.

The adsorption of only a single helium atom is studied in the X-PHI materials. However, it has to be noted that adsorption of multiple helium atoms is not only able to influence the vertical lowest energy position, but also the overall adsorption energy due to competition and limited space and adsorption sites inside the pores.

4.3 Energy Decomposition Analysis

The origin of the adsorption energies of helium in the X-PHI materials is further studied by applying the ALMO-EDA. It allows to decompose the interaction between the helium atoms and the adsorbent into a frozen energy term E_{FRZ}, a polarization term E_{POL} and charge transfer contributions. The amount of charge transfer and the corresponding stabilization energy can be assigned to individual charge donor and acceptor pairs. The summed energy of the ALMO-EDA is the interaction energy of helium and the X-PHI material. It does not exactly equal the adsorption energy discussed before due to possible displacement i. e. of the cations during helium adsorption, which is not included in the ALMO-EDA calculations. However, in this case, this geometric distortion term only has a small contribution and can be neglected (<0.5 kJ/mol). The analysis results for the helium interaction with all studied X-PHI systems are shown in Table 4.2. The energy percentages to the total interaction energy are given in parentheses after each energy. The results are also plotted as a stacked bar chart in Fig. 4.3.

Table 4.2: Results of the decomposition of the interaction energy of adsorbed helium inside the pores of the X-PHI materials to a frozen energy term E_{FRZ}, a polarization term E_{POL} and the charge transfer contributions from PHI to He $E_{PHI \rightarrow He}$ and from He to the corresponding cations $E_{He \rightarrow X}$ as well as their respective transferred charges $q_{PHI \rightarrow He}$ and $q_{He \rightarrow X}$. The percentages (%) of the energies to the total interaction are given in parentheses.

X-PHI	**ΔE_{FRZ}** [kJ/mol]	**ΔE_{POL}** [kJ/mol]	**$\Delta E_{PHI \rightarrow He}$** [kJ/mol]	**$q_{PHI \rightarrow He}$** [me]	**$\Delta E_{He \rightarrow X}$** [kJ/mol]	**$q_{He \rightarrow X}$** [me]
H-PHI	-2.06 (74)	-0.03 (1)	-0.12 (4)	0.03	-0.58 (21)	0.31
Li-PHI	-1.95 (48)	-0.28 (7)	-0.39 (10)	0.09	-1.42 (35)	0.87
Na-PHI	-2.22 (65)	-0.16 (1)	-0.25 (7)	0.06	-0.80 (23)	0.49
K-PHI	-3.22 (76)	-0.05 (1)	-0.13 (3)	0.04	-0.82 (19)	0.51
Rb-PHI	-4.03 (77)	-0.05 (1)	-0.32 (6)	0.09	-0.83 (16)	0.51
Cs-PHI	-4.76 (81)	-0.06 (1)	-0.27 (5)	0.07	-0.79 (13)	0.48
Ca-PHI	-2.24 (72)	-0.06 (2)	-0.15 (5)	0.05	-0.67 (22)	0.38
Sr-PHI	-2.34 (71)	-0.07 (2)	-0.10 (3)	0.03	-0.77 (24)	0.46
Ba-PHI	-2.47 (68)	-0.10 (3)	-0.13 (3)	0.04	-0.94 (26)	0.57
Ag-PHI	-2.36 (70)	-0.04 (1)	-0.15 (4)	0.04	-0.82 (24)	0.54
Au-PHI	-2.81 (74)	-0.06 (2)	-0.08 (2)	0.02	-0.82 (22)	0.53

For all investigated systems, the ALMO-EDA shows that $\Delta E_{FRZ} > \Delta E_{CT} > \Delta E_{POL}$. Hence, the frozen term is the dominating energy contribution to the interaction between helium and all studied adsorbing materials. The frozen term

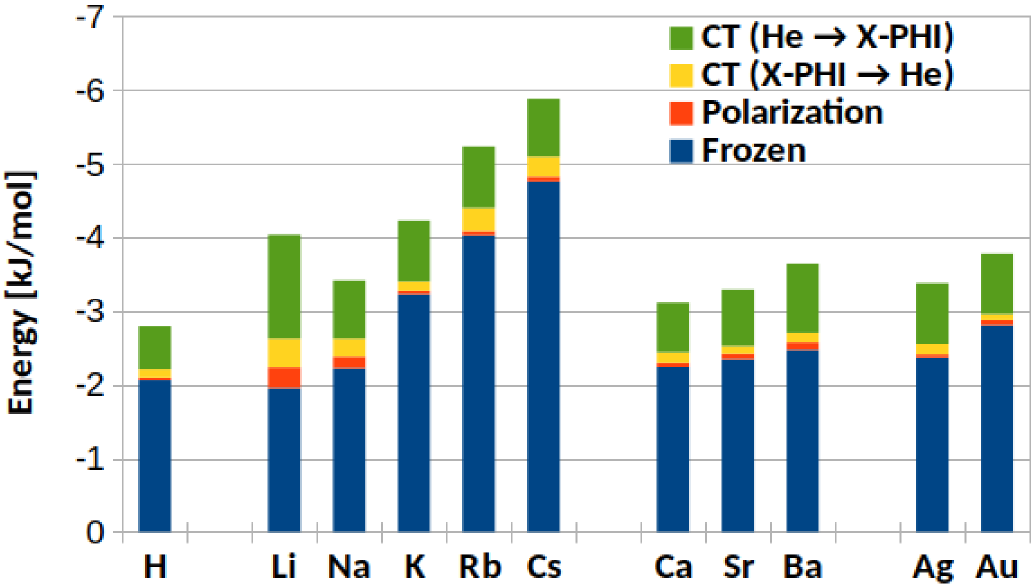

Figure 4.3: Schematic representation of the results of the energy decomposition analysis of helium adsorption in X-PHI shown in Table 4.2

physically mainly represents pure electrostatic interactions, which indicates the importance of present cations and charge separation inside these materials. The highest percentage of the frozen energy term (81%, -4.8 kJ/mol) to the total energy, is found in Cs-PHI, which also has the highest adsorption energy. Notably, the interactions inside materials with lower charge separation and lower adsorption energies, like the covalent H-PHI system and the comparable Au-PHI, are also dominated by Coulomb interactions (both 74%).

Additionally, the calculations suggest that the second-highest term, the charge transfer, also substantially contributes to the total interaction energy in all systems. To investigate the interaction between helium and X-PHI due to charge transfer, the transfer contribution from the X-PHI framework to the He atoms is studied and vice versa. The charge transfer interaction of helium in the metal containing systems can be assigned to two contributions: a charge transfer $q_{\mathrm{PHI}\rightarrow\mathrm{He}}$ from the negative PHI layers to He and from He to the corresponding cation X $q_{\mathrm{He}\rightarrow\mathrm{X}}$. There is practically no back donation from X to He or from He to PHI, respectively ($q_{\mathrm{He}\rightarrow\mathrm{PHI}} \approx q_{\mathrm{X}\rightarrow\mathrm{He}} \approx 0$). In H-PHI, there is no metal ion and hence the neutral PHI layers can also accept a significant charge from the helium (0.31 me, -0.58 kJ/mol). The calculations reflect that the helium atoms are better electron donors than acceptors ($q_{\mathrm{He}\rightarrow\mathrm{X}} > q_{\mathrm{PHI}\rightarrow\mathrm{He}}$), which was already indicated by the calculated positive net atomic charges on the helium atoms after adsorption. Hence, helium has a slightly basic character and interacts more with the acidic sites, i. e., the cations in these materials via charge transfer. In the best He adsorber Cs-PHI, the amount of charge transferred $q_{\mathrm{He}\rightarrow\mathrm{X}}$ from the helium to the Cs cation is 0.48 me resulting in stabilization energy $\Delta E_{\mathrm{He}\rightarrow\mathrm{X}}$ of -0.8 kJ/mol. However, the values of transferred charge (0.38-0.57 me) as well as the energies (-0.7 to -0.9 kJ/mol) are rather similar in all investigated systems. This also applies to the comparison of alkali with alkaline earth metals, even though the cations carry a different charge. Exceptions from these ranges are the covalent H-PHI due to the absence of cations and Li-PHI, which exhibits the significantly highest CT to the cation (0.87 me, -1.4 kJ/mol). The other charge transfer from the PHI layers to the adsorbed helium $q_{\mathrm{He}\rightarrow\ \mathrm{X}}$ is the smaller contribution in all systems (<0.1 me, <0.4 kJ/mol). The lowest values are found in H-PHI and Au-PHI, which is because they carry the lowest negative charges on the PHI layers compared to the other systems.

On top of the Coulomb and charge transfer interactions, polarization effects, i. e. the formation of dipoles, quadrupoles, etc., also contribute to the total interaction energy as can be seen in the energies E_{POL}, however, only to a small extent ($\leq 7\%$). The least polarization energies are found in the covalent H-PHI (-0.03 kJ/mol) and the comparable Au-PHI (-0.04 kJ/mol), which is a consequence of the low charge separation inside these materials. In the other X-PHI materials, the polarization energy is higher, which indicates that the presence of cations in an anionic organic framework is essential and that their electric fields are able to induce a dipole moment in the otherwise non-polarizable He atom. However, the absolute energies are relatively low (-0.05 kJ/mol to -0.28 kJ/mol). In Cs-PHI, the polarization energy is -0.06 kJ/mol and contributes only 1% to the total interaction energy. The highest polarization interaction is found in Li-PHI (-0.28 kJ/mol, 7%). Hence, Li-PHI can also be regarded as a special case. It significantly differs from the other systems and has the lowest E_{FRZ}, but the highest E_{POL} and E_{CT}, possibly because of its high electronegativity and tendency to form bonds with higher covalent character compared to the other studied alkali and alkaline earth metals.

5 Water Adsorption in K-PHI

In this chapter, a single water adsorption in the nanopores of K-PHI is investigated in terms of structure, thermodynamics and interactions. After that, the properties of multiple water molecules inside K-PHI are discussed.

5.1 Structure and Energy of Single Water Adsorption

According to the carried out calculations, water adsorption is energetically favorable in K-PHI. The adsorption of a single water molecule entails adsorption energy of ΔE_{ads} = -94.5 kJ/mol. This adsorption energy of water in K-PHI is surprisingly high and more than twice as much as the heat of vaporization of water (ΔH_{vap}=40.7 kJ/mol [89]). This means that the interactions of water with the pore walls of K-PHI are twice as strong as the water-water interactions in bulk. Due to the high bond strength, it is not a typical physisorption. Instead it appears that water becomes an integral part of the material's structure after adsorption. The lowest energy adsorption site of the first adsorbed water molecule is located in the pores between the PHI layers as can be seen in Fig. 5.1a. In that case, water is located between the positive potassium cations and forms hydrogen bonds with nitrogens of both surrounding negative PHI layers. The oxygen of the water is forming coordinate bonds to the potassium centers while at the same time, the lone pairs of the surface nitrogens act as basic sites for the hydrogen atoms of water. This highly polarized adsorption environment of the water molecule explains the high calculated adsorption energy. The distances between the hydrogen atoms of the water and the involved nitrogen atoms are 2.20 and 2.07 Å, respectively.

5.2 Net Atomic Charges and Electron Densities

To investigate the electronic environment of the adsorbed water, net atomic charges were calculated using the Mulliken population analysis and the density derived

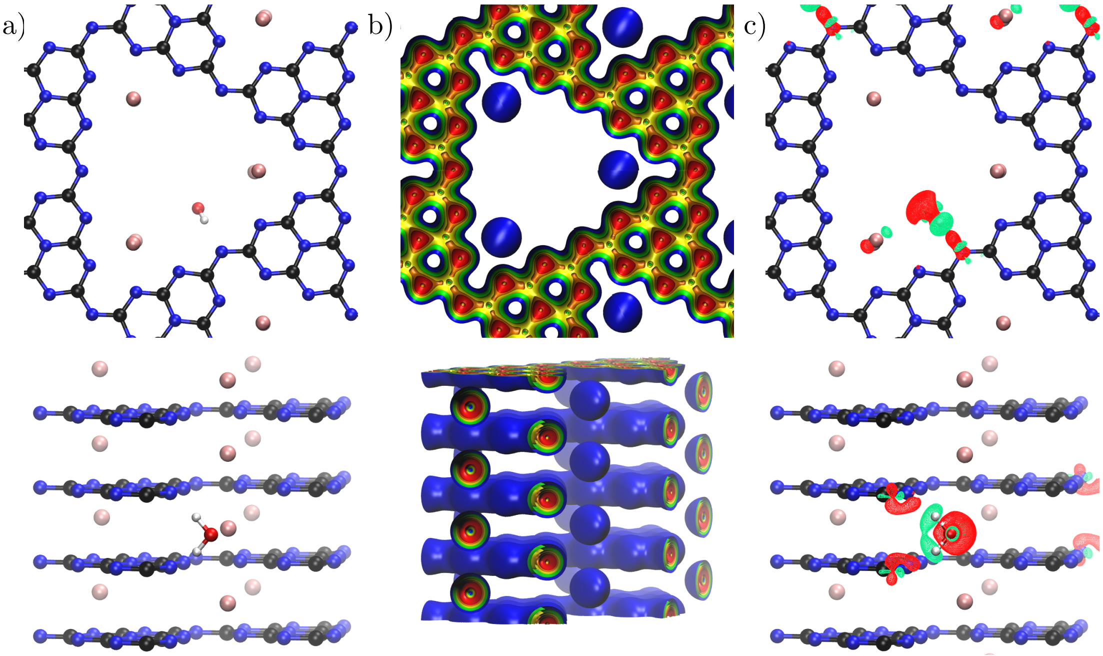

Figure 5.1: Adsorption state of a single water molecule in K-PHI (a), electron density isosurfaces of K-PHI (b, isovalues = 0.05/0.1/0.2/0.3/0.4 from blue to red) and the electron density differences upon water adsorption in K-PHI (c, isovalues = ± 0.002 red(+)/green). Top: top view, bottom: side view. Atomic colors: C=black; N=blue; K=pink; O=red; H=white.

Table 5.1: Averaged net charges calculated by Mulliken as well as DDEC6 method of a single water molecule adsorbed in K-PHI.

	Mulliken	**DDEC6**
K	0.61	0.83
C	0.10	0.55
N	-0.17	-0.54
O	-0.34	-0.84
H	0.13	0.36
PHI	-1.81	-2.45
H_2O	-0.07	-0.12

electrostatical and chemical method DDEC6. The averaged values for each atomic type as well as the summed values for H_2O and the PHI layers per unit cell are shown in Table 5.1. The analysis confirms the positive charges of the potassium ions (Mulliken 0.61; DDEC6 0.83), which are interacting with the partially negative oxygen atoms (-0.34; -0.84) of the adsorbed water molecules. The negative charge of the PHI system (-1.81; -2.45; formally -3) is distributed throughout the layers but mostly located at the more electronegative nitrogen atoms (-0.17; -0.54), whereas the carbon atoms on average carry a positive charge (0.10; 0.55). This behavior is visualized in the top view of the electron density distribution of pristine K-PHI in Fig. 5.1b, where the highest electron densities (red) are located around all the nitrogen atoms. This bond polarization inside the CN framework further active the surface nitrogens as basic sites, which are important for the water adsorption. With these partially negatively charged nitrogen atoms, the water molecules – more precisely, the hydrogen atoms of the water (0.13; 0.36) – form the hydrogen bonds that stabilize the water adsorption. Water carries a slight negative charge in the adsorbed state due to charge transfer from the PHI system to the water. This is also illustrated in the electron density difference representations in Fig. 5.1c, where the charge is increased around the surface nitrogen atoms. A more precise description of the interaction of water inside K-PHI is discussed in the following energy decomposition analysis.

5.3 Energy Decomposition Analysis

To study the origin of the high adsorption energy, the ALMO-EDA is applied to single water adsorption in K-PHI. It allows to decompose the interaction of water with its surroundings into physically meaningful components, i. e. the frozen energy ΔE_{FRZ}, the polarization energy ΔE_{POL} and charge transfer contributions ΔE_{CT}. The results of the ALMO-EDA are given in Table 5.2.

Table 5.2: ALMO-based energy decomposition of the interaction between water and K-PHI.

	$\Delta \mathbf{E}_{FRZ}$	$\Delta \mathbf{E}_{POL}$	$\Delta \mathbf{E}_{CT}$
H_2O @ K-PHI	-57.4 kJ/mol	-18.8 kJ/mol	-42.8 kJ/mol

The main part of the interaction is due to Coulomb interactions of the water molecule and K-PHI, which is represented by the frozen energy term (-57.4 kJ/-mol). This high electrostatic interaction is due to the capability of water to interact with both the positively charged potassium as well as with the anionic PHI framework. This charge separation inside the material also leads to a high polarization energy of -18.8 kJ/mol. Excitingly, a remarkable part (-42.8 kJ/mol) of the interaction between the water molecule and the adsorbent is due to charge transfer contributions. The difference between the adsorption energy (-94.5 kJ/mol) and

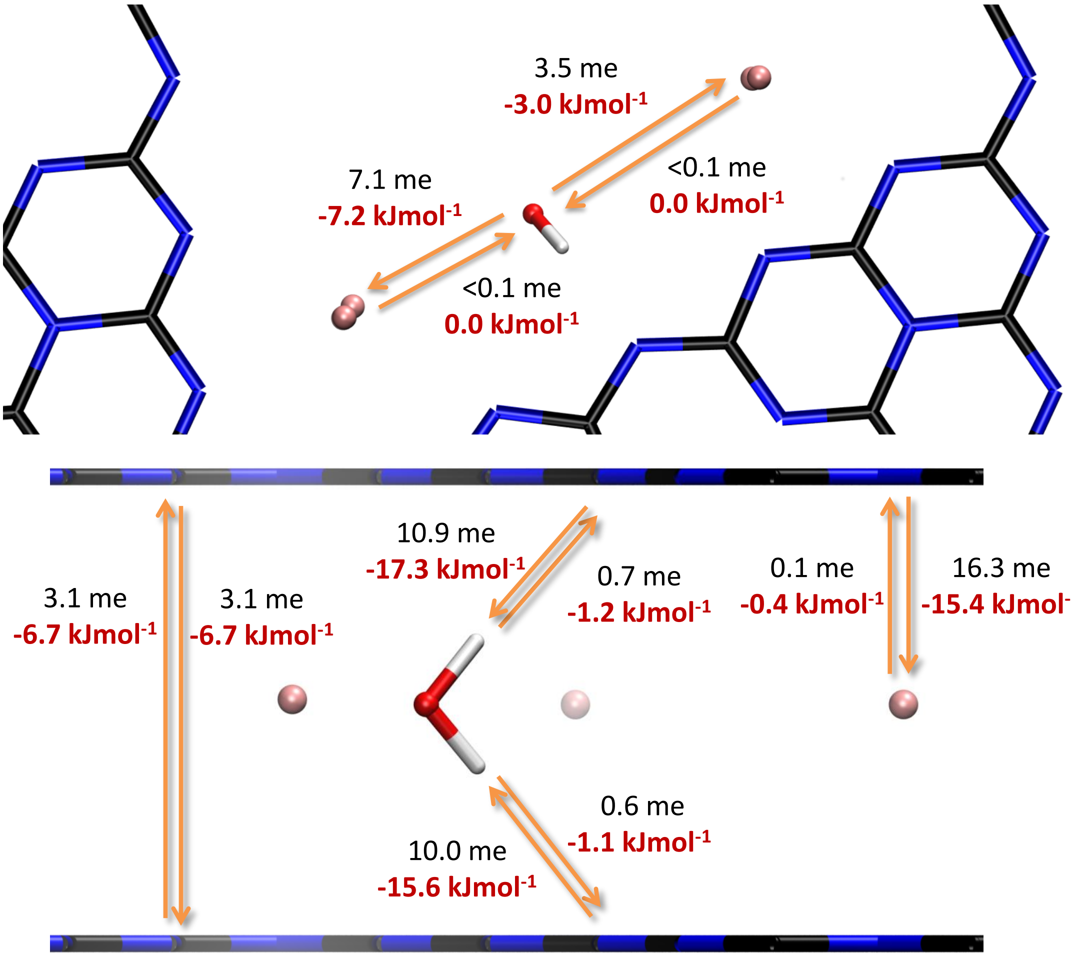

Figure 5.2: Horizontal (top) and vertical (middle) charge transfers (black) occurring between water, the positive K^+ and the negative PHI layers as well as the resulting stabilization energy (red) upon single water adsorption in K-PHI as computed by the ALMO-EDA. Atomic colors: C=black; N=blue; K=pink; O=red; H=white.

the sum of the ALMO interactions (-119.0 kJ/mol) is due to slight distortion of the structure and repositioning of the potassium cations upon water adsorption which is not included in the single point ALMO calculation. This energy difference is sometimes referred to as geometric distortion ΔE_{GD} [90]. The amount of charge transfer and the corresponding stabilization energy can be further assigned to individual charge donor and acceptor pairs. All charge transfers (black) and resulting stabilization energies (red) are shown in Fig. 5.2. The most significant contributions of the charge transfer is the charge transfer from the two neighboring negative PHI layers to H_2O (in total: 20.9 me, -32.9 kJ/mol), which occurs in the context of the hydrogen bonds of water the PHI layers. And secondly, a substantial charge transfer is also occurring from H_2O to the nearest K^+ ions (10.6 me, -10.2 kJ/mol). Both interactions contribute to the high amount of charge transfer stabilization energy of water inside this highly polarizing adsorption environment of K-PHI. An additional back donation from the PHI layers to the water also takes place (1.3 me, -2.3 kJ/mol) Beside the water interactions, the ALMO–EDA calculations reveils a significant charge transfer between the PHI layers of 3.1 me (-6.7 kJ/mol). The PHI layers further transfer a substantial amount of 16.3 me to the potassium ions resulting in a high stabilization of -15.4 kJ/mol per cation per layer plus a small back donation (0.1 me; -0.4 kJ/mol).

5.4 Structures and Energies of Multiple Water Adsorption

As K-PHI reveals a high availability of adsorption sites on the pore walls, this section deals with the adsorption of multiple water molecules in the pores to see how they influence each other as well as to determine the maximum water uptake inside the material. K-PHI can uptake multiple water molecules being thermodynamically favorable. The total adsorption energy $\Delta E_{\mathrm{ads}}^{\mathrm{tot}}$ increases rather linearly as can be seen in Fig. 5.3. Hence, the incremental adsorption energy is relatively constant, which means that the additional water molecules undergo a very similar strong interaction with K-PHI as the first one. The corresponding energy values are also given in Table 5.3. It suggests that the adsorption of multiple water molecules neither enhances (e. g., by hydrogen bonds with each other) nor diminishes (e. g., repulsion due to limited space) the water adsorption thermodynamics significantly. It is also possible that these effects compensate each other to some extent. The incremental adsorption analysis reveals that K-PHI can adsorb water until a final uptake of 14.0 wt% (corresponding to N=18 H_2O molecules in the simulation) and a maximum $\Delta E_{\mathrm{ads}}^{\mathrm{tot}}$ = -1501 kJ/mol is reached. After that, the adsorption finally is thermodynamically unfavorable because the space and especially the adsorption sites in the pores are exploited. The final adsorption energy per molecule upon complete filling is $\Delta E_{\mathrm{ads}}^{\mathrm{mol}}$ = -83.4 kJ/mol per H_2O.

The lowest energy structure of the adsorption state of the water molecules is dependent on the amount of water inside the material. The water molecules are preferentially placed in the pores and like to interact with the pore walls. However, only at low water uptake, the structure is very well organized at specific adsorption

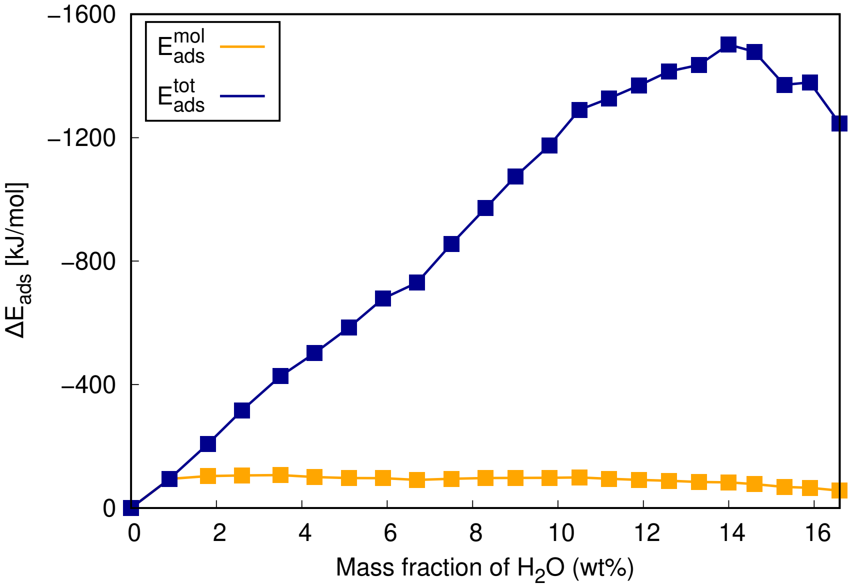

Figure 5.3: Total adsorption energy ΔE^{tot}_{ads} as well as the adsorption energy per molecule ΔE^{mol}_{ads} of water in K-PHI as a function of water loading (in wt%)

Table 5.3: Underlying data for Fig. 5.3.

N	ΔE^{tot}_{ads}	ΔE^{inc}_{ads}	ΔE^{mol}_{ads}	wt_{H_2O}	**N**	ΔE^{tot}_{ads}	ΔE^{inc}_{ads}	ΔE^{mol}_{ads}	wt_{H_2O}
	[kJ/mol]	[kJ/mol]	[kJ/mol]	[%]		[kJ/mol]	[kJ/mol]	[kJ/mol]	[%]
1	-94.5	-94.5	-94.5	0.9	11	-1073.8	-102.5	-97.6	9.0
2	-207.7	-113.2	-103.8	1.8	12	-1174.6	-100.8	-97.9	9.8
3	-316.7	-109.0	-105.6	2.6	13	-1290.1	-115.5	-99.2	10.5
4	-427.3	-110.6	-106.8	3.5	14	-1327.4	-37.3	-94.8	11.2
5	-502.1	-74.8	-100.4	4.3	15	-1369.2	-41.8	-91.3	11.9
6	-584.4	-82.3	-97.4	5.1	16	-1414.7	-45.5	-88.4	12.6
7	-678.7	-94.3	-97.0	5.9	17	-1435.5	-20.8	-84.4	13.3
8	-730.0	-51.3	-91.2	6.7	18	-1501.4	-65.9	-83.4	14.0
9	-855.2	-125.2	-95.0	7.5	19	-1478.5	23.0	-77.8	14.6
10	-971.3	-116.1	-97.1	8.3	20	-1371.0	107.5	-68.5	15.3

sites in a similar fashion as the individual adsorbed water molecule. This is possible until one water molecule per pore and per layer is adsorbed (Fig. 4; 3.5 wt%; N=4). On additional adsorption, the water molecules are still adsorbing at similar adsorption sites with high hydrogen bond affinity towards the PHI layers as can be seen in the adsorption state at 6.7 wt% (N=8). However, the adsorption state of the water molecules tends to be more disordered. On one hand, they are forming attractive hydrogen bonds with each other. On the other hand, repulsive Coulomb forces also play a role upon further water filling because of the limited space in the nanopores of K-PHI. In the case of complete filling (14 wt%; N=18), these effects increase. Hence, some water molecules are located also more in the middle of the pore, which do not interact with the PHI layers directly anymore. However, they are still interacting with the potassium cations and other water molecules. These effects explain very well why the average energy released upon adsorption ($\Delta \mathrm{E}_{\mathrm{ads}}^{\mathrm{mol}}$ = -83.4 kJ/mol) is slightly decreased compared to the single adsorbed water molecule ($\Delta \mathrm{E}_{\mathrm{ads}}$ = -94.5 kJ/mol). However, this is still a remarkable interaction of water with K-PHI at high water uptake.

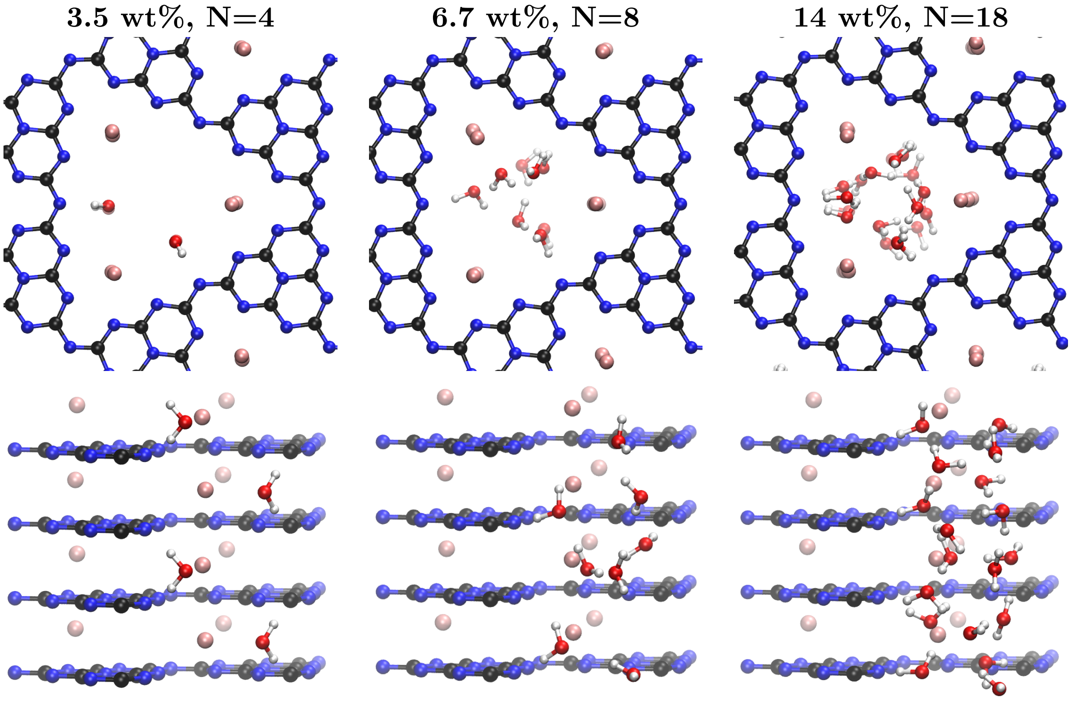

Figure 5.4: Adsorption states of water in K-PHI at different H_2O loadings. N corresponds to the number of water molecules inside the supercell. Top: top view, bottom: side view. Atomic colors: C=black; N=blue; K=pink; O=red; H=white.

6 Impact of Water on the Helium Adsorption in K-PHI

As described in the previous chapters, K-PHI reveals great affinities for the inert helium (-4.3 kJ/mol, Chapter 4) as well as for water (-94.5 kJ/mol, Chapter 5). Due to its high adsorption energy, K-PHI probably tightly binds water even at low partial pressures. The water is expected to be hardly removable and hence can be described as part of the material after adsorption. Therefore, the question remains whether helium can still adsorb in the presence of water, e. g. due to exposure of the material to humidity. For this purpose, the adsorption energy of n helium atoms on wet K-PHI filled with N water molecules is investigated and compared with the corresponding adsorption energy of helium in dry K-PHI (N=0).

6.1 Structure and Energies of Helium Adsorption

The lowest energy adsorption sites of one adsorbed helium atom and a single present water molecule adsorbed in K-PHI are very similar to their individual adsorption sites. Interestingly, the adsorption of both adsorbates occurs in the pores in the same vacancy between two layers of K-PHI (Fig. 6.1), which indicates an attractive interaction between them. This is confirmed by the calculated adsorption energy of a single helium, where the absolute value is significantly higher in the presence of a water molecule (ΔE_{ads}= -5.3 kJ/mol) than without (ΔE_{ads}= -4.3 kJ/mol). This means that the helium adsorption on wet K-PHI is still thermodynamically favourable and the adsorption affinity can even be increased by adsorbed water molecules. This can be explained by the fact that water acts as a dielectric in the electric field of the cations and PHI layers as it is located directly at the core of the charge separation. In the previous chapter, it was shown that the polarizing environment plays a crucial role in the adsorption process and part of the interaction between water and K-PHI originates from polarization effects. Water is known to have a high relative permittivity (in bulk $\varepsilon_{H_2O} = 87.8$ [91])

and thus the charge separation might be increased in the presence of water. The DDEC6 analysis of the potassium cations supports this argumentation by a slight increase of the partial charge in the presence of water (+0.83) compared with dry K-PHI (+0.82).

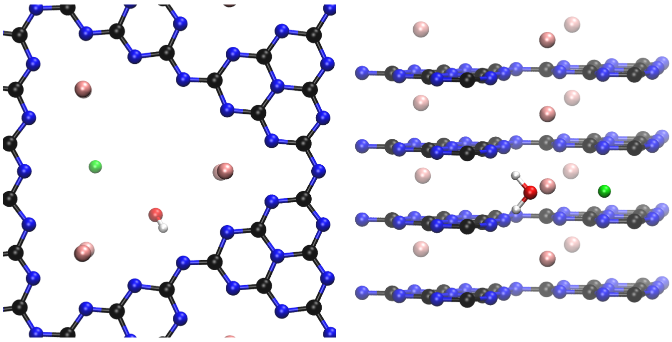

Figure 6.1: Adsorption state of one helium atoms (n=1) and one water molecule (N=1), which both occur in the same layer of K-PHI. Left: top view, right: side view. Atomic colors: C=black; N=blue; K=pink; O=red; H=white; He=green.

6.2 Energy Decomposition Analysis

The ALMO-EDA is also applied to the helium adsorption in K-PHI in the presence of water and compared to adsorption in dry K-PHI. The charge transfers as well as the corresponding energy contributions are shown schematically in Fig. 6.2. As already discussed in Chapter 5, water strongly interacts with the PHI layers and the potassium ions. Regarding the helium adsorption, the calculations suggest that helium is not directly interacting via charge transfer with the water molecule (<0.1 me). Instead, the charge transfer from the helium to the nearest potassium ions is enhanced from 0.30 me (-0.49 kJ/mol) to 0.42 me (-0.68 kJ/mol), which is the main contribution to the stabilization due to charge transfer. It has to be noted that at the same time the charge transfer to the second nearest K^+ decreases from 0.22 me (-0.35 kJ/mol) to 0.11 me (-0.18 kJ/mol). Both charge transfer changes in the presence of H_2O almost cancel out each other and lead to a marginal increase of the charge transfer interaction between helium and the K-PHI material of 0.01 me and stabilization of -0.02 kJ/mol. Hence, according to the calculations, charge transfer does not play a big role for the enhancement. Instead, the frozen and polarization terms are expected to be crucial.

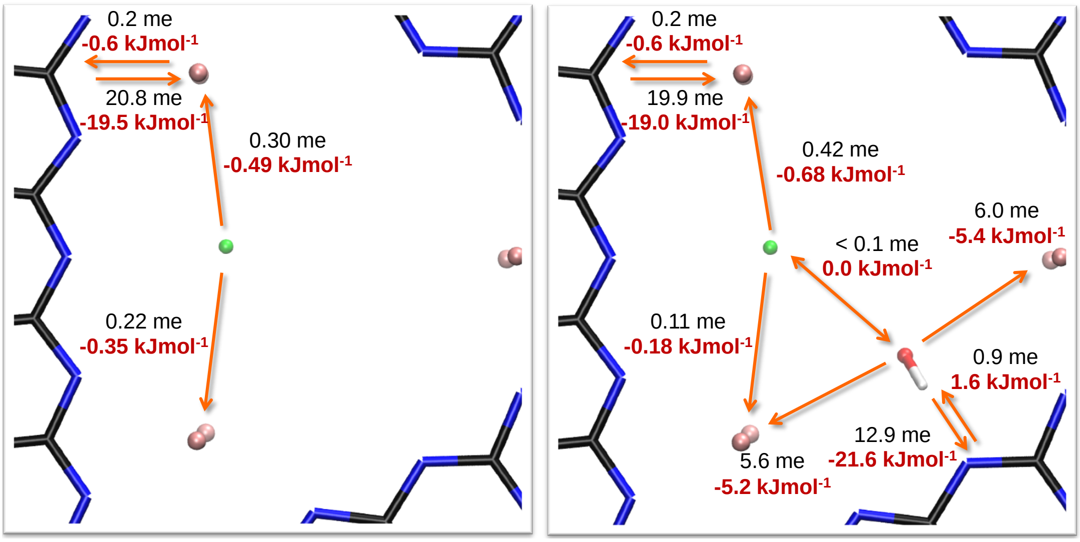

Figure 6.2: Charge transfers (black) and corresponding stabilization energies (red) between the different fragments of adsorbed helium in K-PHI in the absence (left) and presence (right) of water. Atomic colors: C=black; N=blue; K=pink; He=green; O=red; H=white.

6.3 Structures and Energies of Multiple Adsorption of Helium and Water

The helium adsorption is also thermodynamically favorable in the presence of more than one water molecule. The enhancement is quantified by calculating the difference between wet and dry K-PHI $\Delta E^{N}_{ads} - \Delta E^{N=0}_{ads}$ and is shown for single helium adsorption (n=1) in Fig. 6.3a. As can be seen, the enhancement in the range of -0.5 to -1.0 kJ/mol is only found when low amount of water is adsorbed. In this state, one water molecule adsorbs per layer, leading to a total number of water molecules inside the pores of N=4. At these low uptakes, water is adsorbing only on specific sites with a defined structure as discussed in the previous chapter. Hence, the specific adsorption sites of water may play a crucial role in the enhancement process. However, the maximum helium uptake (Fig. 6.3b) as calculated by an incremental adsorption analysis decreases in the presence of water. The highest amount of helium can be adsorbed in K-PHI in the absence of water, where three helium atoms occupy the adsorption sites per pore per layer, leading to the maximum number of adsorbed helium of n_{max}=12. When four water molecules are adsorbed, the maximum number of adsorbed helium atoms is already decreased by one-third

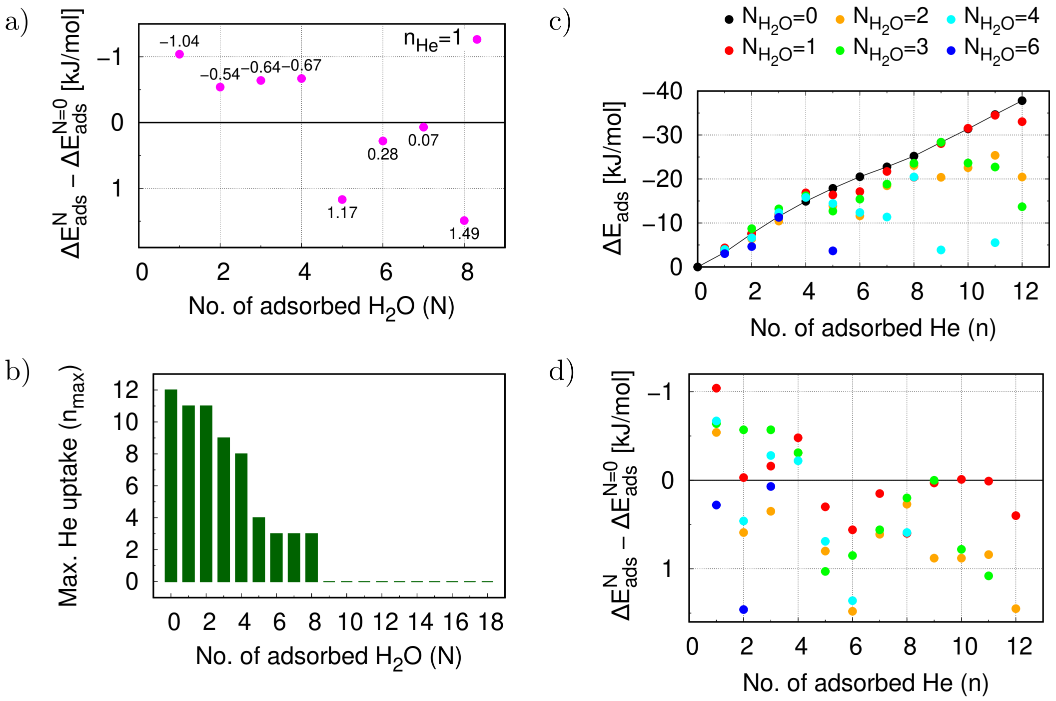

Figure 6.3: The enhancement energy $\Delta E_{ads}^{N} - \Delta E_{ads}^{N=0}$ of single helium adsorption (a) as well as the maximum helium uptake (b) in K-PHI is given with different amount of adsorbed water molecules (N) inside the pores. Furthermore the total adsorption (c) and the enhancement energy (d) are shown for the helium adsorption with respect to different n and N.

to n_{max}=8. This indicates ongoing competition about the adsorption sites in the limited space of the nanopores of K-PHI. The competition increases upon additional water adsorption ($5 \leq N \leq 8$). At these uptakes, helium adsorption is still energetically favorable, however, the enhancement vanishes and the adsorption energy is decreased compared to the dry K-PHI. Due to the same reason, the helium adsorption is no longer energetically favorable at all upon further water adsorption ($N \geq 9$). Furthermore, the total adsorption energies ΔE_{ads} of single and multiple helium adsorption are shown in Fig. 6.3c. The adsorption energies of helium at dry K-PHI $\Delta E_{ads}^{N=0}$ is shown as a black line and used as a reference for the adsorption energies. The adsorption energies of the wet cases are shown in different colors. The maximum uptake corresponds to the calculations, which have the highest absolute values of the adsorption energy ΔE_{ads}. The enhancement energy gives a better visualization of the comparison to dry K-PHI and is shown in Fig. 6.3d. As can be seen, the enhancement effect is not only limited to a small number of water molecules, the helium uptake also has to be small. The enhancement only occurs for up to 4 adsorbed helium atoms. If more than four helium atoms are present, the adsorption might still be thermodynamically favorable in total, however, the adsorption energy is lower than in the dry reference case for all n and N and further decreases when more helium atoms are adsorbed. The derivation from the reference line increases for higher helium uptakes as well as for higher water uptakes due to the space competition. Only a low amount of adsorbed water can compete with the dry K-PHI in the case of more than four adsorbed helium atoms, e. g. N=1 (red).

Hence, the helium affinity is only enhanced when the water molecules are adsorbed in a well-organized fashion at low loadings for a limited number of helium atoms. The enhanced adsorption state, which contains the most adsorbates, includes one water and one helium atom per pore per layer as can be seen in Fig. 6.4 (N=4, n=4). In this case, the adsorption affinity is increased indicated by an adsorption energy decrease of -0.2 kJ/mol. Upon further adsorption the effect vanishes. Due to the competition for the adsorption sites in the narrow pores of the K-PHI material, the adsorption states of the water molecules are less ordered as can be seen for N=8 and n=4. However, the modelled system is idealized and the pore size and hence the available space of the real material are bigger. Therefore, the enhancement effect may also be found at higher uptakes.

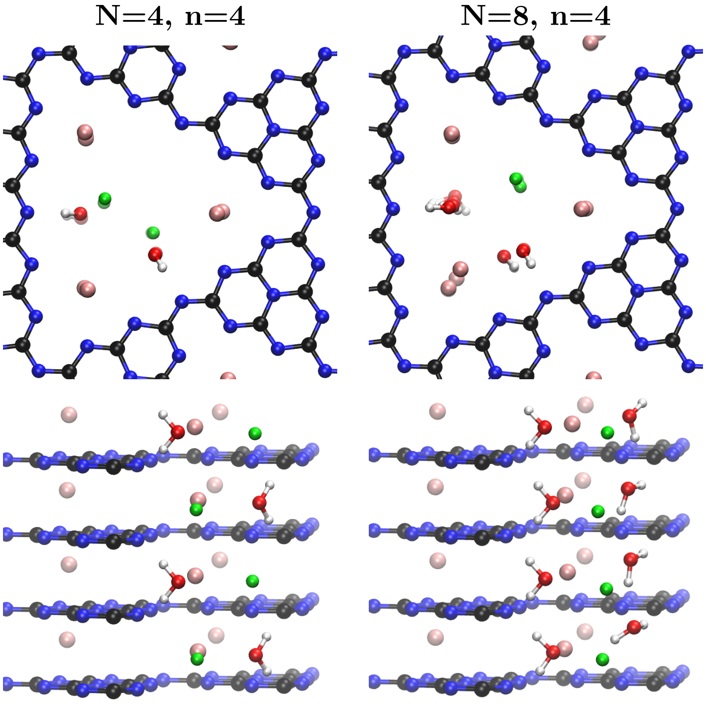

Figure 6.4: Adsorption states of different numbers of helium atoms (n) in the presence of N adsorbed water molecules. Top: top view, bottom: side view. Atomic colors: C=black; N=blue; K=pink; O=red; H=white; He=green.

7 Transport Coefficients of Disordered Crystals

As the scale of the fabrication processes of electronic components is continuously reduced, the quantum mechanical aspects of the charge transport become more important and *ab-initio* quantum simulations will be required for an accurate and predictive characterization. Since most electronic components operate at room and higher temperatures, these *ab-initio* simulations have to take into account the thermal motion of the atoms. Since the dynamics of the electrons is orders of magnitude faster than that of the ionic cores, the quantum dynamics of the electrons takes place in a highly disordered environment. This can result in qualitatively different dynamical behaviors, notably the absence of quantum diffusion or Anderson localization [92], that can not be captured by empirical models or idealistic zero temperature simulations. This and other effects will be investigated from first-principles in this work. To the best of our knowledge, the work reported here is the first attempt to simulate quantum charge transport at finite-temperature from first-principles.

Most of us think of crystals as condensed phases of matter, where the atoms are periodically arranged in space. However, the crystalline phase persists all the way to the melting point so clearly that oversimplifying picture is highly misleading. In fact, defining the crystalline phase is a deep and highly non-trivial problem in condensed matter physics. On the formalism side, the works of Bellissard on the homogeneous phases of matter represent a milestone [93, 94]. They taught us that, in crystals, the space group symmetry $\mathbb{G}$ manifested at zero temperature is replaced at finite temperatures by an ergodic $\mathbb{G}$-action w.r.t. the Gibbs measure on the space Ω of thermally disordered atomic configurations. Furthermore, the invariance w.r.t. $\mathbb{G}$ of the electronic Hamiltonians manifested at zero temperature is replaced at finite temperatures by the covariance w.r.t. the $\mathbb{G}$-action. Ergodicity and covariance w.r.t. the $\mathbb{G}$-action explain why the measurements of the macroscopic physical observables, including the transport coefficients, do not fluctuate from one configuration to another and why the symmetry w.r.t. the full space group is restored at the macroscopic level. For example, the latter is manifested in the $\mathbb{G}$-symmetric X-ray diffraction patterns observed all the way to the melting point [95]. Another manifestation is the stability of the topological phases of matter stabilized by point symmetries in conditions where thermal disorder breaks these symmetries [96].

In our previous work [97], we took the task of quantifying the ergodic dynamical system $(\Omega, \mathbb{G}, \tau, \mathrm{d}\mathbb{P})$ that defines a crystalline phase. Using crystal silicon (Si) as a working example, we devised an algorithm that extracts this data from the output of conventional *ab-initio* molecular dynamics (AIMD) simulations [98, 99]. In particular, we were able to quantify and parametrize the Gibbs measure for crystalline Si at various temperatures. In this work, our focus is mostly on the electronic degrees of freedom, which are simulated with hybrid Gaussian-plane wave based density functional theory (DFT) electronic structure codes [100]. In the first part of our work, we demonstrate how to generate effective lattice models that encode the entire output of the electronic structure codes and where the covariance w.r.t. $(\Omega, \mathbb{G}, \tau, \mathrm{d}\mathbb{P})$ is explicitly manifested. Particular attention will be dedicated to the tight-binding expressions of the Kohn-Sham (KS) Hamiltonian, position and charge current operators.

For the charge transport, we adopt the non-commutative Kubo-formula derived by Schulz-Baldes and Bellissard [101–103]. One extremely important aspect of their formalism is that it includes dissipation. More precisely, given a dissipation mechanism encoded in a scattering operator, the formalism produces a dissipation super-operator that is organically incorporated in the Kubo-formula (see Section 7.3.2). Various dissipation mechanisms and their corresponding super-operators have been analyzed in [104] and they certainly can be evaluated from first principles. One should be aware that dissipation has an important role in shaping the I-V characteristics of both metals and semiconductors and this is why a Kubo-formula that incorporates dissipation is so valuable.

The Kubo-formula derived by Schulz-Baldes and Bellissard has been numerically implemented in the past for disordered tight-binding model Hamiltonians [105–110] and other types of aperiodic Hamiltonians [111–113]. One of the main findings of these works is the rapid convergence of the results with system size. For example, in systems with known quantized transport coefficients, such as 2-dimensional Hall systems, the non-commutative Kubo-formula reproduced the quantization with two digits of precision even on small 10×10 highly disordered tight-binding lattices. This is a convincing fact that this approach is highly suited for the applications we seek in this work, given that the super-cells that can be handled by first-principles simulations are inherently small.

The simulations we report here for crystalline Si at different temperatures are preliminary and certainly not converged w.r.t. either the system's size, or the atomic orbital basis, but they are certainly converged w.r.t. the thermal disorder sampling. Also, the dissipation super-operator is treated in the relaxation time approximation where it becomes proportional to the identity map. The simulations produced expected outputs for the available electronic structures and enabled us to test several important qualitative aspects of the charge transport. One aspect is the formation of a dynamical band gap where the quantum diffusion is absent and this dynamical gap was found to be much larger than the spectral gap. The former defines the reference for the activated behavior of the conductivity, while the latter for the charge carriers. Since these are two different reference energy levels, the Anderson localization phenomenon can lead to substantial quantitative effects that were overlooked so far. We also found that the conductivity tensor is extremely sensitive to the dissipation relaxation time. Given this sensitivity, we believe that the prevalent dissipation mechanism in crystalline Si at room temperature can be identified with high precision by future simulations which incorporate first principles dissipation super-operators.

Based on previous tight-binding model simulations, we initially estimated that at least 1000 disordered atomic configurations will be necessary and, as such, we performed large time scale AIMD simulations to acquire that amount of data. However, our calculations revealed that the average over the atomic configurations of the conductivity tensor can be achieved with a relatively small number of configurations, which can be as low as 50. In fact, with reasonable level of dissipation, the thermal fluctuations are almost entirely suppressed for the largest crystal we simulated, which is a direct manifestation of the self-averaging property of the Kubo-formula. This finding assures us that, in the future simulations, we can reduce the time scale of AIMD simulations, hence, enabling us to further increase the crystal size and to better optimize the orbital basis.

7.1 Thermal Disorder from First Principles

In order to fix our notations and provide the context for the present calculations, we briefly recall our main results reported in [97]. Therein, we describe the ergodic dynamical system $(\Omega, \mathbb{G}, \tau, \mathrm{d}\mathbb{P})$, which completely characterizes the crystalline phase of Si at finite-temperature, where Ω is the atomic configuration space, $\mathbb{G}$ is the space group, $\mathrm{d}\mathbb{P}$ is the Gibbs measure and τ is an ergodic action of $\mathbb{G}$ on Ω.

7.1.1 The ideal lattice and its symmetries

The crystal structure of Si is summarized in Fig. 7.1. Its space group is $\mathbb{G} = Fd\bar{3}\mathrm{m}$ [114, 115], whose structure is summarized by the following exact sequence of groups

$$1 \to \mathcal{B} \to \mathbb{G} \to \mathcal{P} \to 1, \tag{7.1.1}$$

capturing the extension of the point group $\mathcal{P} \subset O(3)$ by the group of discrete translations $\mathcal{B}$. The latter can be pictured as the Bravais lattice of the crystal (hence our notation $\mathcal{B}$), *i.e.* the discrete sub-group of $\mathbb{R}^3$ defined by the centers of the primitive cells

$$\mathcal{B} = \big\{ n_1 \boldsymbol{a}_1 + n_2 \boldsymbol{a}_2 + n_3 \boldsymbol{a}_3,\ \boldsymbol{n} = (n_1, n_2, n_3) \in \mathbb{Z}^3 \big\}, \tag{7.1.2}$$

with the generators $\boldsymbol{a}_i$ supplied in Fig. 7.1. The point group $\mathcal{P}$ of crystalline Si is O_h^7, the full symmetry group of the cube.

Let us recall that a space group is called symmorphic if the exact sequence (7.1.1) is split. Silicon's cubic-diamond lattice is an example of a non-symmorphic space group. Nevertheless, every element $\mathfrak{g}$ of $\mathbb{G}$ can be presented in the form $\mathfrak{g} = (\mathfrak{p}|\mathfrak{a})$, with $\mathfrak{p} \in \mathcal{P}$ and $\mathfrak{a} \in \mathbb{R}^3$. Note that for a symmorphic space group, $\mathfrak{a}$ can be always drawn from $\mathcal{B}$, but this is not the case here. Such space group elements act on the points of the Euclidean space as

$$(\mathfrak{p}|\mathfrak{a})\boldsymbol{x} = \mathfrak{p}\boldsymbol{x} + \mathfrak{a}, \quad \boldsymbol{x} \in \mathbb{R}^3. \tag{7.1.3}$$

They also act on any subset $\mathcal{L}$ of the Euclidean space, such as a lattice, via

$$\mathfrak{g}\mathcal{L} = \{\mathfrak{g}\boldsymbol{x},\ \boldsymbol{x} \in \mathcal{L}\}. \tag{7.1.4}$$

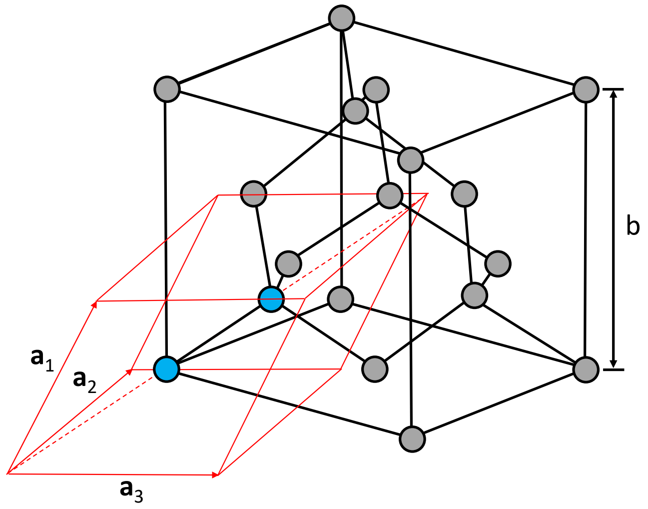

Figure 7.1: Si crystallizes in a diamond cubic lattice (Fd-3m), whose conventional unit cell is shown in this diagram. This cubic unit cell is symmetric to the full point group and contains eight Si atoms. The diamond cubic lattice results from the interpenetration of two face-centered cubic (fcc) lattices. The fcc lattice can be generated by translating a primitive cell that contains just one atom. Hence, silicon's diamond cubic lattice can be generated by translating the same primitive cell, but with one additional Si atom inside it. This primitive cell is shown in red, together with its two atoms (blue disks) and the generating primitive vectors $\boldsymbol{a}_1 = \frac{b}{2}(\hat{z}+\hat{y})$, $\boldsymbol{a}_2 = \frac{b}{2}(\hat{x}+\hat{z})$ and $\boldsymbol{a}_3 = \frac{b}{2}(\hat{y}+\hat{x})$, with $b = 5.431$ Å. The magnitude of the primitive vectors is $a = b/\sqrt{2}$.

The multiplication of the elements takes the form

$$(\mathfrak{p}|\mathfrak{a})(\mathfrak{p}'|\mathfrak{a}') = (\mathfrak{p}\mathfrak{p}'|\mathfrak{p}\mathfrak{a}' + \mathfrak{a}) \tag{7.1.5}$$

and the inverse of an element is

$$(\mathfrak{p}|\mathfrak{a})^{-1} = (\mathfrak{p}^{-1}| - \mathfrak{p}^{-1}\mathfrak{a}). \tag{7.1.6}$$

The ideal or zero temperature Si lattice will be denoted by $\mathcal{L}_0$. This lattice is left invariant by the space group $\mathbb{G}$. In fact, the asymmetric unit cell of the diamond cubic structure contains a single atom [114, 115], which means that the entire lattice can be reconstructed from one single point by acting with the full space group: $\mathcal{L}_0 = \big\{\mathfrak{g}\cdot\boldsymbol{x}_0,\ \boldsymbol{g}\in\mathbb{G}\big\}$. While $\boldsymbol{x}_0$ can be any point of the Euclidean space, we will fix $\boldsymbol{x}_0$ at the origin.

7.1.2 Thermally disordered configurations

When the temperature is finite, the Si atoms undergo a thermal motion and the instantaneous snapshots of the Si lattice can be labeled by a configuration space Ω. In [97], Ω was found to be well represented by a product of identical balls

$$\Omega = \prod_{\mathfrak{g} \in \mathbb{G}} B_{\mathfrak{g}}, \quad B_{\mathfrak{g}} = B_0, \tag{7.1.7}$$

where a point $\omega = \{\omega_{\mathfrak{g}}\}_{\mathfrak{g} \in \mathbb{G}}$ of Ω encodes the displacements of the atoms from their equilibrium positions. Thermal motion defines an ergodic dynamical system $\omega(t)$ (t = time) over Ω and an instantaneous snapshot of crystalline Si supplies a thermally disordered lattice

$$\mathcal{L}_\omega = \big\{ \mathfrak{g}\boldsymbol{x}_0 + \omega_{\mathfrak{g}}, \ \mathfrak{g} \in \mathbb{G} \big\} \subset \mathbb{R}^3. \tag{7.1.8}$$

For these disordered lattices, the invariance of $\mathcal{L}_0$ under the space group is replaced by the covariance relation

$$\mathfrak{g}\mathcal{L}_\omega = \mathcal{L}_{\tau_{\mathfrak{g}}\omega}, \quad \forall\, \omega \in \Omega, \quad \mathfrak{g} \in \mathbb{G}. \tag{7.1.9}$$

The action τ of the space group on Ω, appearing above, can be computed as follows. If $\mathfrak{g} = (\mathfrak{p}|\mathfrak{a}) \in \mathbb{G}$, then

$$\begin{aligned} \mathfrak{g}\mathcal{L}_\omega &= \{ \mathfrak{g}(\mathfrak{g}'\boldsymbol{x}_0 + \omega_{\mathfrak{g}'}), \ \mathfrak{g}' \in \mathbb{G} \} \\ &= \{ \mathfrak{p}(\mathfrak{g}'\boldsymbol{x}_0) + \mathfrak{p}\omega_{\mathfrak{g}'} + \mathfrak{a}, \ \mathfrak{g}' \in \mathbb{G} \}. \end{aligned} \tag{7.1.10}$$

After regrouping,

$$\mathfrak{p}(\mathfrak{g}'\boldsymbol{x}_0) + \mathfrak{p}\omega_{\mathfrak{g}'} + \mathfrak{a} = \mathfrak{g}\mathfrak{g}'\boldsymbol{x}_0 + \mathfrak{p}\omega_{\mathfrak{g}'}, \tag{7.1.11}$$

and, after the change of variable $\mathfrak{g}' \to \mathfrak{g}^{-1}\mathfrak{g}'$, we have

$$\mathfrak{g}\mathcal{L}_\omega = \{ \mathfrak{g}'\boldsymbol{x}_0 + \mathfrak{p}\omega_{\mathfrak{g}^{-1}\mathfrak{g}'}, \ \mathfrak{g}' \in \mathbb{G} \} = \mathcal{L}_{\tau_{\mathfrak{g}}\omega}. \tag{7.1.12}$$

We now can identify the action as

$$\tau_{\mathfrak{g}}\omega = \tau_{\mathfrak{g}}\{\omega_{\mathfrak{g}'}\}_{\mathfrak{g}' \in \mathbb{G}} = \{\omega'_{\mathfrak{g}'}\}_{\mathfrak{g}' \in \mathbb{G}}, \quad \omega'_{\mathfrak{g}'} = \mathfrak{p}\omega_{\mathfrak{g}^{-1}\mathfrak{g}'}. \tag{7.1.13}$$

One can verify that $\tau_{\mathfrak{g}_1}\tau_{\mathfrak{g}_2} = \tau_{\mathfrak{g}_1\mathfrak{g}_2}$, as it should be for a group action.

The Gibbs measure over the configuration space Ω can be computed from the atomic orbits in an AIMD simulation, more precisely, from the histograms encoding the number of times an orbit intersects the elementary volumes of Ω. In [97], the Gibbs measure of the Si crystal was found to be extremely well characterized by a multivariate normal distribution of zero mean

$$\mathrm{d}\mathbb{P}(\omega) = \rho(\omega)\mathrm{d}\omega, \quad \rho(\omega) = \frac{1}{\sqrt{\mathrm{Det}(2\pi\hat{\Sigma})}} e^{-\frac{1}{2}\omega^T\hat{\Sigma}^{-1}\omega}, \tag{7.1.14}$$

where ω is seen here as a 1-column matrix and the variance matrix $\hat{\Sigma}$ was quantified in [97] as a function of temperature. The Gibbs measure is invariant and ergodic w.r.t. the τ-action. In fact, the Gibbs measure found in [97] is ergodic relative to the subgroup $\mathcal{B}$ of translations, which is in fact a generic property of homogeneous systems at thermodynamic equilibrium [116, Chap. 6]. The crystalline phase of Si at finite-temperature is entirely defined by the ergodic dynamical system $(\Omega, \mathbb{G}, \tau, \mathrm{d}\mathbb{P})$.

The observations of the last paragraph will play an important role for the self-averaging properties of the transport coefficients. Let us stress again that, due to the well separated scales in the dynamics of the atomic and electronic degrees of freedom, the quantum state of the electrons evolves in a static atomic potential.[1] This is a thermally disordered potential and, as we shall see, the physical observables, such as the Hamiltonians or charge currents, become indexed by points of the configuration space Ω. In this new context, the notion of a symmetric observable is replaced by that of a covariant observable. The macroscopic measurements of these observables, however, are independent of the thermally disordered configuration. This remarkable property is a consequence of the covariance and of the ergodic character of the Gibbs measure.

7.2 Tight-Binding Form of the Physical Observables

Our goal for this section is to formulate discrete representations of the Hamiltonians and other physical observables in the context of Gaussian-based implementations of the KS program. Special attention will be given to the transformation of

---

[1] The electron-phonon and electron-electron scattering processes are rare and sudden dynamical events, which are included via Poisson processes as explained later.

the physical observables under the space group $\mathbb{G}$ of the crystal.

7.2.1 The continuum theory

The formally exact KS theory for condensed matter systems, at its most fundamental level, is formulated over the Hilbert space $L^2(\mathbb{R}^3)$ of square integrable wave functions [117]. For the Si crystal in a thermally disordered configuration ω, the KS-Hamiltonian takes the form

$$H_{\mathrm{KS}}^{\omega} = -\frac{\hbar^2}{2m}\boldsymbol{\nabla}_{\boldsymbol{r}}^2 - \sum_{\boldsymbol{x}\in\mathcal{L}_\omega} \frac{Ze^2}{|\boldsymbol{r}-\boldsymbol{x}|} + V_{\mathrm{xc}}[n_\omega](\boldsymbol{r}), \tag{7.2.1}$$

where V_{xc} is a local potential encoding the exchange and correlation (XC) effects. The latter has a functional dependence on the electron density $n_\omega(\boldsymbol{r})$, which is to be determined self-consistently. As the notation suggests, the electron density has a dependence on the atomic configuration ω. In fact, this becomes even more apparent if we reformulate (7.2.1) as a fixed point problem

$$n_\omega(\boldsymbol{r}) = \langle \boldsymbol{r}|\Phi_{\mathrm{FD}}\big(H_{\mathrm{KS}}^{\omega}; T, \mu\big)|\boldsymbol{r}\rangle, \tag{7.2.2}$$

where Φ_{FD} is the Fermi-Dirac distribution at temperature T and chemical potential μ [118]. In the following, we assume that this equation has a unique solution for almost all thermally disordered configuration (see [119] and [120]).

The starting point of our study is the covariant property of the KS-Hamiltonian under the space group transformations. To understand the origin of this property, we need to go all the way to the Euclidean group $\mathbb{E}$ of transformations and recall that the XC potential enjoys the following property

$$V_{\mathrm{xc}}[n \circ \mathfrak{e}](\mathfrak{e}^{-1}\boldsymbol{r}) = V_{\mathrm{xc}}[n](\boldsymbol{r}), \quad \mathfrak{e} \in \mathbb{E}, \tag{7.2.3}$$

for any density function n and point $\boldsymbol{r} \in \mathbb{R}^3$, which can be inferred from the universality and uniqueness assumptions on V_{xc} [121]. Certainly, this can be verified directly for the local density approximation (LDA) to V_{xc} [122]. The action of $\mathbb{E}$ on $\mathbb{R}^3$ lifts to a unitary action on the Hilbert space $L^2(\mathbb{R}^2)$ via

$$\big(T_{\mathfrak{e}}\psi\big)(\boldsymbol{r}) = \psi(\mathfrak{e}^{-1}\boldsymbol{r}), \quad \mathfrak{e} \in \mathbb{E}, \quad \psi \in L^2(\mathbb{R}^3). \tag{7.2.4}$$

Now, recall that $\mathbb{G}$ is just a subgroup of the Euclidean group, hence (7.2.4) describes the action of $\mathbb{G}$ as well. Then, under such unitary actions, the KS-Hamiltonian behaves as

$$T_{\mathfrak{g}} H_{\mathrm{KS}}^{\omega} T_{\mathfrak{g}}^{\dagger} = -\frac{\hbar^2}{2m} \boldsymbol{\nabla}^2_{\mathfrak{g}^{-1}\boldsymbol{r}} - \sum_{\boldsymbol{x} \in \mathcal{L}_\omega} \frac{Ze^2}{|\mathfrak{g}^{-1}\boldsymbol{r} - \boldsymbol{x}|} + V_{\mathrm{xc}}[n_\omega](\mathfrak{g}^{-1}\boldsymbol{r}) \tag{7.2.5}$$

$$= -\frac{\hbar^2}{2m} \boldsymbol{\nabla}^2_{\boldsymbol{r}} - \sum_{\boldsymbol{x} \in \mathcal{L}_{\mathfrak{g}\omega}} \frac{Ze^2}{|\boldsymbol{r} - \boldsymbol{x}|} + V_{\mathrm{xc}}[n_\omega \circ \mathfrak{g}^{-1}](\boldsymbol{r}). \tag{7.2.6}$$

We learn from here that, if n_ω is the solution of (7.2.2) for configuration ω, then $n_\omega \circ \mathfrak{g}^{-1}$ is the solution of (7.2.2) for configuration $\mathfrak{g}\omega$. In other words, the self-consistent solutions of the KS equations enjoy the covariant property

$$n_{\mathfrak{g}\omega} = n_\omega \circ \mathfrak{g}^{-1}. \tag{7.2.7}$$

In turn, this assures us that the converged KS-Hamiltonian satisfies the covariant relation

$$T_{\mathfrak{g}} H_{\mathrm{KS}}^{\omega} T_{\mathfrak{g}}^{\dagger} = H_{\mathrm{KS}}^{\tau_{\mathfrak{g}}\omega}, \quad \forall\, \mathfrak{g} \in \mathbb{G}. \tag{7.2.8}$$

It will be extremely important to preserve this characteristics in our tight-binding approximation. As we already mentioned, (7.2.8) together with the ergodicity of the space group action ensure the self-averaging of the transport coefficients.

7.2.2 The effective Hilbert space

In Gaussian-based approaches, the atom located at position $\boldsymbol{x} \in \mathcal{L}_\omega$ carries a finite-dimensional local Hilbert space

$$\mathcal{H}_{\boldsymbol{x}} = \mathrm{Span}\big\{\phi_n(\boldsymbol{r} - \boldsymbol{x}),\ n = 1, \dots N\big\}, \tag{7.2.9}$$

where $\phi_n : \mathbb{R}^3 \to \mathbb{C}$ are optimized atomic orbitals (see Section 7.4.2 for details). It is important to realize that the same set of functions ϕ_n are used for all $\boldsymbol{x} \in \mathcal{L}_\omega$. The total Hilbert space for the Gaussian-based computations is the linear subspace

$$\mathcal{H}_\omega = \overline{\mathrm{Span}}\big\{\mathcal{H}_{\boldsymbol{x}},\ \boldsymbol{x} \in \mathcal{L}_\omega\big\} \subset L^2(\mathbb{R}^3). \tag{7.2.10}$$

As the notation suggests, this subspace depends on the configuration $\omega \in \Omega$ of the atoms. As we shall see, it is isomorphic to the tight-binding Hilbert space

$$\mathbb{C}^N \otimes \ell^2(\mathcal{L}_\omega) = \overline{\mathrm{Span}}\big\{\xi \otimes |\boldsymbol{x}\rangle,\ \xi \in \mathbb{C}^N,\ \boldsymbol{x} \in \mathcal{L}_\omega\big\} \tag{7.2.11}$$

of square summable linear combinations of $\xi \otimes |\boldsymbol{x}\rangle$ basis vectors. The scalar product for this space is defined by the orthonormality condition

$$\langle \boldsymbol{x}|\boldsymbol{x}'\rangle = \delta_{\boldsymbol{x},\boldsymbol{x}'}, \quad \forall\ \boldsymbol{x}, \boldsymbol{x}' \in \mathcal{L}_\omega. \tag{7.2.12}$$

All our physical observables will be mapped over this tight-binding Hilbert space and all the calculations will be ultimately performed on $\mathbb{C}^N \otimes \ell^2(\mathcal{L}_\omega)$.

Our goal for this section is to explain in details how to transfer the observables between the Hilbert spaces. We start with the consideration of the overlap coefficients

$$S^{ij}_{\boldsymbol{x}\boldsymbol{x}'}(\omega) = \int_{\mathbb{R}^3} \mathrm{d}^3\boldsymbol{r}\ \phi_i^*(\boldsymbol{r}-\boldsymbol{x})\phi_j(\boldsymbol{r}-\boldsymbol{x}'), \tag{7.2.13}$$

which can be found among the outputs of standard AIMD simulations. Using these coefficients, we form the self-adjoint, positive and invertible operator

$$\begin{aligned} &S_\omega : \mathbb{C}^N \otimes \ell^2(\mathcal{L}_\omega) \to \mathbb{C}^N \otimes \ell^2(\mathcal{L}_\omega), \\ &S_\omega = \sum_{\boldsymbol{x},\boldsymbol{x}' \in \mathcal{L}} \widehat{S}_{\boldsymbol{x},\boldsymbol{x}'}(\omega) \otimes |\boldsymbol{x}\rangle\langle \boldsymbol{x}'|, \end{aligned} \tag{7.2.14}$$

where $\widehat{S}_{\boldsymbol{x},\boldsymbol{x}'}(\omega)$ is the overlap matrix with the entries $S^{ij}_{\boldsymbol{x},\boldsymbol{x}'}(\omega)$ defined in (7.2.13). Then, the isomorphism between $\mathcal{H}_\omega$ and $\mathbb{C}^N \otimes \ell^2(\mathcal{L}_\omega)$ is supplied by the unique linear map U_ω that acts on the generators as

$$\phi_n(\boldsymbol{r}-\boldsymbol{x}) \mapsto \sqrt{S_\omega}\ \xi_n \otimes |\boldsymbol{x}\rangle, \quad n = 1, \dots N. \tag{7.2.15}$$

Above, $\xi_n \in \mathbb{C}^N$ is a column vector, whose entries are one at position n and zero for all others, whereas $\sqrt{S_\omega}$ is the square root operator defined via the functional calculus. Let us verify that the map indeed preserves the scalar product. We have

$$\begin{aligned} \big(\sqrt{S_\omega}\,\xi_i \otimes |\boldsymbol{x}\rangle, \sqrt{S_\omega}\,\xi_j \otimes |\boldsymbol{x}'\rangle\big) &= \big(\xi_i \otimes |\boldsymbol{x}\rangle, S_\omega \xi_j \otimes |\boldsymbol{x}'\rangle\big) \\ &= \xi_i^T \widehat{S}_{\boldsymbol{x},\boldsymbol{x}'}(\omega)\xi_j = S^{ij}_{\boldsymbol{x},\boldsymbol{x}'}(\omega). \end{aligned} \tag{7.2.16}$$

As a consequence,

$$\big(\sqrt{S_\omega}\,\xi_i \otimes |\boldsymbol{x}\rangle, \sqrt{S_\omega}\,\xi_j \otimes |\boldsymbol{x}'\rangle\big) = \int_{\mathbb{R}^3} \mathrm{d}^3\boldsymbol{r}\ \phi_i^*(\boldsymbol{r}-\boldsymbol{x})\phi_j(\boldsymbol{r}-\boldsymbol{x}'), \tag{7.2.17}$$

for all $i, j = 1, \dots, N$, as desired.

To preserve the covariance of the physical observables w.r.t. the space group $\mathbb{G}$ and the disordered configurations, it is important to choose the atomic orbitals as such that they span a linear space, which is closed under representations of the $O(3)$ group. Thus, all ϕ_n are assumed to transform under rotations as

$$(\phi_1, \dots, \phi_N) \circ \mathfrak{r}^{-1} = (\phi_1, \dots, \phi_N)\widehat{\mathcal{D}}(\mathfrak{r}), \quad \mathfrak{r} \in O(3) \subset \mathbb{E}, \tag{7.2.18}$$

where $\{\widehat{\mathcal{D}}(\mathfrak{r}),\ \mathfrak{r} \in O(3)\}$ is a family of $N \times N$ matrices supplying a N-dimensional unitary representation of the rotation group that is not necessarily irreducible (see Section 7.4.2 for details). Then, if $\mathfrak{g} = (\mathfrak{p}|\mathfrak{a}) \in \mathbb{G}$, the overlap matrix satisfies the relation

$$\widehat{\mathcal{D}}(\mathfrak{p})^\dagger \widehat{S}_{\mathfrak{g}\boldsymbol{x},\mathfrak{g}\boldsymbol{x}'}(\tau_{\mathfrak{g}}\omega)\widehat{\mathcal{D}}(\mathfrak{p}) = \widehat{S}_{\boldsymbol{x},\boldsymbol{x}'}(\omega), \tag{7.2.19}$$

for any $\boldsymbol{x}$ and $\boldsymbol{x}'$ in $\mathcal{L}_\omega$. This is an important relation for which we provide the derivation below. Indeed, both $\mathfrak{g}\boldsymbol{x}$ and $\mathfrak{g}\boldsymbol{x}'$ belong to $\mathfrak{g}\mathcal{L}_\omega = \mathcal{L}_{\tau_{\mathfrak{g}}\omega}$ and

$$\begin{aligned} S^{ij}_{\mathfrak{g}\boldsymbol{x},\mathfrak{g}\boldsymbol{x}'}(\tau_{\mathfrak{g}}\omega) &= \int_{\mathbb{R}^3} \mathrm{d}^3\boldsymbol{r}\ \phi_i^*(\boldsymbol{r}-\mathfrak{g}\boldsymbol{x})\phi_j(\boldsymbol{r}-\mathfrak{g}\boldsymbol{x}') \\ &= \int_{\mathbb{R}^3} \mathrm{d}^3(\mathfrak{g}\boldsymbol{r})\ \phi_i^*(\mathfrak{g}\boldsymbol{r}-\mathfrak{g}\boldsymbol{x})\phi_j(\mathfrak{g}\boldsymbol{r}-\mathfrak{g}\boldsymbol{x}'). \end{aligned} \tag{7.2.20}$$

Since $\mathfrak{g}\boldsymbol{r} - \mathfrak{g}\boldsymbol{x} = \mathfrak{p}(\boldsymbol{r}-\boldsymbol{x})$ and $\mathrm{d}^3(\mathfrak{g}\boldsymbol{r}) = \mathrm{d}^3\boldsymbol{r}$, we can continue as

$$\begin{aligned} S^{ij}_{\mathfrak{g}\boldsymbol{x},\mathfrak{g}\boldsymbol{x}'}(\tau_{\mathfrak{g}}\omega) &= \int_{\mathbb{R}^3} \mathrm{d}^3\boldsymbol{r}\ \phi_i^*\big(\mathfrak{p}(\boldsymbol{r}-\boldsymbol{x})\phi_j\big(\mathfrak{p}(\boldsymbol{r}-\boldsymbol{x}'\big) \\ &= \int_{\mathbb{R}^3} \mathrm{d}^3\boldsymbol{r}\ \mathcal{D}(\mathfrak{p}^{-1})^*_{ki}\phi_k^*(\boldsymbol{r}-\boldsymbol{x})\phi_s(\boldsymbol{r}-\boldsymbol{x}')\mathcal{D}(\mathfrak{p}^{-1})_{sj} \\ &= \mathcal{D}(\mathfrak{p})_{ik}\int_{\mathbb{R}^3} \mathrm{d}\boldsymbol{r}\ \phi_k^*(\boldsymbol{r}-\boldsymbol{x})\phi_s(\boldsymbol{r}-\boldsymbol{x}')\mathcal{D}(\mathfrak{p})^*_{js}, \end{aligned} \tag{7.2.21}$$

and (7.2.19) follows.

For any $\omega \in \Omega$, we define a Hilbert space isomorphism between $\mathbb{C}^N \otimes \ell^2(\mathcal{L}_\omega)$ and

$\mathbb{C}^N \otimes \ell^2(\mathcal{L}_{\tau_{\mathfrak{g}}\omega})$ as

$$T_{\mathfrak{g}}\big(\xi \otimes |\boldsymbol{x}\rangle\big) = \widehat{\mathcal{D}}(\mathfrak{p})\xi \otimes |\mathfrak{g}\boldsymbol{x}\rangle, \quad \mathfrak{g} = (\mathfrak{p}|\mathfrak{a}) \in \mathbb{G}, \quad \boldsymbol{x} \in \mathcal{L}_\omega. \tag{7.2.22}$$

Note that we use here the same notation as in (7.2.4) because these two maps can be easily differentiated from the context. Now, by examining the rule of multiplication in (7.1.5) for the space group, it is immediate to see that T respect this binary operation: $T_{\mathfrak{g}}T_{\mathfrak{g}'} = T_{\mathfrak{g}\mathfrak{g}'}$. Furthermore, it follows directly from (7.2.19) and the definition (7.2.14) that

$$T_{\mathfrak{g}} S_\omega T_{\mathfrak{g}}^\dagger = S_{\tau_{\mathfrak{g}}\omega}, \quad \mathfrak{g} \in \mathbb{G}. \tag{7.2.23}$$

Indeed, if $\mathfrak{g} = (\mathfrak{p}|\mathfrak{a})$, then

$$\begin{aligned} T_{\mathfrak{g}} S_\omega T_{\mathfrak{g}}^\dagger &= \sum_{\boldsymbol{x},\boldsymbol{x}' \in \mathcal{L}_\omega} \widehat{D}(\mathfrak{p})\widehat{S}_{\boldsymbol{x},\boldsymbol{x}'}(\omega)\widehat{D}(\mathfrak{p})^\dagger \otimes |\mathfrak{g}\boldsymbol{x}\rangle\langle \mathfrak{g}\boldsymbol{x}'| \\ &= \sum_{\boldsymbol{x},\boldsymbol{x}' \in \mathcal{L}_{\tau_{\mathfrak{g}}\omega}} \widehat{D}(\mathfrak{p}^{-1})^\dagger \widehat{S}_{\mathfrak{g}^{-1}\boldsymbol{x},\mathfrak{g}^{-1}\boldsymbol{x}'}(\omega)\widehat{D}(\mathfrak{p}^{-1}) \otimes |\boldsymbol{x}\rangle\langle \boldsymbol{x}'|. \end{aligned} \tag{7.2.24}$$

Furthermore, from (7.2.19),

$$\widehat{D}(\mathfrak{p}^{-1})^\dagger \widehat{S}_{\mathfrak{g}^{-1}\boldsymbol{x},\mathfrak{g}^{-1}\boldsymbol{x}'}(\omega)\widehat{D}(\mathfrak{p}^{-1}) = \widehat{S}_{\boldsymbol{x},\boldsymbol{x}'}(\tau_{\mathfrak{g}}\omega), \tag{7.2.25}$$

hence (7.2.23) follows.

We conclude this section with the observation that the map U_ω, defined in (7.2.15), satisfies the covariant relation $U_{\tau_{\mathfrak{g}}\omega}T_{\mathfrak{g}} = T_{\mathfrak{g}}U_\omega$. Indeed, for $\boldsymbol{x} \in \mathcal{L}_\omega$,

$$\phi_j(\mathfrak{g}^{-1}\boldsymbol{r} - \boldsymbol{x}) = \phi_j\big(\mathfrak{p}^{-1}(\boldsymbol{r} - \mathfrak{g}\boldsymbol{x})\big) = \sum_{k=1}^N \phi_k(\boldsymbol{r} - \mathfrak{g}\boldsymbol{x})\mathcal{D}(\mathfrak{p})_{kj}, \tag{7.2.26}$$

while

$$T_{\mathfrak{g}}\sqrt{S_\omega}\,\xi_j \otimes |\boldsymbol{x}\rangle = \sqrt{S_{\tau_{\mathfrak{g}}\omega}}\,\widehat{\mathcal{D}}(\mathfrak{p})\xi_j \otimes |\mathfrak{g}\boldsymbol{x}\rangle = \sum_{k=1}^N \sqrt{S_{\tau_{\mathfrak{g}}\omega}}\,\xi_k \otimes |\mathfrak{g}\boldsymbol{x}\rangle\mathcal{D}(\mathfrak{p})_{kj}. \tag{7.2.27}$$

Then, by applying rule (7.2.15) on each terms of the two sums, one can convince oneself that we have the following correspondence

$$\phi_j(\mathfrak{g}^{-1}\boldsymbol{r} - \boldsymbol{x}) \mapsto T_{\mathfrak{g}}\sqrt{S_\omega}\,\xi_j \otimes |\boldsymbol{x}\rangle, \quad \forall\, \boldsymbol{x} \in \mathcal{L}, \tag{7.2.28}$$

under the U map.

7.2.3 Canonical tight-binding form of the observables

Let A be an operator defined over $L^2(\mathbb{R}^3)$. Our goal here is to investigate how to define a canonical approximation as an operator A_ω over the effective Hilbert space $\mathbb{C}^N \otimes \ell^2(\mathcal{L}_\omega)$. The natural requirement is the matching of all the available matrix elements under the U_ω map (7.2.15), i.e.

$$\langle \phi_n(\cdot - \boldsymbol{x})|A|\phi_m(\cdot - \boldsymbol{x}')\rangle = \langle n, \boldsymbol{x}|\sqrt{S_\omega}\,A_\omega\sqrt{S_\omega}|m, \boldsymbol{x}'\rangle, \tag{7.2.29}$$

for all $n, m = \overline{1, N}$ and $\boldsymbol{x}, \boldsymbol{x}' \in \mathcal{L}_\omega$. For convenience, above and throughout, we use the notation $|n, \boldsymbol{x}\rangle$ for $\xi_n \otimes |\boldsymbol{x}\rangle$. Henceforth, let $\widehat{A}_{\boldsymbol{x},\boldsymbol{x}'}(\omega)$ be the matrix with the entries

$$A^{n,m}_{\boldsymbol{x},\boldsymbol{x}'}(\omega) = \int_{\mathbb{R}^3} \mathrm{d}^3\boldsymbol{r}\,\phi_n^*(\boldsymbol{r} - \boldsymbol{x})(A\phi_m)(\boldsymbol{r} - \boldsymbol{x}'), \tag{7.2.30}$$

which is just the explicit form of the coefficients appearing in the left side of (7.2.29). We form first the operator

$$\widetilde{A}_\omega = \sum_{\boldsymbol{x},\boldsymbol{x}' \in \mathcal{L}_\omega} \widehat{A}_{\boldsymbol{x},\boldsymbol{x}'}(\omega) \otimes |\boldsymbol{x}\rangle\langle \boldsymbol{x}'|, \tag{7.2.31}$$

over $\mathbb{C}^N \otimes \ell^2(\mathcal{L}_\omega)$. Then, the solution to (7.2.29) is supplied by

$$A_\omega = S_\omega^{-\frac{1}{2}}\,\widetilde{A}_\omega\,S_\omega^{-\frac{1}{2}}, \tag{7.2.32}$$

as it readily follows from a direct calculation. We call (7.2.32) the canonical tight-binding operator associated to the operator A that is defined in the continuum KS theory. Note that under this correspondence, the identity operator is sent to the identity operator.

Now assume that the continuum observable depends on ω in a covariant fashion.

In such a case, we can repeat the calculations leading to (7.2.19) to prove

$$\widehat{\mathfrak{D}}(\mathfrak{p})^\dagger \widehat{A}_{\mathfrak{g}\boldsymbol{x},\mathfrak{g}\boldsymbol{x}'}(\tau_\mathfrak{g}\omega)\widehat{\mathfrak{D}}(\mathfrak{p}) = \widehat{A}_{\boldsymbol{x},\boldsymbol{x}'}(\omega). \tag{7.2.33}$$

This automatically implies that $\widetilde{A}_\omega$ is a covariant operator under the space group transformations and, since A_ω in (7.2.32) is a product of covariant operators, A_ω is also a covariant operator:

$$T_\mathfrak{g} A_\omega T_\mathfrak{g}^\dagger = A_{\tau_\mathfrak{g}\omega}. \tag{7.2.34}$$

Below, we apply this standard procedure to several observables of interest.

As we learned in section 7.2.1, the continuum KS-Hamiltonian is a covariant observable. Furthermore, among the standard outputs of AIMD simulations are the matrix elements

$$W^{ij}_{\boldsymbol{x},\boldsymbol{x}'}(\omega) = \int_{\mathbb{R}^3} \mathrm{d}^3\boldsymbol{r}\ \phi_i^*(\boldsymbol{r}-\boldsymbol{x})(H^\omega_{\mathrm{KS}}\phi_j)(\boldsymbol{r}-\boldsymbol{x}'). \tag{7.2.35}$$

This is precisely the data one needs to define the tight-binding Hamiltonian. Following the above procedure, we define first the operator

$$\widetilde{H}_\omega = \sum_{\boldsymbol{x},\boldsymbol{x}'\in\mathcal{L}_\omega} \widehat{W}_{\boldsymbol{x},\boldsymbol{x}'}(\omega)\otimes|\boldsymbol{x}\rangle\langle\boldsymbol{x}'|, \tag{7.2.36}$$

which then supplies the tight-binding expression of the KS-Hamiltonian

$$H_\omega = S_\omega^{-\frac{1}{2}}\,\widetilde{H}_\omega\,S_\omega^{-\frac{1}{2}}, \quad T_\mathfrak{g} H_\omega T_\mathfrak{g}^\dagger = H_{\tau_\mathfrak{g}\omega}, \quad \mathfrak{g}\in\mathbb{G}. \tag{7.2.37}$$

We now focus on the position operator $\boldsymbol{X}$. At the continuum level of the theory, the matrix elements of the position operator are

$$\boldsymbol{R}^{ij}_{\boldsymbol{x},\boldsymbol{x}'}(\omega) = \int_{\mathbb{R}^3} \mathrm{d}^3\boldsymbol{r}\ \phi_i^*(\boldsymbol{r}-\boldsymbol{x})\,\boldsymbol{r}\,\phi_j(\boldsymbol{r}-\boldsymbol{x}'). \tag{7.2.38}$$

Note that these matrix elements depend too on the disordered configuration. They, however, satisfy a different covariant relation

$$\widehat{\mathfrak{D}}(\mathfrak{g})^\dagger \widehat{\boldsymbol{R}}_{\mathfrak{g}\boldsymbol{x},\mathfrak{g}\boldsymbol{x}'}(\tau_\mathfrak{g}\omega)\widehat{\mathfrak{D}}(\mathfrak{g}) = \mathfrak{p}\widehat{\boldsymbol{R}}_{\boldsymbol{x},\boldsymbol{x}'}(\omega) + \mathfrak{a}\,\widehat{S}_{\boldsymbol{x},\boldsymbol{x}'}(\omega), \tag{7.2.39}$$

for all $\mathfrak{g} = (\mathfrak{p}|\mathfrak{a}) \in \mathbb{G}$. The above relation follows from an exercise similar to that below (7.2.19). Before going any further, let us explain the notation. Note that $\widehat{\boldsymbol{R}}_{\boldsymbol{x},\boldsymbol{x}'}(\omega)$ is actually a 3-component column vector with matrices as entries. Then, $\mathfrak{p}$ in front of it, which is an ordinary 3×3 matrix, acts naturally on this 3-component vector. Furthermore, $\mathfrak{a}$ in the second term is viewed as an ordinary 3-component vector from $\mathbb{R}^3$ such that $\mathfrak{a}\,\widehat{S}_{\boldsymbol{x},\boldsymbol{x}'}(\omega)$ becomes a 3-component vector with matrix entries. Now, as before, we define an operator on $\mathbb{C}^N \otimes \ell^2(\mathcal{L}_\omega)$

$$\widetilde{\boldsymbol{R}}_\omega = \sum_{\boldsymbol{x},\boldsymbol{x}' \in \mathcal{L}} \widehat{\boldsymbol{R}}_{\boldsymbol{x},\boldsymbol{x}'}(\omega) \otimes |\boldsymbol{x}\rangle\langle\boldsymbol{x}'|, \tag{7.2.40}$$

which satisfies the covariance relation

$$T_{\mathfrak{g}} \widetilde{\boldsymbol{R}}_\omega T_{\mathfrak{g}}^\dagger = \mathfrak{p}^{-1} \widetilde{\boldsymbol{R}}_{\tau_{\mathfrak{g}}\omega} + (\mathfrak{p}^{-1}\mathfrak{a})\, S_{\tau_{\mathfrak{g}}\omega}, \tag{7.2.41}$$

as it follows directly from (7.2.39). Then

$$\boldsymbol{X}_\omega = S_\omega^{-\frac{1}{2}}\, \widetilde{\boldsymbol{R}}_\omega\, S_\omega^{-\frac{1}{2}} \tag{7.2.42}$$

maps the position operator from $L^2(\mathbb{R}^3)$ to $\mathbb{C}^N \otimes \ell^2(\mathcal{L}_\omega)$. Furthermore, the mapped position operator satisfies the covariance relation

$$T_{\mathfrak{g}} \boldsymbol{X}_\omega T_{\mathfrak{g}}^\dagger = \mathfrak{p}^{-1} \boldsymbol{X}_{\tau_{\mathfrak{g}}\omega} + (\mathfrak{p}^{-1}\mathfrak{a})\, I, \quad \mathfrak{g} = (\mathfrak{p}|\mathfrak{a}) \in \mathbb{G}, \tag{7.2.43}$$

where I is the identity operator. The above relation follows directly from (7.2.41).

Note that, although $\boldsymbol{X}_\omega$ is not entirely a covariant operator, the commutator $[\boldsymbol{X}_\omega, A_\omega]$ is covariant whenever A_ω is, i.e.

$$T_{\mathfrak{g}}[\boldsymbol{X}_\omega, A_\omega]T_{\mathfrak{g}}^\dagger = \mathfrak{p}^{-1}[\boldsymbol{X}_{\tau_{\mathfrak{g}}\omega}, A_{\tau_{\mathfrak{g}}\omega}], \quad \mathfrak{g} = (\mathfrak{p}|\mathfrak{a}) \in \mathbb{G}. \tag{7.2.44}$$

This will become relevant when we will analyze the charge current operator.

7.2.4 The trace per volume

Over the Hilbert space $L^2(\mathbb{R}^3)$, the trace per volume of a bounded operator A with continuous kernel $\langle \boldsymbol{r}|A|\boldsymbol{r}'\rangle$ is defined as

$$\mathrm{Tr}_V\{A\} = \lim_{V \to \mathbb{R}^3} \tfrac{1}{V} \int_V \mathrm{d}\boldsymbol{r}\ \langle \boldsymbol{r}|A|\boldsymbol{r}\rangle, \tag{7.2.45}$$

where, for consistency with the space group, we require that the limit be taken over finite volumes V that are invariant under the point group action. Our goal here is to supply its canonical translation over the effective Hilbert space $\mathbb{C}^N \otimes \ell^2(\mathcal{L}_\omega)$. For this, let A_ω be the tight-binding operator associated to A. We claim that

$$\mathrm{Tr}_V\{A_\omega\} = \frac{1}{V_0} \lim_{V\to\infty} \frac{1}{|\mathcal{L}_\omega \cap V|} \sum_{\boldsymbol{x}\in\mathcal{L}\cap V} \sum_{n=1}^{N} \langle n, \boldsymbol{x}|A_\omega|n, \boldsymbol{x}\rangle \tag{7.2.46}$$

supplies the canonical expression. Above, V_0 is the volume per Si atom, which is just half of that of the primitive cell, and $|\cdot|$ denotes the cardinal of a set.

Indeed, let us note that $\int_V \mathrm{d}\boldsymbol{r}\, \langle \boldsymbol{r}|A|\boldsymbol{r}\rangle$ coincides with the trace of A, when A is restricted over $L^2(V)$. This trace can be alternatively computed as $\sum_i \langle\psi_i|A|\psi_i\rangle$, with $\{\psi_i\}$ being an arbitrary orthonormal basis of $L^2(V)$. But, up to errors that are irrelevant in the thermodynamic limit and when N is large, the finite-volume trace can be computed using the partial basis $\{U_\omega^*|n, \boldsymbol{x}\rangle\}_{\boldsymbol{x}\in\mathcal{L}_\omega\cap V}^{n=\overline{1,N}}$. As a consequence, if N_a is the total number of atoms in V, then

$$\mathrm{Tr}_V\{A\} = \frac{1}{V_0} \lim_{N_a\to\infty} \frac{1}{N_a} \sum_{n=1}^{N} \sum_{\boldsymbol{x}\in\mathcal{L}\cap V} \langle n, \boldsymbol{x}|U_\omega A U_\omega^*|n, \boldsymbol{x}\rangle, \tag{7.2.47}$$

which coincides with (7.2.46).

The trace per volume, which is defined in (7.2.46), is a genuine trace over the algebra of operators we encounter in this work. For example, it displays the standard property $\mathrm{Tr}_V\{A_\omega B_\omega\} = \mathrm{Tr}_V\{B_\omega A_\omega\}$. An extremely important property of Tr_V is the self-averaging when evaluated on covariant operators, *i.e.* those operators satisfying the relations

$$T_{\mathfrak{g}} A_\omega T_{\mathfrak{g}}^\dagger = A_{\tau_{\mathfrak{g}}\omega}. \tag{7.2.48}$$

Indeed, using the invariance of the trace under conjugations, we have

$$\mathrm{Tr}_V\{A_\omega\} = \frac{1}{|H|} \sum_{\mathfrak{g}\in H\subset\mathbb{G}} \mathrm{Tr}_V\{T_{\mathfrak{g}} A_\omega T_{\mathfrak{g}}^\dagger\} = \frac{1}{|H|} \sum_{\mathfrak{g}\in H\subset\mathbb{G}} \mathrm{Tr}_V\{A_{\tau_{\mathfrak{g}}\omega}\}, \tag{7.2.49}$$

where H is a finite subset of $\mathbb{G}$ invariant to the point group. Since τ acts ergodically over Ω, in the limit $H \to \mathbb{G}$, Birkhoff's ergodic theorem assures us that the last term coincides with the ensemble average [123]. Hence,

$$\mathrm{Tr}_V\{A_\omega\} = \int_\Omega \mathrm{d}\mathbb{P}(\omega)\ \mathrm{Tr}_V\{A_\omega\}. \tag{7.2.50}$$

Let us point out that intensive thermodynamic variables as measured in laboratories, such as the transport coefficients, are all computed as traces per volumes of covariant observables. The aforementioned self-averaging property assures us that these macroscopic variables do not fluctuate from one disordered configuration to another, as long as the corresponding physical observables are covariant. This is the main reason why we pay special attention to the covariant properties of the physical observables in our theory.

7.3 Transport Coefficients

With the mappings from the previous section, we can formulate the theory of quantum charge transport directly on the Hilbert space $\mathbb{C}^N \otimes \ell^2(\mathcal{L}_\omega)$. The goal of this section is to supply the key elements of this theory and to formulate the Kubo-formula for the conductivity tensor.

7.3.1 Kinetic theory of quantum transport

The purpose of this section is to review the theory of charge transport in the presence of dissipation, as developed by Schulz-Baldes and Bellissard [101–103].

Let us recall that the physical observable corresponding to the 3-component vector of the electron charge current density is

$$\boldsymbol{J}_\omega = -\frac{e}{\imath\hbar}[\boldsymbol{X}_\omega, H_\omega], \tag{7.3.1}$$

where $e = 1.6 \times 10^{-19}$ C is the charge of the electron. Based on the last remark in Section 7.2.3, $\boldsymbol{J}_\omega$ is a covariant operator, i.e.

$$T_\mathfrak{g} \boldsymbol{J}_\omega T_\mathfrak{g} = \mathfrak{p}^{-1} \boldsymbol{J}_{\tau_\mathfrak{g}\omega}. \tag{7.3.2}$$

Under the action of an externally applied electric field $\boldsymbol{E}$, the measured current-density is

$$\boldsymbol{j}_{\boldsymbol{E}} = \lim_{T\to\infty} \frac{1}{T} \int_0^T \mathrm{d}t \ \mathrm{Tr}_V \big\{ \boldsymbol{J}_\omega \rho_\omega(t) \big\}, \tag{7.3.3}$$

where $\rho_\omega(t)$ is the time-evolved density matrix. The time evolution is w.r.t. the time-dependent Hamiltonian

$$H(t) = H_\omega + e\boldsymbol{E}\cdot\boldsymbol{X}_\omega + V_\omega(t), \tag{7.3.4}$$

which incorporates the externally applied electric field $\boldsymbol{E}$, as well as dissipation via the scattering potential

$$V_\omega(t) = \sum_{j\in\mathbb{Z}} \delta(t-t_j) W_\omega, \tag{7.3.5}$$

with W_ω assumed to be covariant. The collision times $\eta = \{t_j\}_{j\in\mathbb{Z}}$ are generated via a Poisson process with fixed collision time-scale τ_c. Such processes are known to be self-averaging, hence the time and the space averages in (7.3.3) do not depend on the particular realization of the collision times, nor on the disordered configuration. In other words, $\boldsymbol{j}_{\boldsymbol{E}}$ defined in (7.3.3) is a genuine macroscopic thermodynamic coefficient.

For the reason state above, one can use in (7.3.3) an effective quantum time evolution, which is averaged over the Poisson processes η. A computation of this average can be found in [105]. It takes the form

$$U_{\mathrm{eff}}(t) A U_{\mathrm{eff}}(t)^* = e^{-\frac{t}{\hbar}(\Gamma_\omega + \mathrm{L}_{\boldsymbol{E},\omega})}[A], \tag{7.3.6}$$

where Γ is the collision super-operator, acting on the physical observables as

$$\Gamma_\omega[A] = \tfrac{\hbar}{\tau_c}\big(A - e^{\frac{\imath}{\hbar}W_\omega} A \, e^{-\frac{\imath}{\hbar}W_\omega}\big), \tag{7.3.7}$$

and $\mathrm{L}_{\boldsymbol{E},\omega}$ is the super-operator

$$\mathrm{L}_{\boldsymbol{E},\omega}[A] = \imath[H_\omega, A] - e\boldsymbol{E}\cdot\imath[\boldsymbol{X}_\omega, A]. \tag{7.3.8}$$

The electrons are assumed initially at the thermal equilibrium, hence the initial density matrix takes the form

$$\rho_\omega(t=0) = \Phi_{\mathrm{FD}}(H_\omega; T, \mu), \tag{7.3.9}$$

where $\Phi_{\mathrm{FD}}(\epsilon; T, \mu)$ is the Fermi-Dirac distribution at temperature T and μ the chemical potential. The density matrix is evolved via the time propagator (7.3.6), hence

$$\rho_\omega(t) = U(t)\,\Phi_{\mathrm{FD}}(H_\omega; T, \mu)\,U(t)^*. \tag{7.3.10}$$

Since, the two parameters T and μ are kept fixed, we will omit writing them explicitly.

7.3.2 Kubo formula with dissipation

With the inputs supplied in the previous section, (7.3.3) can be evaluated explicitly:

$$\boldsymbol{J}^{\omega}_{\boldsymbol{E}} = \frac{e^2}{\hbar}\mathrm{Tr}_V\left\{\big[\boldsymbol{X}_\omega, H_\omega\big]\big(\Gamma_\omega + \mathrm{L}_{\boldsymbol{E},\omega}\big)^{-1}\big[\boldsymbol{E}\cdot\boldsymbol{X}_\omega, \Phi_{\mathrm{FD}}(H_\omega)\big]\right\}. \tag{7.3.11}$$

In the linear regime, this leads to a Kubo-formula with dissipation for the conductivity tensor

$$\sigma^{\alpha\beta}(T,\mu;\omega) = -\pi G_0 \mathrm{Tr}_V\Big\{\big[X^\alpha_\omega, H_\omega\big](\Gamma_\omega + \mathrm{L}_\omega)^{-1}\big[X^\beta_\omega, \Phi_{\mathrm{FD}}(H_\omega)\big]\Big\}, \tag{7.3.12}$$

where α and β indicate space directions, L_ω is the limit of $L_{\boldsymbol{E},\omega}$ as $\boldsymbol{E} \to 0$ and $G_0 = \frac{2e^2}{h} = 7.74 \times 10^{-5}$ S is the conductance quantum. Note that the super-operator $(\Gamma_\omega + \mathrm{L}_\omega)^{-1}$ acts on the observable appearing at its right.

7.3.3 Self-averaging of the transport coefficients

We now discuss the self-averaging properties of the conductivity tensor. Using the covariant properties of the operators appearing in the Kubo formula, one finds

$$\begin{aligned}\sigma^{\alpha\beta}(T,\mu;\tau_{\mathfrak{g}}\omega) = &-\pi G_0\,\mathfrak{p}_{\alpha\alpha'}\mathrm{Tr}_V\Big\{T_{\mathfrak{g}}\big[X^{\alpha'}_\omega, H_\omega\big] \\ &(\Gamma_\omega + \mathrm{L}_\omega)^{-1}\big[X^{\beta'}_\omega, \Phi(H_\omega)\big]T^\dagger_{\mathfrak{g}}\Big\}\mathfrak{p}_{\beta'\beta},\end{aligned} \tag{7.3.13}$$

for any $\mathfrak{g} = (\mathfrak{p}|\mathfrak{a}) \in \mathbb{G}$, where repeated indices are summed over their range. Using the invariance of the trace under conjugation, we find the simple rule of transformation

$$\hat{\sigma}(T, \mu; \tau_{\mathfrak{g}}\omega) = \mathfrak{p}\, \hat{\sigma}(T, \mu; \omega)\, \mathfrak{p}^{-1}. \tag{7.3.14}$$

As such, the conductivity tensor is invariant under the translations $(1|\mathfrak{t}) \in \mathcal{B}$. Our observation in section 7.1.2 that this subgroup of $\mathbb{G}$ acts ergodically on Ω, become extremely important because it assures us that $\hat{\sigma}(T, \mu)$ is self-averaging and does not fluctuate from one disordered configuration to another. Indeed, given that $\hat{\sigma}(T, \mu; \omega) = \sigma(T, \mu; \tau_{(1|\mathfrak{t})}\omega)$ for any $(1|\mathfrak{t}) \in \mathcal{B}$), we can write

$$\begin{aligned} \hat{\sigma}(T, \mu; \omega) &= \lim_{V \to \mathbb{R}^3} \frac{1}{|V \cap \mathcal{B}|} \sum_{\mathfrak{t} \in V} \hat{\sigma}(T, \mu; \tau_{(1|\mathfrak{t})}\omega) \\ &= \int_{\Omega} \mathrm{d}\mathbb{P}(\omega')\, \hat{\sigma}(T, \mu; \omega'), \end{aligned} \tag{7.3.15}$$

where the last equality follows from Birkhoff's theorem [123]. Now, the only way to reconcile the above conclusion and (7.3.14), is to admit the invariance of the conductivity tensor under the point group action

$$\mathfrak{p}^{-1}\, \hat{\sigma}(T, \mu; \omega)\, \mathfrak{p} = \hat{\sigma}(T, \mu; \omega), \quad \forall\, \mathfrak{p} \in \mathcal{P}. \tag{7.3.16}$$

The remarkable conclusion is that the invariance w.r.t. the full space group $\mathbb{G}$ of the non-averaged conductivity tensor is exact even though this symmetry is broken locally by the thermal motion of atoms. We mention that in our numerical calculations, we evaluate the isotropic part of the conductivity tensor

$$\sigma(T, \mu; \omega) = \tfrac{1}{3} \sum_{\alpha=1}^{3} \sigma^{\alpha\alpha}(T, \mu; \omega), \tag{7.3.17}$$

which is manifestly invariant under the action of the entire space group.

Let us stress that the above self-averaging property manifests itself only in the strict thermodynamic limit. For finite samples, there will be fluctuations w.r.t. the thermally disordered configurations. This is because the group of symmetry transformations gets reduced when dealing with finite samples and, as a consequence, $\tau_{\mathfrak{g}}\omega$ does not explore[2] the whole Ω when $\mathfrak{g}$ is given all allowed values. For

---

[2] Up to subsets of measure zero

a finite Si crystal of cubic shape, which is built by repeating the unit cell, the rank of the group of symmetries is equal to the number N_a of atoms in the crystal. Given the invariance of $\sigma(\mu, T; \omega)$ w.r.t. these transformations, when we evaluate $\sigma(\mu, T; \omega)$ for one disordered configuration, we in fact evaluate the conductivity for all $\tau_{\mathfrak{g}}\omega$ configurations. In other words, with just one calculation, we sample N_a points of Ω. Hence, if we repeat the calculation of $\sigma(\mu, T; \omega)$ for a number N_c of different configurations, we effectively sampled Ω at $N_a \times N_c$ points. Because of this amplification effect that stems from the invariance of $\sigma(\mu, T; \omega)$ relative to the space symmetries, we expect that a good disorder average can be achieved even with a small number of disordered configurations. This is indeed observed in our simulations.

7.3.4 Optimal finite-volume approximations

There are two fundamental difficulties when attempting to evaluate (7.3.12) on a computer. The first one stems from the incompatibility between the covariant relation (7.2.43) for the position operator and the periodic boundary conditions. The second difficulty comes from inverting the super-operator $\Gamma_\omega + \mathrm{L}_\omega$. Both these issues have been resolved in [105] and then further refined in [110, 124]. In the present context, however, the situation is slightly different because the position operator depends on the disordered configuration. This complication is being addressed below.

We start by computing the matrix elements of the commutator of a continuum observable with the position operator:

$$\begin{aligned}
[\boldsymbol{X}, A]^{m,n}_{\boldsymbol{x},\boldsymbol{x}'}(\omega) =& \int_{\mathbb{R}^3} \mathrm{d}^3\boldsymbol{r}\, \phi^*_m(\boldsymbol{r}-\boldsymbol{x})([\boldsymbol{X}, A]\phi_n)(\boldsymbol{r}-\boldsymbol{x}') \qquad (7.3.18)\\
=& \int_{\mathbb{R}^3} \mathrm{d}^3\boldsymbol{r} \int_{\mathbb{R}^3} \mathrm{d}^3\boldsymbol{r}'\, (\boldsymbol{r}-\boldsymbol{r}')\phi^*_m(\boldsymbol{r}-\boldsymbol{x})A(\boldsymbol{r},\boldsymbol{r}')\phi_n(\boldsymbol{r}'-\boldsymbol{x}')\\
=& (\boldsymbol{x}-\boldsymbol{x}') \int_{\mathbb{R}^3} \mathrm{d}^3\boldsymbol{r} \int_{\mathbb{R}^3} \mathrm{d}^3\boldsymbol{r}'\, \phi^*_m(\boldsymbol{r}-\boldsymbol{x})A(\boldsymbol{r},\boldsymbol{r}')\phi_n(\boldsymbol{r}'-\boldsymbol{x}')\\
&+ \int_{\mathbb{R}^3} \mathrm{d}^3\boldsymbol{r} \int_{\mathbb{R}^3} \mathrm{d}^3\boldsymbol{r}'\, (\boldsymbol{r}-\boldsymbol{r}')\phi^*_m(\boldsymbol{r})A(\boldsymbol{r},\boldsymbol{r}')\phi_n(\boldsymbol{r}').
\end{aligned}$$

We can summarize the above calculation as

$$[\boldsymbol{X}, A]^{m,n}_{\boldsymbol{x},\boldsymbol{x}'}(\omega) = (\boldsymbol{x} - \boldsymbol{x}')A^{m,n}_{\boldsymbol{x},\boldsymbol{x}'}(\omega) + [\boldsymbol{X}, A]^{m,n}_{\boldsymbol{0},\boldsymbol{0}}(\omega). \tag{7.3.19}$$

While the right hand side makes perfect sense for an infinite samples, when the simulation proceeds over a finite crystal with periodic boundary conditions, there is an obvious problem with the first term. In [110, 124], it was found that the optimal adaptation to the periodic boundary conditions is through the following substitution:

$$\boldsymbol{x} - \boldsymbol{x}' \to \boldsymbol{x} - \boldsymbol{x}' - \left[\left[\frac{\boldsymbol{x} - \boldsymbol{x}'}{L/2}\right]\right] L, \tag{7.3.20}$$

where L is the size of the periodic super-cell of the simulation and $[[\cdot]]$ denotes the integer part of a real number. The second term in (7.3.19) is a local term and there is no need for a modification when finite crystals with periodic boundary conditions are considered. With the proper matrix elements at hand, the finite-volume tight-binding operators corresponding to the commutators with the position operator are derived via the procedure detailed in section 7.2.3 without any modifications. To alert the reader about the substitution (7.3.20), we write the modified commutators of these tight-binding operators as $\lfloor X_\omega, A_\omega \rfloor$.

We now focus on the super-operator $\Gamma_\omega + \mathrm{L}_\omega$. We will only consider here the so called relaxation time approximation where the dissipation super-operator is proportional with identity: $\Gamma_\omega = \Gamma_0\,\mathrm{id}$, with Γ_0 a positive number. Now we recall that L_ω acts on operators A_ω over $\mathbb{C}^N \otimes \ell^2(\mathcal{L}_\omega)$ via $\mathrm{L}_\omega[A_\omega] = \imath[H_\omega, A_\omega]$. Observe that, if

$$\big(\epsilon^\omega_a,\ \psi^\omega_a\big)_{a=1,\ldots,N|\mathcal{L}_\omega|} \tag{7.3.21}$$

is an eigen-system for H_ω, then

$$\mathrm{L}_\omega\big[|\psi^\omega_a\rangle\langle\psi^\omega_b|\big] = \imath(\epsilon^\omega_a - \epsilon^\omega_b)\,|\psi^\omega_a\rangle\langle\psi^\omega_b|. \tag{7.3.22}$$

In other words,

$$\Big(\epsilon^\omega_a - \epsilon^\omega_b,\ |\psi^\omega_a\rangle\langle\psi^\omega_b|\Big)_{a,b=1,\ldots,N|\mathcal{L}_\omega|} \tag{7.3.23}$$

is an eigen-system for L_ω. This observation together with the fact that any operator can be decomposed as

$$A_\omega = \sum_{a,b} \langle \psi_a^\omega | A_\omega | \psi_b^\omega \rangle \, |\psi_a^\omega\rangle\langle\psi_b^\omega| \tag{7.3.24}$$

provide a straightforward way to invert the super-operator:

$$(\Gamma_0 \,\mathrm{id} + \mathrm{L}_\omega)^{-1}[A_\omega] = \sum_{a,b} \frac{\langle \psi_a^\omega | A_\omega | \psi_b^\omega \rangle}{\Gamma_0 + \imath(\epsilon_a^\omega - \epsilon_b^\omega)} |\psi_a^\omega\rangle\langle\psi_b^\omega|. \tag{7.3.25}$$

Finally, we can give a direct translation of the Kubo-formula (7.3.12) at finite-volume:

$$\sigma^{\alpha\beta} = \Big\langle \tfrac{-\pi G_0}{\mathrm{Vol}} \sum_{a,b} \frac{\big\langle \psi_a^\omega \big| \lfloor X_\omega^\alpha, H_\omega \rfloor \big| \psi_b^\omega \big\rangle \big\langle \psi_b^\omega \big| \lfloor X_\omega^\beta, \Phi_{\mathrm{FD}}(H_\omega) \rfloor \big| \psi_a^\omega \big\rangle}{\Gamma_0 + \imath(\epsilon_a^\omega - \epsilon_b^\omega)} \Big\rangle_\omega . \tag{7.3.26}$$

This expression is useful when the matrix elements of the Fermi operator are available. Since this quantity is not among the standard outputs of AIMD simulations, we process this expression one step further as in [109]:

$$\begin{aligned} \sigma^{\alpha\beta} = \Big\langle \tfrac{-\pi G_0}{\mathrm{Vol}} \sum_{a,b} & \frac{\Phi_{\mathrm{FD}}(\epsilon_a^\omega) - \Phi_{\mathrm{FD}}(\epsilon_b^\omega)}{\epsilon_a^\omega - \epsilon_b^\omega} \\ & \times \frac{\big\langle \psi_a^\omega \big| \lfloor X_\omega^\alpha, H_\omega \rfloor \big| \psi_b^\omega \big\rangle \big\langle \psi_b^\omega \big| \lfloor X_\omega^\beta, H_\omega \rfloor \big| \psi_a^\omega \big\rangle}{\Gamma_0 + \imath(\epsilon_a^\omega - \epsilon_b^\omega)} \Big\rangle_\omega . \end{aligned} \tag{7.3.27}$$

This is the expression we coded as a post-processing subroutine to the AIMD simulations. The inputs for this expression are the matrix elements of the Kohn-Sham Hamiltonians (7.2.35) and the overlap coefficients (7.2.13), as well as the xyz-coordinates of the atoms.

7.4 Numerical Implementation

In this section, we first present a novel electronic structure method that is only scaling quadratically with system size, thus facilitating second-generation Car-Parrinello AIMD simulations of even longer length and time scales than previously thought feasible [98, 99]. More importantly, this approach permits to efficiently compute the exact finite-temperature density matrix ρ_ω of a given Kohn-Sham

Hamiltonian H_ω "on-the-fly" during the AIMD. Thereafter, the computational details of our simulations are described in detail.

7.4.1 Field-Theory-based Eigenvalue Solver

Following Alavi and coworkers [125, 126], we begin with the (Helmholtz) free energy functional

$$\mathcal{F} = \Xi + \mu N_e + V_{dc}, \tag{7.4.1}$$

where $N_e = 2\mathcal{N}$ is the number of electrons and Ξ the grand-canonical potential (GCP) for noninteracting fermions. The latter reads as

$$\Xi = -\tfrac{2}{\beta} \ln \det \left(1 + e^{\beta(\mu S_\omega - H_\omega)}\right) = -\tfrac{2}{\beta} \operatorname{Tr} \ln \left(1 + e^{\beta(\mu S_\omega - H_\omega)}\right), \tag{7.4.2}$$

with given by $\beta^{-1} = kT$ (k = Boltzmann constant). Yet, in the low-temperature limit

$$\lim_{\beta\to\infty} \Xi = 2 \sum_{a=1}^{\mathcal{N}} \epsilon_a^\omega - \mu N_e, \tag{7.4.3}$$

the so-called band-structure energy, which is given by the sum of the lowest $\mathcal{N}$ doubly occupied eigenvalues ϵ_a^ω of H_ω, can be recovered and

$$\lim_{\beta\to\infty} \mathcal{F} = 2 \sum_{a=1}^{\mathcal{N}} \epsilon_a^\omega + V_{dc} \tag{7.4.4}$$

holds. Therein, V_{dc} accounts for double counting terms, as well as for the nuclear Coulomb interaction.

In the present case of fully self-consistent KS-DFT calculations

$$\begin{aligned} V_{dc}[n_\omega(\boldsymbol{r})] &= -\tfrac{1}{2} \int d\boldsymbol{r} \int d\boldsymbol{r}' \, \frac{n_\omega(\boldsymbol{r}) n_\omega(\boldsymbol{r}')}{|\boldsymbol{r} - \boldsymbol{r}'|} \\ &- \int d\boldsymbol{r} \, n_\omega(\boldsymbol{r}) \, \frac{\delta \Xi_{\mathrm{XC}}[n_\omega(\boldsymbol{r})]}{\delta n_\omega(\boldsymbol{r})} + \Xi_{\mathrm{XC}}[n_\omega(\boldsymbol{r})] + E_{II}, \end{aligned} \tag{7.4.5}$$

where the first term on the right hand side is the double counting correction of the Hartree energy, while $\Xi_{\mathrm{XC}}[n_\omega(\boldsymbol{r})]$ is the finite-temperature XC grand-canonical functional and E_{II} the nuclear Coulomb interaction. Except for the latter term, Eq. (7.4.5) accounts for the difference between Ξ and the GCP for the interacting spin-$\frac{1}{2}$ Fermi gas, i.e.

$$\begin{aligned}\Xi_{int}[n_\omega(\boldsymbol{r})] &= -\tfrac{2}{\beta}\ln\det\left(1+e^{\beta\left(\mu S_\omega - H_{\mathrm{KS}}^\omega\right)}\right)\\ &- \tfrac{1}{2}\int d\boldsymbol{r}\int d\boldsymbol{r}'\,\frac{n_\omega(\boldsymbol{r})n_\omega(\boldsymbol{r}')}{|\boldsymbol{r}-\boldsymbol{r}'|}\\ &- \int d\boldsymbol{r}\,n_\omega(\boldsymbol{r})\,\frac{\delta\Xi_{\mathrm{XC}}[n_\omega(\boldsymbol{r})]}{\delta n_\omega(\boldsymbol{r})}+\Xi_{\mathrm{XC}}[n_\omega(\boldsymbol{r})]. \qquad (7.4.6)\end{aligned}$$

As before, in the low-temperature limit $\Xi_{int}[n_\omega(\boldsymbol{r})]+\mu N_e$ equals to the band-structure energy, whereas $\Xi_{\mathrm{XC}}[n_\omega(\boldsymbol{r})]$ corresponds to the familiar XC energy, so that in this limit $\mathcal{F}=\Xi+\mu N_e+V_{dc}=\Xi_{int}[n_\omega(\boldsymbol{r})]+\mu N_e+E_{II}$ is equivalent to the Harris-Foulkes functional [127, 128]. Equally than the latter, $\mathcal{F}$ is explicitly defined for any $n_\omega(\boldsymbol{r})$ and obeys exactly the same stationary point as the finite-temperature functional of Mermin [129].

Whereas it is well known how to calculate V_{dc} with linear-scaling computational effort, the computation of all occupied orbitals by diagonalization requires $\mathcal{O}(N^3)$ operations. Due to the fact that the band-structure term can be equivalently expressed in terms of ρ_ω, the total energy can be written as

$$E_{\mathrm{KS}}[n_\omega(\boldsymbol{r})]=2\sum_{a=1}^{\mathcal{N}}\epsilon_i^\omega+V_{dc}=\mathrm{Tr}[\rho_\omega H_{\mathrm{KS}}^\omega]+V_{dc}[n_\omega(\boldsymbol{r})]. \qquad (7.4.7)$$

As a consequence, the cubic-scaling diagonalization of H_{KS}^ω can be bypassed by directly calculating ρ_ω rather than all ε_i's.

In order to make further progress, let us now factorize the operator of Eq. (7.4.2) into P terms. Given that P is even, which we shall assume in the following, Krajewski and Parrinello derived the following identity

$$1+e^{\beta\left(\mu S_\omega-H_{\mathrm{KS}}^\omega\right)}=\prod_{l=1}^{P}\left(1-e^{\frac{i\pi}{2P}(2l-1)}e^{\frac{\beta}{2P}\left(\mu S_\omega-H_{\mathrm{KS}}^\omega\right)}\right)=\prod_{l=1}^{P/2}M_l^*M_l, \qquad (7.4.8)$$

where the matrices M_l, with $l=1,\ldots,P$, are defined as

$$M_l:=1-e^{\frac{i\pi}{2P}(2l-1)}e^{\frac{\beta}{2P}\left(\mu S_\omega-H_{\mathrm{KS}}^\omega\right)}, \qquad (7.4.9)$$

while * denotes complex conjugation [130]. Analog to numerical path-integral calculations [131], it is possible to exploit the fact that if P is large enough, so that the effective temperature β/P is small, the exponential operator $e^{\frac{\beta}{2P}\left(\mu S_\omega - H^\omega_{\text{KS}}\right)}$ can be approximated by a Trotter decomposition or simply by a high-temperature expansion, i.e.

$$M_l = 1 - e^{\frac{i\pi}{2P}(2l-1)}\left(1 + \tfrac{\beta}{2P}(\mu S_\omega - H^\omega_{\text{KS}})\right) + \mathcal{O}\left(\frac{1}{P^2}\right). \tag{7.4.10}$$

However, as we will see, here no such approximation is required, which is in contrast to the original approach [130]. In any case, the GCP can be rewritten as

$$\Xi \;=\; -\tfrac{2}{\beta}\ln\prod_{l=1}^{P/2}\det\left(M_l^* M_l\right) = \tfrac{4}{\beta}\sum_{l=1}^{P/2}\ln\left(\det\left(M_l^* M_l\right)\right)^{-\frac{1}{2}}. \tag{7.4.11}$$

As is customary in lattice gauge theory [132, p. 17], where the minus sign problem is avoided by sampling a positive definite distribution, the inverse square root of the determinant can be expressed as an integral over a complex field $\boldsymbol{\phi}_l$, which has the same dimension M as the full Hilbert space, i.e.

$$\det\left(M_l^* M_l\right)^{-1/2} = \frac{1}{(2\pi)^{\frac{M}{2}}}\int d\phi_l\, e^{-\frac{1}{2}\phi_l^* M_l^* M_l \phi_l}. \tag{7.4.12}$$

Inserting Eq. (7.4.12) into Eq. (7.4.11) we end up with the following field-theoretic expression for the GCP:

$$\begin{aligned}\Xi \;&=\; \tfrac{4}{\beta}\sum_{l=1}^{P/2}\ln\left[\frac{1}{(2\pi)^{\frac{M}{2}}}\int d\phi_l\, e^{-\frac{1}{2}\phi_l^* M_l^* M_l \phi_l}\right] \\ &=\; \tfrac{4}{\beta}\sum_{l=1}^{P/2}\ln\int d\phi_l\, e^{-\frac{1}{2}\phi_l^* M_l^* M_l \phi_l} + const.,\end{aligned} \tag{7.4.13}$$

where ϕ_l are appropriate vectors.

All physical relevant observables can then be determined as functional derivatives of the GCP w.r.t. an appropriately chosen external parameter. For example, $N_e = -\partial\Xi/\partial\mu$ and $\lim_{\beta\to\infty}\Xi + \mu N_e = 2\sum_{a=1}^{\mathcal{N}}\epsilon_i^\omega$, so that

$$E = \lim_{\beta\to\infty}\mathcal{F} = 2\sum_{a=1}^{\mathcal{N}}\epsilon_a^\omega + V_{dc} = \frac{\partial(\beta\Xi)}{\partial\beta} - \mu\frac{\partial\Xi}{\partial\mu} + V_{dc}. \tag{7.4.14}$$

Since the functional derivative of the constant in Eq. (7.4.13) is identical to zero, all physical interesting quantities can be computed via

$$\begin{aligned}
\frac{\partial \Xi}{\partial \lambda} &= -\tfrac{2}{\beta} \sum_{l=1}^{P/2} \frac{\int d\phi_l \sum\limits_{i,j=1}^{d} (\phi_l)_i^* \left(\frac{\partial (M_l^* M_l)}{\partial \lambda}\right)_{ij} (\phi_l)_j \, e^{-\frac{1}{2}\phi_l^* M_l^* M_l \phi_l}}{\int d\phi_l \, e^{-\frac{1}{2}\phi_l^* M_l^* M_l \phi_l}} \quad &(7.4.15a)\\
&= -\tfrac{2}{\beta} \sum_{l=1}^{P/2} \sum_{i,j=1}^{d} \left(\frac{\partial (M_l^* M_l)}{\partial \lambda}\right)_{ij} (M_l^* M_l)^{-1}_{ij} \quad &(7.4.15b)\\
&= -\tfrac{2}{\beta} \sum_{l=1}^{P/2} \mathrm{Tr}\left[(M_l^* M_l)^{-1} \frac{\partial (M_l^* M_l)}{\partial \lambda}\right] = -\tfrac{2}{\beta} \sum_{l=1}^{P} \mathrm{Tr}\left[M_l^{-1} \frac{\partial M_l}{\partial \lambda}\right] . \quad &(7.4.15c)
\end{aligned}$$

Thereby, the left-hand side of Eq. (7.4.15c) holds because of Montvay and Münster [132, p. 18], whereas the right-hand side is due to the fact that beside being positive definite $M_l^* M_l$ is also symmetric.

Comparing Eq. (7.4.7) with Eq. (7.4.3), it is easy to see that the GCP and hence all physical significant observables can be written as the trace of a product consisting of the Fermi matrix ρ_ω. Specifically, $\Xi = \mathrm{Tr}[\rho_\omega H^\omega_{\mathrm{KS}}] - \mu N_e$, but because at the same time $N_e = \mathrm{Tr}[\rho_\omega S_\omega]$ holds, the former can be simplified to

$$\Xi = \mathrm{Tr}[\rho_\omega (H^\omega_{\mathrm{KS}} - \mu S_\omega)], \tag{7.4.16}$$

where $S_\omega = -\partial H^\omega_{\mathrm{KS}} / \partial \mu$ and $\rho_\omega = \partial \Xi / \partial H^\omega_{\mathrm{KS}}$. As a consequence, the GCP and all its functional derivatives can be reduced to evaluate ρ_ω based on Eq. (7.4.15c) with $\lambda = H_{ij}$. Using the identity

$$\frac{\partial M_l}{\partial H_{ij}} = -\tfrac{1}{2P} \left\{ (M_l - 1)\beta + \beta (M_l - 1) \right\} , \tag{7.4.17}$$

for this particular case, Eq. (7.4.15c) eventually equals to

$$\rho_\omega = \frac{\partial \Xi}{\partial H^\omega_{\mathrm{KS}}} = \tfrac{4}{P} \sum_{l=1}^{P/2} \left(1 - \left(M_l^* M_l\right)^{-1}\right) = \tfrac{2}{P} \sum_{l=1}^{P} \left(1 - M_l^{-1}\right) . \tag{7.4.18}$$

In other words, the origin of the method is the notion that the density matrix, the square of the wavefunction at low temperature and the Maxwell-Boltzmann distribution at high temperature, can be decomposed into a sum of M_l^{-1} matrices, each at higher effective temperature β/P and hence always sparser than ρ_ω. Yet, contrary to the original approach [130], neither a Trotter decomposition nor a high-temperature expansion for Eq. (7.4.9) has been used, so far everything is exact for any P.

In particular, unlike Eq. (7.4.11), the determination of $\Omega = \partial(\beta\Omega)/\partial\beta$ does no longer involve the calculation of the inverse square root of a determinant, but just the inverse of M_l, which is not only very sparse, since it obeys the same sparsity pattern as H_{KS}^{ω}, but is furthermore also always better conditioned as the latter. Hence, all M_l^{-1} matrices are substantially sparser than ρ_ω and thus can be efficiently computed [133, 134]. In fact, for quasi one-dimensional systems, M_l is tridiagonal that permits for an exact linear-scaling calculation of its inverse using a recursive scheme [135]. For all other dimensions D, M_l can be sought of being block-tridiagonal, where the dimensionality of each block is $d = N^{1-(1/D)}$, eventually leading to a computational effort, which scales like $Nd^2 = N^{3-2/d}$. Since this is only marginally better than the initial $\mathcal{O}(N^3)$ scaling for a general matrix inversion (or diagonalization), we compute M_l^{-1} by solving the N_e sets of linear equations $M_l \Phi_j^l = \psi_j$, where $\{\psi_j\}$ is a complete set of basis functions [136]. Using a preconditioned biconjugate gradient method [137], the inverse can be exactly computed as $M_l^{-1} = \sum_{j=1}^{N_e} \phi_j^l \psi_j^l$ within $\mathcal{O}(N^2)$ operations. Furthermore, the formal analogy of the decomposition to the Trotter factorization immediately suggests the possibility to apply some of the here presented ideas with benefit to numerical path-integral calculations [131]. The same applies for a related area where these methods are extensively used, namely the lattice gauge theory to quantum chromodynamics [138], whose action is rather similar to the one of Eq. (7.4.12).

7.4.2 Computational Details

We now return to our specific simulations. Our models of crystalline silicon consisted of 216 and 1000 Si atoms in a cubic simulation box with periodic boundary conditions. For each system size, five simulations have been conducted, at $T = 300$ K, 600 K, 900 K, 1200 K and 1500 K, respectively. All of our calculations were performed in the canonical NVT ensemble using the second-generation Car-Parrinello AIMD method of Kühne and coworkers [98, 99]. Throughout, the experimental density of crystalline silicon was assumed, which, at ambient conditions, is semiconducting and four-fold coordinated. In each run, we carefully

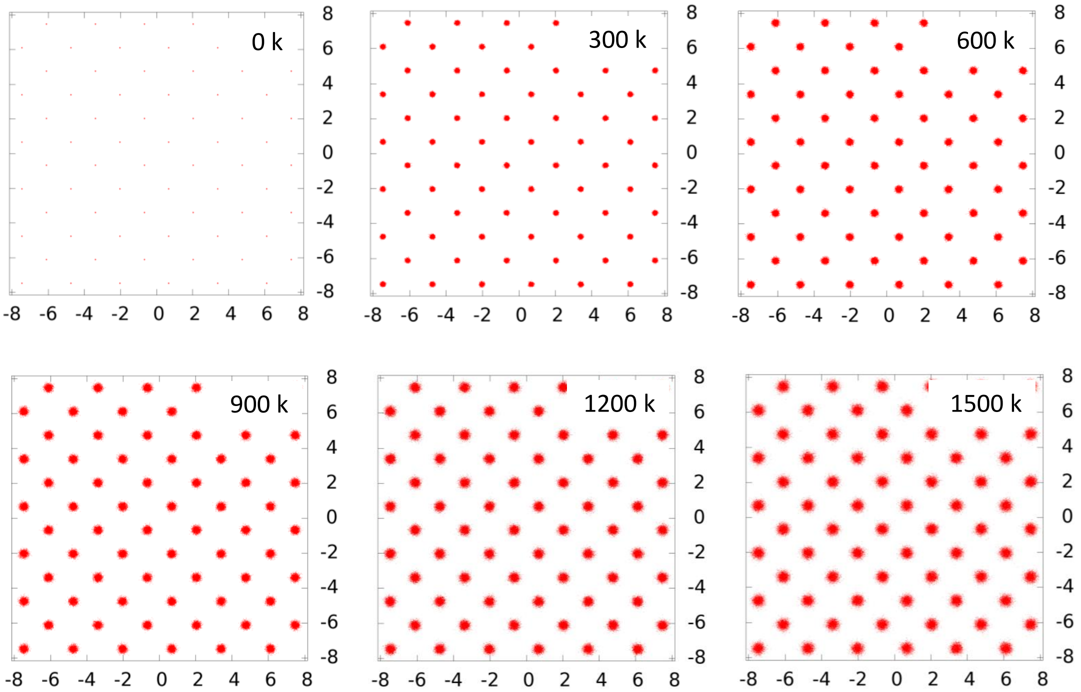

Figure 7.2: The orbits of the atoms under the thermal motion at different temperatures. The simulation is for a crystal containing 216 Si atoms and each orbit is sampled at 1001 points. In these renderings, the crystal is viewed from atop of xy-plane. The units of the graphs are Angstroms.

equilibrated the system for 250 ps before accumulating statistics during additional 1.25 ns, resulting in a total AIMD simulation time of 15 ns.

All simulations were performed at the DFT level using the mixed Gaussian and plane wave code CP2K/*Quickstep* [100]. In this approach, the KS orbitals are expanded in contracted Gaussians functions, while the electronic charge density is represented by plane waves [78]. A density cutoff of 100 Ry was employed for the latter, whereas for the former a dimer-optimized minimal basis set was used [139] of s- and p-type. As such, $N = 4$ in (7.2.9) and the linear space spanned by these wave functions is indeed a representation space for the $O(3)$ group. The unknown exact XC potential is substituted by the LDA [122], whereas the interactions between the valence electrons and the ionic cores are described by separable norm-conserving Goedecker-Teter-Hutter pseudopotentials [140, 141]. For the sake of simplicity, the first Brillouin zone of the super cell is sampled at the Γ-point only.

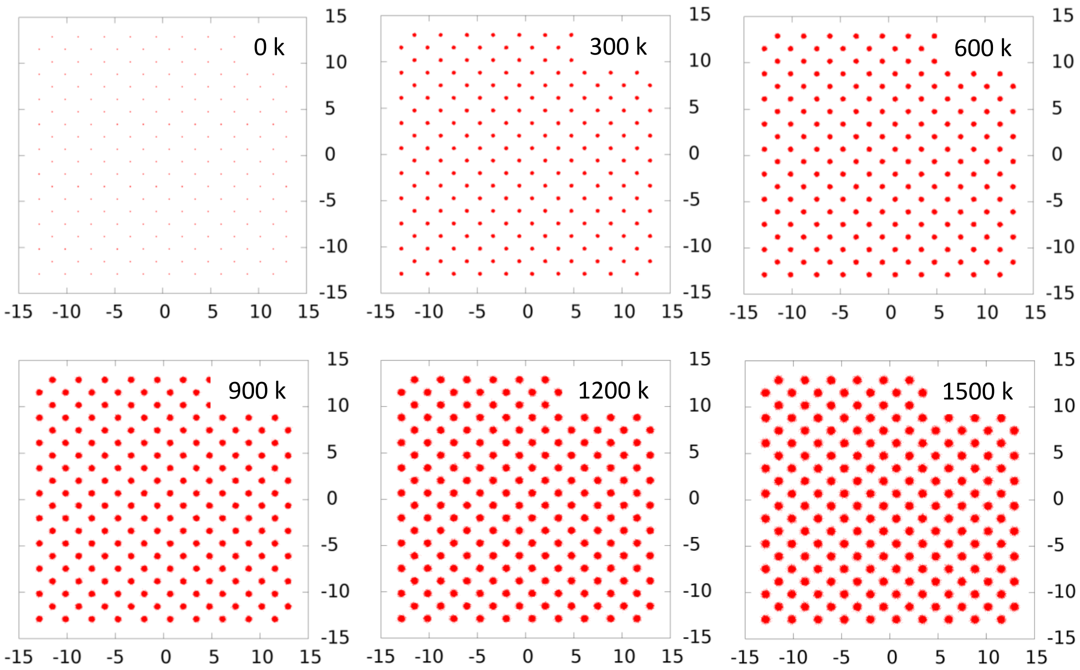

Figure 7.3: Same as Fig. 7.2 but for a simulation with 1000 Si atoms.

7.5 Numerical Results

In this section, we first present and analyze the output of our AIMD simulations and then we report the output of the charge-transport post-processing subroutine detailed in section 7.3.4.

7.5.1 Spectral analysis

In Figs. 7.2 and 7.3 we report the orbits of the atoms at different temperatures, as simulated with 216 and 1000 Si atoms, respectively. As one can see, the orbits wonder around the equilibrium positions and the data reveals that crystal Si is quite disordered even at the room temperature. Let us point out that many electronic devices operate at 600 K or higher under heavy loads. At these temperatures, the thermal disorder is quite pronounced. As it is well known, in such conditions, some of the wave functions can and will become affected by the phenomenon called Anderson localization [142]. When a wave function becomes Anderson localized, its contribution to the Kubo-formula is zero. Almost as a rule [143], these local-

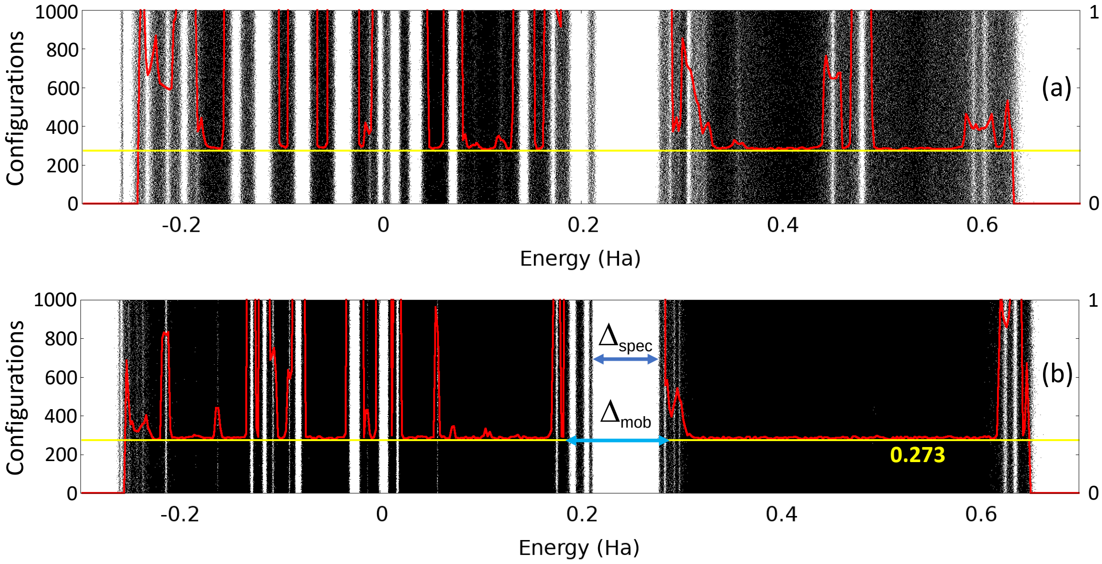

Figure 7.4: Level statistics for a (a) 3 × 3 × 3 unit cells crystal containing 216 atoms and (b) 5 × 5 × 5 unit cells crystal containing 1000 atoms. Both sets of data were generated at $T = 900$ K. The background displays the energy spectra for various thermally disordered configurations. The red curve represents the variance of the level spacings ensembles collected at different energies. The yellow line indicates the variance of the Gaussian orthogonal ensemble. Both the red and yellow curves have their y-axis on the right side. Also shown are the spectral and the mobility gaps, as inferred from the data.

ized states occur close to the edges of the energy spectrum and, for 3-dimensional crystals, it is predicted there exist mobility edges in the energy spectrum, one in the conduction and one in valence bands, beyond which the wave functions remain extended. These mobility edges define the so called mobility gap and the expectation of the charge current operator is zero when one only populates electron states with eigen-energy within this gap. It becomes clear that the activated behavior of the conductivity is determined by the mobility gap and not by the spectral gap. As such, it is extremely important to detect the mobility edges for our crystals. For this, we employ a technique called the level statistics analysis, which has been successfully used in the past for this very purpose [110, 144].

We exemplify the process for the temperature $T = 900$ K, where the disorder is quite pronounced and the effects described above are more visible. Before we start, we need to examine the spectral characteristics of the Hamiltonians. For this, we have diagonalized the tight-binding KS-Hamiltonian for 1001 selected thermally disordered configurations. The result is a sequence of 1001 discrete sets of eigenvalues $\{\epsilon_a^\omega\}$, which we rendered on a horizontal line for each configuration

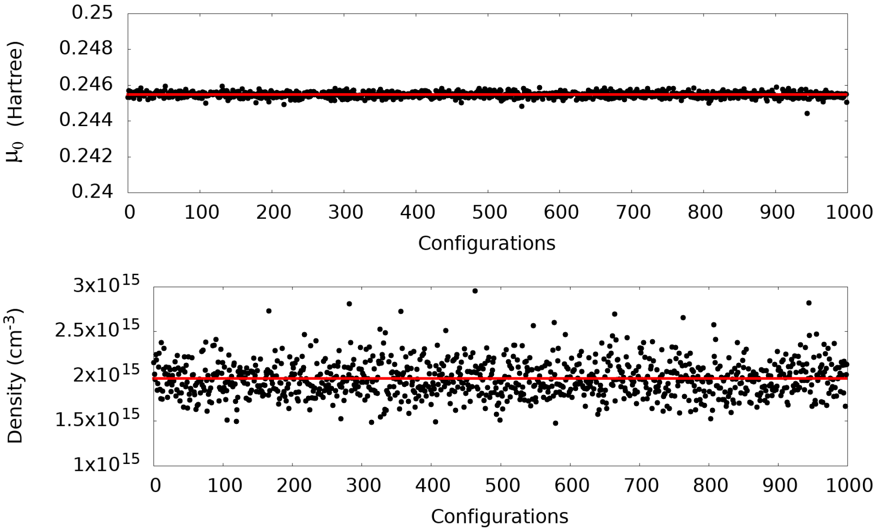

Figure 7.5: (a) Fluctuation (black dots) and average value (red line) of the chemical potential value corresponding to the charge neutrality. (b) Same as (a) for the intrinsic charge carrier density. The data was extracted from the spectra shown in Fig. 7.4(b) for a crystal containing 1000 Si atoms at temperature 900 K.

and then we stuck these lines vertically. The resulting collection of spectra then appears as the fuzzy dots seen in the background of Fig. 7.4. We recall that for covariant systems of Hamiltonians in the thermodynamic, the spectrum is in fact non-fluctuating in the sense that, if we pick any energy interval and ask what is the probability (w.r.t. to ω) for at least one eigenvalue to fall within this interval, the answer will either 0 or 100 percent. This is a consequence of the fact that $T_{\mathfrak{g}} H_\omega T_{\mathfrak{g}}^\dagger$ have the same spectrum for all $\mathfrak{g} \in \mathbb{G}$. In the same time, $T_{\mathfrak{g}} H_\omega T_{\mathfrak{g}}^\dagger = H_{\tau_{\mathfrak{g}}\omega}$ and the orbit $\{\tau_{\mathfrak{g}}\omega,\ \mathfrak{g} \in \mathbb{G}\}$ samples Ω entirely. The spectrum of a covariant family of Hamiltonians is defined as the intersection of all closed subsets of the real axis that contain all eigenvalues with 100% probability. Rendering the spectra as in Fig. 7.4 helps one identify this non-fluctuating spectral set.

We now examine the spectra more closely. The first issue we want to address is the appearance of the spectral gaps inside the valence and conduction bands. These are artificial features due to relative small size of the system. For a periodic system simulated with periodic boundary conditions (*i.e.* at Γ-point) on a finite super-cell containing many unit cells, these gaps will be explained by the coarse sampling of the Brillouin zone of the unit cell. As one can see in Fig. 7.4, many of the gaps disappear when the size of the Si crystal is increased from $3 \times 3 \times 3$ unit cells to $5 \times 5 \times 5$ unit cells. One should also note that the fuzziness in the rendered spectra decreases as the size of the system increases, which is a manifestation of the non-fluctuating character of the spectrum in the thermodynamic limit.

The second issue is the size of the spectral gap, which in our simulations comes at 1.7 eV. This is more than twice the value returned by converged KS-DFT simulations and it indicates that the local orbital basis is too coarse. We have verified that, indeed, increasing the local orbital basis converges the spectral gap to the standard KS-DFT value of 0.7 eV. We recall that the experimental value is 1.1700 eV at 4.2K [145] and that the experimental band gap displays a temperature dependence which has been assessed quite precisely [146, 147]. Our simulations, however, are performed with the same super-cell regardless of the temperature, hence we cannot relate them to that experimental fact. Our conclusions based on the spectral data reported in Fig. 7.4 is that the present simulations are not yet precise enough for quantitative predictions. As such, we will focus in the following only at qualitative aspects.

We now turn our focus on the level statics analysis, which was performed in the following way. We picked an arbitrary energy ϵ and, for each of the 1000 thermally disordered configurations considered in Fig. 7.4, we identified the unique eigenvalues ϵ_a^ω and ϵ_{a+1}^ω that satisfy the constraint $\epsilon_a^\omega < \epsilon < \epsilon_{a+1}^\omega$. Then we computed the level spacings $\Delta\epsilon = \epsilon_{a+j+1}^\omega - \epsilon_{a+j}\omega$, letting j take 11 consecutive values between -5 and 5. After repeating the procedure for all 1000 configurations, we generated ensembles of 11,0000 level spacings for each energy ϵ. These level spacings were subsequently normalized by their average.

As done in [144], one can examine the histograms of these ensembles and determine what kind of distributions they manifest. Since the KS-Hamiltonians are real, we expect the outcome to be either a Poisson distribution $P(s) = e^{-s}$ or a Gaussian orthogonal ensemble (GOE), $P_{\text{GOE}} = \frac{\pi}{2} s e^{-\frac{\pi}{4}s^2}$. These distributions are expected when the localization length of the wave functions with energy close to ϵ is smaller/larger than the size of the super-cell, respectively [148]. If the super-cell is large enough, one can derive from these distributions the localized or de-localized character of the wave functions. Overlapped over the spectra in Fig. 7.4 is the variance $\langle s^2 \rangle - \langle s \rangle^2$ of the level spacing ensembles collected at different energies, as well as the variance value of 0.273 computed from P_{GOE}. Since the variance of the Poisson ensemble is 1, we can easily identify from Fig. 7.4 the character of the

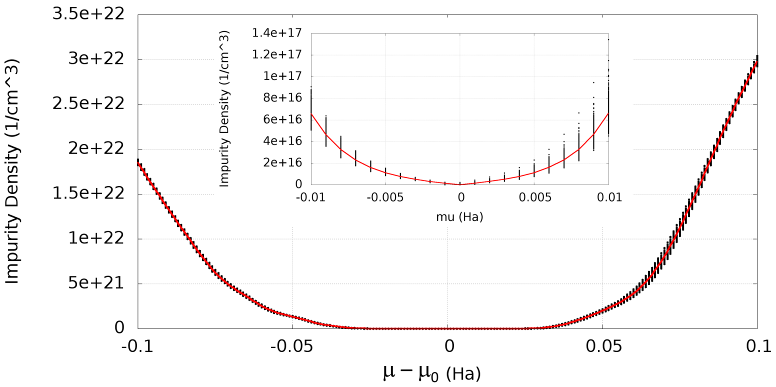

Figure 7.6: Fluctuation (black dots) and average value (red line) of the impurity density as a function of chemical potential. The inset shows a restricted range of the same data. The numerical values were extracted from the spectra shown in Fig. 7.4(b) for a crystal containing 1000 Si atoms at temperature 900 K.

wave functions, in particular, the mobility gap. As one can see, it extends well beyond the spectral gap.

7.5.2 Charge carrier concentrations

The charge-neutrality point is defined by the precise value of the chemical potential μ_0 where the charge neutrality of the crystal is achieved. Since in our calculations each ionic core carries $4e$ charge, the charge neutrality condition reads:

$$\frac{4N_a}{\mathrm{Vol}} = \left\langle \frac{2}{\mathrm{Vol}} \sum_a \frac{1}{1+\exp(\frac{\epsilon_a^\omega - \mu_0}{kT})} \right\rangle_\omega . \tag{7.5.1}$$

We want to point out that, for covariant systems, μ_0 and the quantity inside the average brackets in (7.5.1) are self-averaging in the thermodynamic limit. However, for our finite-size crystals, these quantities will display fluctuations from one thermally disordered configuration to another and the size of these fluctuations is a good indicator of how close is the simulation to the thermodynamic limit. A rendering of the fluctuations as well as the average value of the chemical potential μ_0 at the neutrality point and 900 K temperature are reported in Fig. 7.5(a). The data reveal an extremely low level of fluctuations, characterized by a standard deviation of 0.063 % around the average value $\mu_0 = 0.24546$ Ha.

Mapping the concentration of the conduction electrons and valance holes is cru-

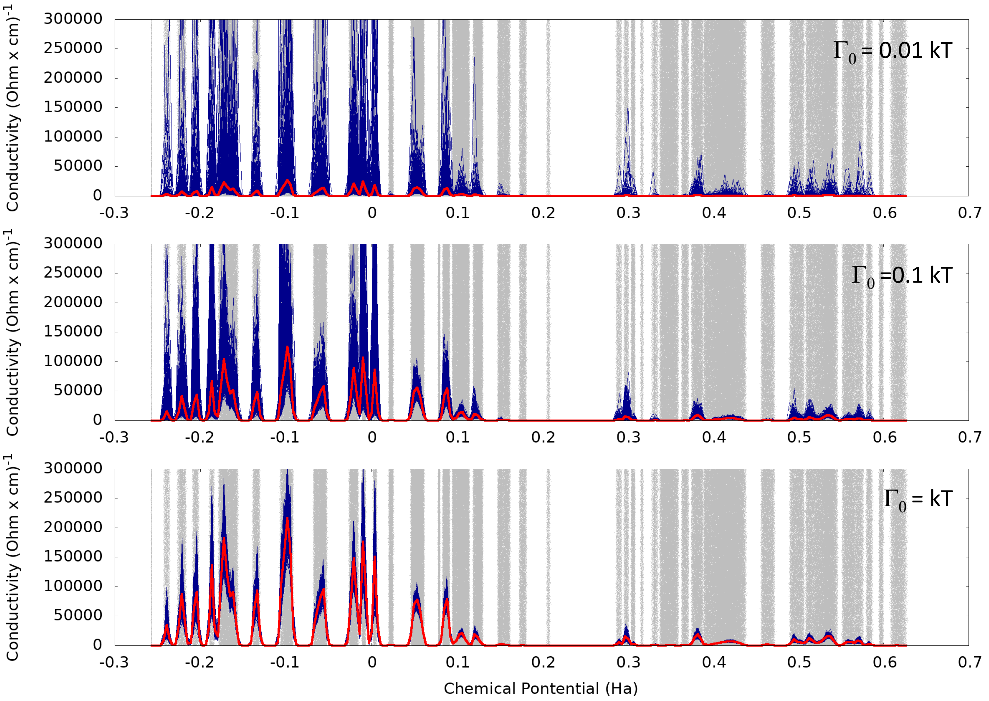

Figure 7.7: Conductivity as a function of chemical potential for 216 Si atoms, $T = 300$ K and different values of the dissipation coefficient. Shown in blue are the un-processed output for 1000 thermally disordered configurations. The red curves represent the average values.

cial for understanding the transport characteristics of crystals. The hole concentration is determined by the depletion of the valence states due to the thermal excitations:

$$n_{\mathrm{h}}(T,\mu) = \left\langle \frac{2}{\mathrm{Vol}} \sum_{\epsilon_a^\omega \leq \mu_0} \left[1 - \frac{1}{1+\exp(\frac{\epsilon_a^\omega - \mu}{kT})} \right] \right\rangle_\omega . \tag{7.5.2}$$

The concentration of the mobile electrons is determined by the population of the conduction states due to the thermal excitations:

$$n_{\mathrm{e}}(T,\mu) = \left\langle \frac{2}{\mathrm{Vol}} \sum_{\epsilon_a^\omega \geq \mu_0} \frac{1}{1+\exp(\frac{\epsilon_a^\omega - \mu}{kT})} \right\rangle_\omega . \tag{7.5.3}$$

Note that at the neutrality point, we have the equality:

$$n_{\mathrm{h}}(T,\mu_0) = n_{\mathrm{e}}(T,\mu_0). \tag{7.5.4}$$

The common value of the two densities is called the intrinsic density (n_i) of charge

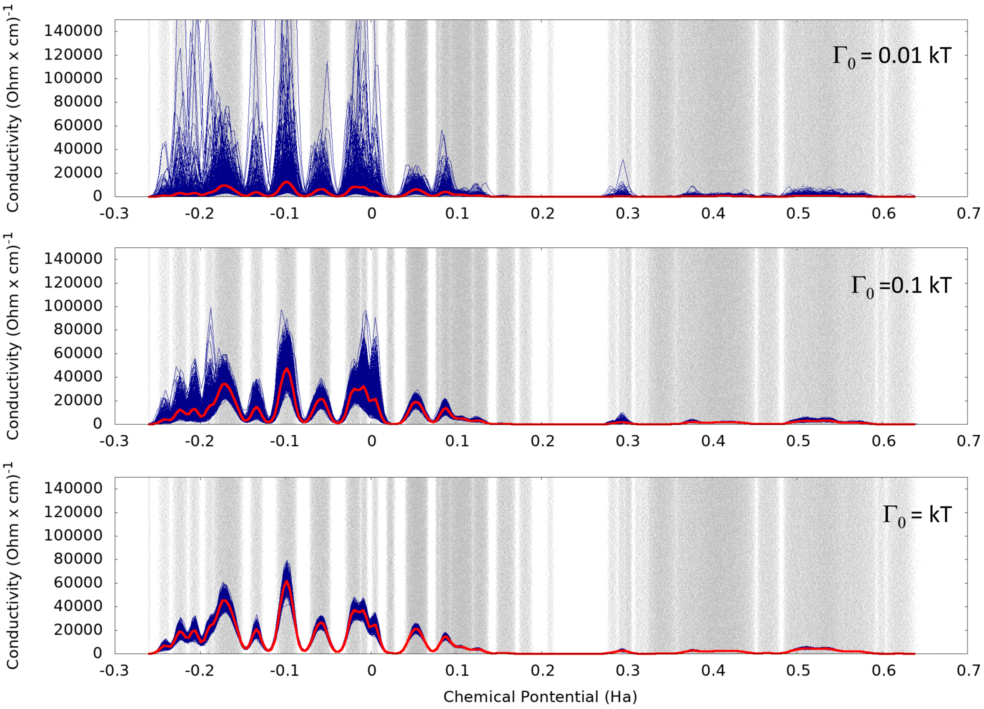

Figure 7.8: Same as Fig. 7.7 for $T = 900$ K.

carriers and it is one of the most important characteristics of Si semiconductor. Its experimental value at 300 K has been determined with great precision [149–151] to be $n_i = 9.7 \div 10.0 \times 10^9$ cm^{-3}. Experimental data on the dependence of n_i with the temperature has been summarized in [152, Fig. 14], from where we extracted the experimental value of 1.0×10^{17} cm^{-3} at $T = 900$ K. For our simulations, the fluctuations and the average value of n_i are reported in Fig. 7.5(b). As one can see, despite of extremely low fluctuations in μ_0, there are substantial fluctuations in the n_i data, which reflect the extreme sensitivity of n_i on the energy spectrum. Quantitatively, the standard deviation in Fig. 7.5(b) is 6 % and the average value is $n_i = 1.973 \times 10^{15}$. This value is much lower than the experimental value mentioned above, the main reason being the over-estimation of the band gap by our simulations.

In our study, we will consider not only neutral but also Si crystals that are away from neutrality point by letting the chemical potential μ be a variable. Experimentally, the variation of the chemical potential can be achieved via gate potentials for thin films or via impurity doping for bulk samples. Either way, such variations

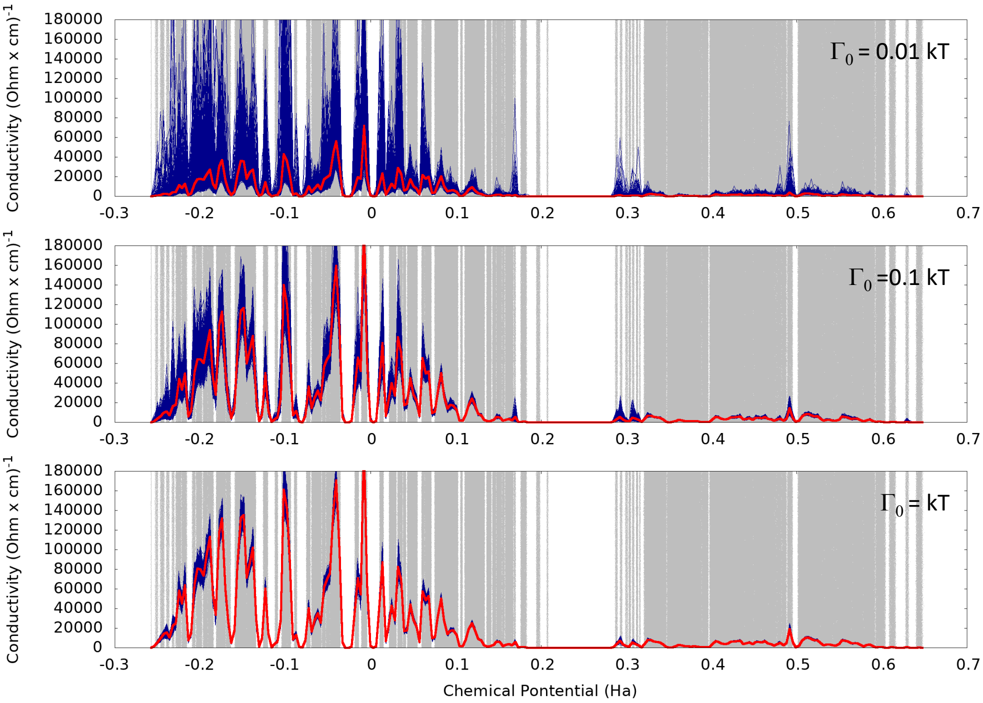

Figure 7.9: Direct conductivity as a function of the chemical potential for 1000 Si atoms, $T = 300$ K and $\Gamma_0 = 0.01kT$ (top), $\Gamma_0 = 0.1kT$ (middle) and $\Gamma_0 = kT$ (bottom). Shown in blue are the unprocessed output for 1000 thermally disordered configurations. The red curves represent the average values.

lead to changes in the electronic structure of the crystal, which should be recomputed every time the doping level is changed. Since in our simulations we use the same electronic structure, specifically the one computed at the neutrality point, the results we present here are relevant only for lightly doped or weakly gated samples where the changes in the electronic structure are expected to insignificant. To make contact with the experiment, one has to rely on the impurity density value rather than on the chemical potential, because the former is the parameter that can be controlled in laboratory. The impurity density is evaluated from:

$$n(\mu,T) = |n_{\rm e}(\mu,T) - n_{\rm h}(\mu,T)| = \left| \left\langle \frac{2}{\rm Vol} \sum_a \frac{1}{1+\exp(\frac{\epsilon_a^\omega - \mu}{kT})} \right\rangle_\omega - \frac{4N_a}{\rm Vol} \right|. \quad (7.5.5)$$

For completeness, we show in Fig. 7.6 the relation between the impurity density and chemical potential μ, as derived from the spectra shown in Fig. 7.4 and (7.5.5). Let us recall that a light to moderate doping corresponds to the experimental values

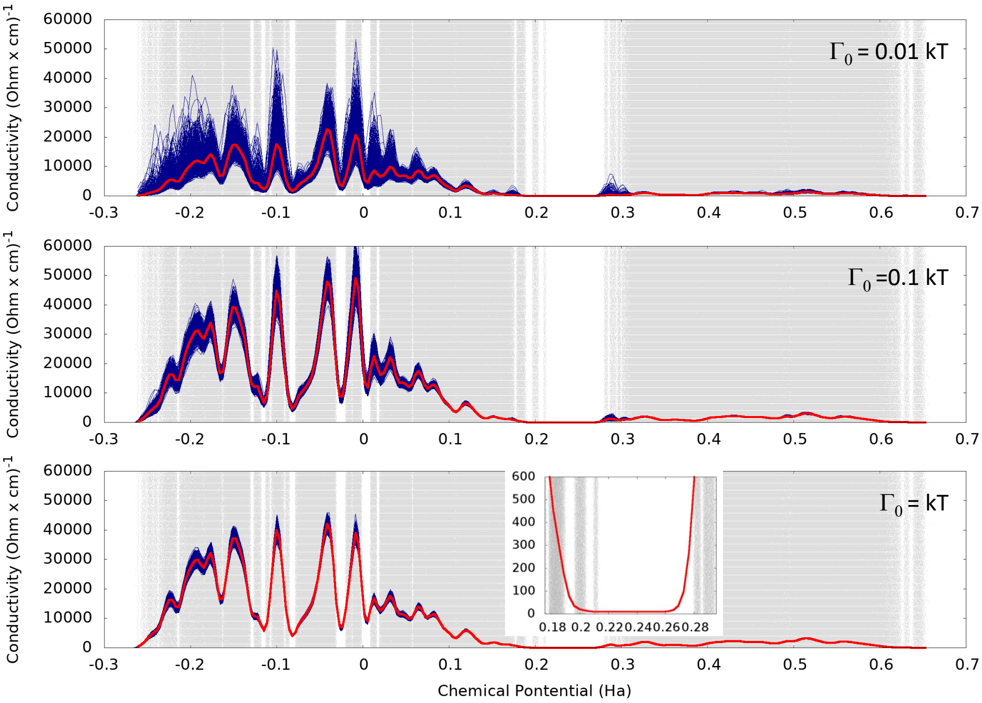

Figure 7.10: Same as Fig. 7.9 for $T = 900$ K. In addition, the bottom panel contains a zoom-in.

$n_{\text{exp}} < 10^{16}$ cm^{-3}, which in terms of the chemical potential means, approximately, that $|\mu - \mu_0| < 0.01\,$Ha.

Let us end this section by specifying that the extrinsic hole density from Eqs. (7.5.2) will be used in the next section to generate the hole mobility via the relation $\sigma = en_{\text{h}}\mu_{\text{h}}$. The hole mobility μ_{h} will be mapped as a function of the acceptor concentration (7.5.5).

7.5.3 Direct conductivity and mobilities of charge carriers

In this section we present and analyze the numerical results on the direct conductivity (7.3.17). Figs. 7.7 and 7.8 report the data for a 216 Si atoms crystal at temperatures $T = 300$ K and $T = 900$ K, respectively. Similarly, Figs. 7.9 and 7.10 report the data for a 1000 Si atoms crystal at temperatures $T = 300$ K and $T = 900$ K, respectively. The chemical potential has been varied throughout the entire energy spectral range and the dissipation parameter Γ_0 was sampled at three different values in these simulations. Overall, the results show a good correlation between the conductivity plots and the spectrum of the Kohn-Sham Hamiltonians. There is a significant difference between the outputs for 216 and 1000 atom crystals, indicating that the results are not converged yet w.r.t. the system's size. There is also a significant dependence on the dissipation parameter Γ_0. It is interesting to notice that for its largest values, the fluctuations of the direct conductivity are drastically suppressed. As explained in [110], the convergence to thermodynamic limit is faster for larger Γ_0, and this explains the suppression of the fluctuations observed in these figures.

The conductivity results are in very good agreement with the mobility gap prediction, which for $T = 900$ K can be found in Fig. 7.4. Indeed, the conductivity is obviously not influenced at all by the first band of spectrum, which was determined in Fig. 7.4 to be Anderson localized. This is quite obvious in the inset of Fig. 7.10, which shows a zoom into the region around the spectral gap. Let us point out again that, on the other hand, the intrinsic and extrinsic charge carriers are highly influenced by the presence of this Anderson localized band.

In Fig. 7.11(a), we focus on the behavior of direct conductivity inside and around the insulating gap, especially on the hole side. We chose to investigate only at the crystal with 1000 Si atoms and $T = 900$ K because it is the most converged system. At $T = 300$ K, the conductivity curves display a pronounced dependence on the spectral details which are not yet converged, hence the analysis will not be reliable. As it is customary, the transport coefficient has been plotted as a function of the acceptor concentration rather than chemical potential. The behavior of σ seen in Fig. 7.11(a) is as expected. Deep inside the insulating gap, the direct conductivity saturate at a value proportional to Γ_0 and, as the chemical potential moves towards the valence band, an activated behavior takes over. In Fig. 7.11(b), we report the hole mobility as a function of the acceptor concentration. The functional shape is in good agreement with the measured one (see [145, Fig. 21.8]). Let us point out that, when the chemical potential is inside a spectral gap, the mobility is proportional with the dissipation Γ_0, hence with inverse of the relaxation time. In contrast, when the chemical potential is inside a spectral band, as is the case of a metal, the mobility is proportional with relaxation time, hence inverse proportionally with Γ_0. As such, one should not be surprised by the behavior with Γ_0 seen in Fig. 7.11(b).

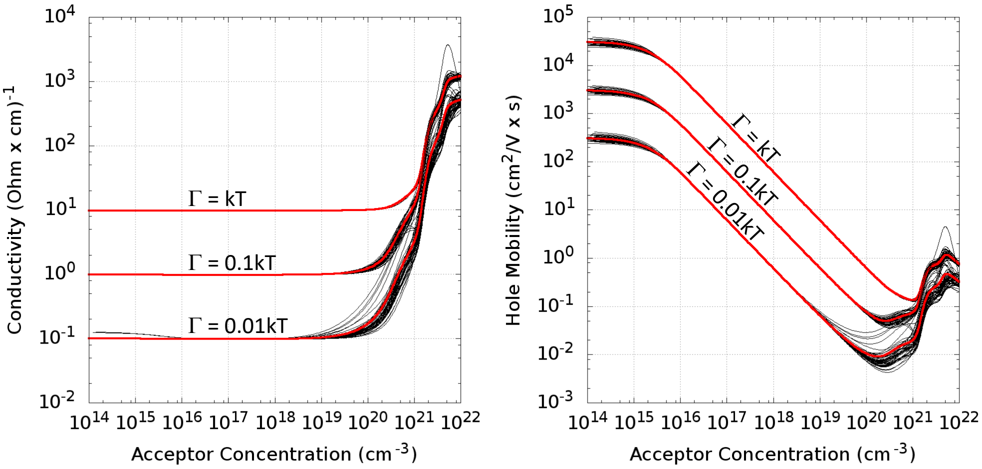

Figure 7.11: Dependence with the acceptor concentration of (a) direct conductivity and (b) hole mobility, as computed for the 1000-atom Si crystal at T = 900 K. The fine lines represent unprocessed data coming from individual disordered configurations, hence they are a measure of the fluctuations. The thicker red lines represent the averages over 50 configurations. The simulations have been carried for three values of the dissipation parameter, which are specified in each panel.

8 Conclusions

In this work, the structure and adsorption properties of K-PHI and related cation exchanged poly(heptazine imide) salts are studied by means of density functional theory calculations of an idealized model derived from experimental findings. The structure of K-PHI consists of positive potassium cations, which are embedded in the pores between the layers of a negatively charged well-organized 2D carbon nitride framework. This charge separation can be described as frustrated Coulomb pairs analogues to frustrated Lewis pairs which are known to exhibit adsorbate activation properties. The potassium cations can be exchanged experimentally with other ions while maintaining the crystal structure. Here, the potassiums were exchanged with other alkali (Li^+, Na^+, Rb^+), alkaline earth (Ca^{2+}, Sr^{2+}, Ba^{2+}) and transition metal (Au^+, Ag^+) cations as well as hydrogen atoms. All these materials have similar structures with intercalated cations between the layers except the covalent H-PHI and Au-PHI, which has the gold ions in the same layer as PHI due to a high degree of covalency as it is typical for gold and confirmed by charge analysis.

Due to the presence of positive ions as well as negative PHI layers which contain surface nitrogens as basic adsorption sites, K-PHI and their metal exchanged analogues (X-PHI) offer a unique highly-polarizing adsorption environment, which can be used for different adsorbates. The carried out calculations suggest that the adsorption environment inside these materials makes them even possible candidates for helium storage and transportation. The helium adsorption is found to be energetically favorable inside the nanopores of all studied systems although helium is known to hardly interact with any species. Even in the metal-free H-PHI system the adsorption is energetically favored which underlines the potential of metal-free CN materials. Furthermore, the adsorption energy increases for the cation containing systems and its helium affinity is determined by the cation choice. K-PHI exhibits an adsorption energy of ΔE_{ads}= -4.3 kJ/mol. The highest adsorption energies are calculated in the case of the alkali metal containing PHI materials and depend on the size of the cation as one factor for the resulting charge separation. Hence, Cs-PHI was determined as the material with the thermodynamically highest adsorption affinity (ΔE_{ads}= -5.5 kJ/mol). The origin of the interaction between helium and the X-PHI materials was determined to be dominated by Coulomb interactions as shown by the ALMO-EDA method. However, also charge transfer is significantly contributing to the interaction. The strongest charge transfer occurs from He to the positive cations in the order of 0.5 me resulting in a stabilization of around -0.8 kJ/mol. A second charge transfer contribution was determined from the negative PHI framework to He (around 0.05 me and -0.2 kJ/mol).

The highly active adsorption environment is not only interesting for helium adsorption, but also exhibits interesting possibilities for more reactive species. The water adsorption in K-PHI was investigated and a remarkable adsorption energy of -94.5 kJ/mol for a single molecule and -83.4 kJ/mol per water molecule upon complete filling of K-PHI (14 wt%). This high adsorption affinity can be explained by the fact that water can be adsorbed directly at the core of the charge separation in K-PHI. The water is closely coordinated to the positive potassium ions while at the same time forming hydrogen bonds with the surface nitrogens of the negative PHI layers. The immense adsorption energy reveals that water is not interacting in terms of regular physisorption and instead, it is becoming part of the architecture of the material. The interaction of water in K-PHI originates mainly by Coulomb as well as charge transfer contributions, which is occurring from PHI to water (20.9 me, -32.9 kJ/mol) and from water to the potassium cations (10.6 me, -10.2 kJ/mol). Since water interacts strongly with the material, it is expected to be adsorbed even at low partial pressures and not to be easily removable thereafter. Hence, it was investigated how the presence of H_2O influence the helium adsorption in K-PHI.¸ Interestingly, adsorbed water is able to slightly increase the helium affinity at low water and helium uptakes (up to -1.0 kJ/mol). However, this enhancement effect quickly vanishes at higher loadings due to competition for adsorption sites in the narrow nanopores. Also the maximum helium uptake decreases the more water is present in the pores. Therefore, K-PHI should be treated cautiously in presence of polar molecules which whom it may interact strongly. If water is not desired to fill the nanopores, these materials should be used in an anhydrous environment.

This work is a contribution to understand the structure-property relation inside poly(heptazine imides) and their unique confined adsorption environment with strongly interacting nanopores. Their immense potential is indicated for various applications, where strong interactions are desired, e. g. for molecular activation for catalytic purposes.

Furthermore, in the last chapter, disordered tight-binding models based on AIMD outputs has been derived and a Kubo-formalism was formulated that preserves the self-averaging property of the transport coefficients. The Kubo-formalism was coded as a post-processing subroutine to a standard AIMD code and preliminary results on the transport coefficients of crystals Si were obtained at various temperatures. According to the study, the thermal disorder can have measurable effects even at room temperature.

9 References

[1] J. Liebig, "Über einige Stickstoff - Verbindungen", *Annalen der Pharmacie* **1834**, *10*, 1–47.

[2] K. Gong, F. Du, Z. Xia, M. Durstock, L. Dai, "Nitrogen-Doped Carbon Nanotube Arrays with High Electrocatalytic Activity for Oxygen Reduction", *Science* **2009**, *323*, 760–764.

[3] X. Wang, K. Maeda, A. Thomas, K. Takanabe, G. Xin, J. M. Carlsson, K. Domen, M. Antonietti, "A metal-free polymeric photocatalyst for hydrogen production from water under visible light", *Nature materials* **2009**, *8*, 76–80.

[4] M.-H. Huang, X.-C. Dai, T. Li, Y.-B. Li, Y. He, G. Xiao, F.-X. Xiao, "Stimulating Charge Transfer Over Quantum Dots via Ligand-Triggered Layer-by-Layer Assembly toward Multifarious Photoredox Organic Transformation", *The Journal of Physical Chemistry C* **2019**, *123*, 9721–9734.

[5] J. Zhang, F.-X. Xiao, "Modulation of interfacial charge transfer by self-assembly of single-layer graphene enwrapped one-dimensional semiconductors toward photoredox catalysis", *Journal of Materials Chemistry A* **2017**, *5*, 23681–23693.

[6] N. Zhang, M.-Q. Yang, S. Liu, Y. Sun, Y.-J. Xu, "Waltzing with the versatile platform of graphene to synthesize composite photocatalysts", *Chemical reviews* **2015**, *115*, 10307–10377.

[7] K. N. Wood, R. O'Hayre, S. Pylypenko, "Recent progress on nitrogen/carbon structures designed for use in energy and sustainability applications", *Energy Environ. Sci.* **2014**, *7*, 1212–1249.

[8] L. Wang, C. Yang, S. Dou, S. Wang, J. Zhang, X. Gao, J. Ma, Y. Yu, "Nitrogen-doped hierarchically porous carbon networks: synthesis and applications in lithium-ion battery, sodium-ion battery and zinc-air battery", *Electrochimica Acta* **2016**, *219*, 592–603.

[9] J. Wu, Z. Pan, Y. Zhang, B. Wang, H. Peng, "The recent progress of nitrogen-doped carbon nanomaterials for electrochemical batteries", *J. Mater. Chem. A* **2018**, *6*, 12932–12944.

[10] N. Mahmood, C. Zhang, H. Yin, Y. Hou, "Graphene-based nanocomposites for energy storage and conversion in lithium batteries, supercapacitors and fuel cells", *J. Mater. Chem. A* **2014**, *2*, 15–32.

[11] A. Savateev, D. Dontsova, B. Kurpil, M. Antonietti, "Highly crystalline poly (heptazine imides) by mechanochemical synthesis for photooxidation of various organic substrates using an intriguing electron acceptor–Elemental sulfur", *Journal of Catalysis* **2017**, *350*, 203–211.

[12] V. W.-h. Lau, I. Moudrakovski, T. Botari, S. Weinberger, M. B. Mesch, V. Duppel, J. Senker, V. Blum, B. V. Lotsch, "Rational design of carbon nitride photocatalysts by identification of cyanamide defects as catalytically relevant sites", *Nature communications* **2016**, *7*, 1–10.

[13] H. Ou, L. Lin, Y. Zheng, P. Yang, Y. Fang, X. Wang, "Tri-s-triazine-based crystalline carbon nitride nanosheets for an improved hydrogen evolution", *Advanced Materials* **2017**, *29*, 1700008.

[14] J. Liu, Y. Liu, N. Liu, Y. Han, X. Zhang, H. Huang, Y. Lifshitz, S.-T. Lee, J. Zhong, Z. Kang, "Metal-free efficient photocatalyst for stable visible water splitting via a two-electron pathway", *Science* **2015**, *347*, 970–974.

[15] Z. Li, C. Kong, G. Lu, "Visible photocatalytic water splitting and photocatalytic two-electron oxygen formation over Cu-and Fe-doped g-C_3N_4", *The Journal of Physical Chemistry C* **2016**, *120*, 56–63.

[16] Y. Wang, X. Wang, M. Antonietti, "Polymeric graphitic carbon nitride as a heterogeneous organocatalyst: from photochemistry to multipurpose catalysis to sustainable chemistry", *Angewandte Chemie International Edition* **2012**, *51*, 68–89.

[17] S. Yin, J. Han, T. Zhou, R. Xu, "Recent progress in g-C_3N_4 based low cost photocatalytic system: activity enhancement and emerging applications", *Catalysis science & technology* **2015**, *5*, 5048–5061.

[18] S. Cao, J. Low, J. Yu, M. Jaroniec, "Polymeric photocatalysts based on graphitic carbon nitride", *Advanced Materials* **2015**, *27*, 2150–2176.

[19] V. W.-h. Lau, D. Klose, H. Kasap, F. Podjaski, M.-C. Pignié, E. Reisner, G. Jeschke, B. V. Lotsch, “Dark photocatalysis: storage of solar energy in carbon nitride for time-delayed hydrogen generation”, *Angewandte Chemie* **2017**, *129*, 525–529.

[20] Z. Zeng, X. Quan, H. Yu, S. Chen, Y. Zhang, H. Zhao, S. Zhang, “Carbon nitride with electron storage property: Enhanced exciton dissociation for high-efficient photocatalysis”, *Applied Catalysis B: Environmental* **2018**, *236*, 99–106.

[21] A. Savateev, B. Kurpil, A. Mishchenko, G. Zhang, M. Antonietti, “A “waiting” carbon nitride radical anion: a charge storage material and key intermediate in direct C–H thiolation of methylarenes using elemental sulfur as the “S”-source”, *Chemical science* **2018**, *9*, 3584–3591.

[22] F. Podjaski, J. Kröger, B. V. Lotsch, “Toward an aqueous solar battery: Direct electrochemical storage of solar energy in carbon nitrides”, *Advanced Materials* **2018**, *30*, 1705477.

[23] A. Savateev, S. Pronkin, M. G. Willinger, M. Antonietti, D. Dontsova, “Towards Organic Zeolites and Inclusion Catalysts: Heptazine Imide Salts Can Exchange Metal Cations in the Solid State”, *Chemistry – An Asian Journal* **2017**, *12*, 1517–1522.

[24] Z. Chen, A. Savateev, S. Pronkin, V. Papaefthimiou, C. Wolff, M. G. Willinger, E. Willinger, D. Neher, M. Antonietti, D. Dontsova, ““The Easier the Better” Preparation of Efficient Photocatalysts—Metastable Poly(heptazine imide) Salts”, *Advanced Materials* **2017**, *29*, 1700555.

[25] A. Savateev, S. Pronkin, J. D. Epping, M. G. Willinger, C. Wolff, D. Neher, M. Antonietti, D. Dontsova, “Potassium Poly(heptazine imides) from Aminotetrazoles: Shifting Band Gaps of Carbon Nitride-like Materials for More Efficient Solar Hydrogen and Oxygen Evolution”, *ChemCatChem* **2017**, *9*, 167–174.

[26] L. Lin, W. Ren, C. Wang, A. Asiri, J. Zhang, X. Wang, “Crystalline carbon nitride semiconductors prepared at different temperatures for photocatalytic hydrogen production”, *Applied Catalysis B: Environmental* **2018**, *231*, 234–241.

[27] C. Faul, M. Antonietti, “Ionic Self-Assembly: Facile Synthesis of Supramolecular Materials”, *Advanced Materials* **2003**, *15*, 673–683.

[28] K. Mizushima, P. Jones, P. Wiseman, J. B. Goodenough, “Li_xCoO_2 (0<x<1): A new cathode material for batteries of high energy density”, *Materials Research Bulletin* **1980**, *15*, 783–789.

[29] M. Thomas, P. Bruce, J. Goodenough, “Lithium mobility in the layered oxide $Li_{1-x}CoO_2$”, *Solid State Ionics* **1985**, *17*, 13–19.

[30] H. Ma, B. Liu, B. Li, L. Zhang, Y.-G. Li, H.-Q. Tan, H.-Y. Zang, G. Zhu, “Cationic covalent organic frameworks: a simple platform of anionic exchange for porosity tuning and proton conduction”, *Journal of the American Chemical Society* **2016**, *138*, 5897–5903.

[31] E. Wirnhier, M. Döblinger, D. Gunzelmann, J. Senker, B. V. Lotsch, W. Schnick, “Poly (triazine imide) with intercalation of lithium and chloride ions $[(C_3N_3)_2(NH_xLi_{1-x})_3{\cdot}LiCl]$: a crystalline 2D carbon nitride network”, *Chemistry–A European Journal* **2011**, *17*, 3213–3221.

[32] M. B. Mesch, K. Bärwinkel, Y. Krysiak, C. Martineau, F. Taulelle, R. B. Neder, U. Kolb, J. Senker, “Solving the hydrogen and lithium substructure of poly (triazine imide)/LiCl using NMR crystallography”, *Chemistry–A European Journal* **2016**, *22*, 16878–16890.

[33] Y. Ham, K. Maeda, D. Cha, K. Takanabe, K. Domen, “Synthesis and Photocatalytic Activity of Poly (triazine imide)”, *Chemistry–An Asian Journal* **2013**, *8*, 218–224.

[34] C. Fettkenhauer, J. Weber, M. Antonietti, D. Dontsova, “Novel carbon nitride composites with improved visible light absorption synthesized in $ZnCl_2$-based salt melts”, *RSC advances* **2014**, *4*, 40803–40811.

[35] C. Fettkenhauer, G. Clavel, K. Kailasam, M. Antonietti, D. Dontsova, “Facile synthesis of new, highly efficient SnO_2/carbon nitride composite photocatalysts for the hydrogen evolution reaction”, *Green Chemistry* **2015**, *17*, 3350–3361.

[36] D. W. Stephan, G. Erkner, “Frustrated Lewis Pairs: Metal-free Hydrogen Activation and More”, *Angew. Chem. Int. Ed.* **2010**, *49*, 46–76.

[37] L. Greb, P. Ona-Burgos, B. Schirmer, D. W. Stephan, S. Grimme, J. Paradies, “Metal-free Catalytic Olefin Hydrogenation: Low-Temperature H_2-Activation by Frustrated Lewis Pairs”, *Angew. Chem. Int. Ed.* **2012**, *51*, 10164–10168.

[38] D. W. Stephan, G. Erkner, “Frustrated Lewis Pair Chemistry: Development and Perspectives”, *Angew. Chem. Int. Ed.* **2015**, *54*, 2–44.

[39] J. Paradies, “From structure to novel reactivity in frustrated Lewis pairs”, *Coord. Chem. Rev.* **2019**, *380*, 170–183.

[40] K. Alix, M.-L. David, J. Dérès, C. Hébert, L. Pizzagalli, “Evolution of the properties of helium nanobubbles during in situ annealing probed by spectrum imaging in the transmission electron microscope”, *Phys. Rev. B* **2018**, *97*, 104102.

[41] W. Jäger, R. Manzke, H. Trinkaus, G. Crecelius, R. Zeller, J. Fink, H. Bay, “Density and pressure of helium in small bubbles in metals”, *Journal of Nuclear Materials* **1982**, *111-112*, 674–680.

[42] C. A. Walsh, J. Yuan, L. M. Brown, “A procedure for measuring the helium density and pressure in nanometre-sized bubbles in irradiated materials using electron-energy-loss spectroscopy”, *Philosophical Magazine A* **2000**, *80*, 1507–1543.

[43] M.-L. David, F. Pailloux, V. Mauchamp, L. Pizzagalli, “In situ probing of helium desorption from individual nanobubbles under electron irradiation”, *Appl. Phys. Lett.* **2011**, *98*, 171903.

[44] J. Jia, L. Shi, X. Lai, Q. Wang, “Preparation of Al thin films charged with helium by DC magnetron sputtering”, *Nuclear Instruments and Methods in Physics Research Section B: Beam Interactions with Materials and Atoms* **2007**, *263*, 446–450.

[45] V. Godinho, F. J. Ferrer, B. Fernńdez, J. Caballero-Hernández, J. Gómez-Camacho, A. Fernńdez, “Characterization and Validation of a-Si Magnetron-Sputtered Thin Films as Solid He Targets with High Stability for Nuclear Reactions”, *ACS Omega* **2016**, *1*, 1229–1238.

[46] R. Schierholz, B. Lacroix, V. Godinho, J. Caballero-Hernández, M. Duchamp, A. Fernández, “STEM–EELS analysis reveals stable high-density He in nanopores of amorphous silicon coatings deposited by magnetron sputtering”, *Nanotechnology* **2015**, *26*, 075703.

[47] H. Zheng, S. Liu, H. B. Yu, L. . Wang, C. Z. Liu, L. Q. Shi, “Introduction of helium into metals by magnetron sputtering deposition method”, *Mater. Lett.* **2005**, *59*, 1071–1075.

[48] D. Chandler, “Interfaces and the driving force of hydrophobic assembly”, *Nature* **2005**, *437*, 640–647.

[49] K. Koch, H. F. Bohn, W. Barthlott, “Hierarchically Sculptured Plant Surfaces and Superhydrophobicity”, *Langmuir* **2009**, *25*, PMID: 19634871, 14116–14120.

[50] S. Törnroth-Horsefield, Y. Wang, K. Hedfalk, U. Johanson, M. Karlsson, E. Tajkhorshid, R. Neutze, P. Kjellbom, “Structural mechanism of plant aquaporin gating”, *Nature* **2006**, *439*, 688–694.

[51] G. Li, P. Xiao, P. Webley, J. Zhang, R. Singh, M. Marshall, “Capture of CO_2 from high humidity flue gas by vacuum swing adsorption with zeolite 13X”, *Adsorption* **2008**, *14*, 415–422.

[52] P. Herves, M. Perez-Lorenzo, L. M. Liz-Marzan, J. Dzubiella, Y. Lu, M. Ballauff, “Catalysis by metallic nanoparticles in aqueous solution: model reactions”, *Chemical Society Reviews* **2012**, *41*, 5577–5587.

[53] S. Porada, R. Zhao, A. Van Der Wal, V. Presser, P. Biesheuvel, “Review on the science and technology of water desalination by capacitive deionization”, *Progress in materials science* **2013**, *58*, 1388–1442.

[54] B. Grünberg, T. Emmler, E. Gedat, I. Shenderovich, G. H. Findenegg, H.-H. Limbach, G. Buntkowsky, “Hydrogen bonding of water confined in mesoporous silica MCM-41 and SBA-15 studied by 1H solid-state NMR”, *Chemistry–A European Journal* **2004**, *10*, 5689–5696.

[55] T. D. Kühne, J. Heske, E. Prodan, “Disordered Crystals from First Principles II: Transport Coefficients”, *Annals of Physics* **2020**, *421*, 168290.

[56] K. Capelle, “A bird’s-eye view of density-functional theory”, *Brazilian journal of physics* **2006**, *36*, 1318–1343.

[57] W. Koch, M. C. Holthausen, *A chemist’s guide to density functional theory*, John Wiley & Sons, **2015**.

[58] R. Dreizler, E. Gross, *Density Functional Theory*, Springer Verlag, **1990**.

[59] R. G. Parr et al., *W. Yang Density functional theory of atoms and molecules*, Oxford University Press, **1989**.

[60] R. O. Jones, O. Gunnarsson, “The density functional formalism, its applications and prospects”, *Reviews of Modern Physics* **1989**, *61*, 689.

[61] J. Seminario (Ed.), *Recent Developments and Applications of Modern Density Functional Theory Theoretical and Computational Chemistry*, Elsevier, Amsterdam, **1996**.

[62] E. Schrödinger, “Quantisierung als Eigenwertproblem”, *Annalen der Physik* **1926**, *384*, 361–376.

[63] E. Schrödinger, “Quantisierung als Eigenwertproblem”, *Annalen der Physik* **1926**, *384*, 489–527.

[64] M. Born, R. Oppenheimer, “Zur Quantentheorie der Molekeln”, *Annalen der Physik* **1927**, *389*, 457–484.

[65] P. Hohenberg, W. Kohn, “Inhomogeneous electron gas”, *Physical review* **1964**, *136*, B864.

[66] L. H. Thomas in Mathematical proceedings of the Cambridge philosophical society, *Vol. 23*, Cambridge University Press, **1927**, pp. 542–548.

[67] E. Fermi, “Eine statistische Methode zur Bestimmung einiger Eigenschaften des Atoms und ihre Anwendung auf die Theorie des periodischen Systems der Elemente”, *Zeitschrift für Physik* **1928**, *48*, 73–79.

[68] W. Kohn, L. J. Sham, “Self-consistent equations including exchange and correlation effects”, *Physical review* **1965**, *140*, A1133.

[69] J. P. Perdew, K. Burke, M. Ernzerhof, “Generalized Gradient Approximation Made Simple”, *Phys. Rev. Lett.* **1996**, *77*, 3865–3868.

[70] A. D. Becke, “Density-functional exchange-energy approximation with correct asymptotic behavior”, *Physical review A* **1988**, *38*, 3098.

[71] C. Lee, W. Yang, R. G. Parr, “Development of the Colle-Salvetti correlation-energy formula into a functional of the electron density”, *Phys. Rev. B* **1988**, *37*, 785–789.

[72] R. Staub, M. Iannuzzi, R. Z. Khaliullin, S. N. Steinmann, “Energy Decomposition Analysis for Metal Surface–Adsorbate Interactions by Block Localized Wave Functions”, *J. Chem. Theory Comput.* **2019**, *15*, 265–275.

[73] R. Z. Khaliullin, T. D. Kühne, “Microscopic properties of liquid water from combined ab initio molecular dynamics and energy decomposition studies”, *Physical Chemistry Chemical Physics* **2013**, *15*, 15746–15766.

[74] T. D. Kühne, R. Z. Khaliullin, “Electronic signature of the instantaneous asymmetry in the first coordination shell of liquid water”, *Nature communications* **2013**, *4*, 1–7.

[75] T. D. Kühne, R. Z. Khaliullin, “Nature of the asymmetry in the hydrogen-bond networks of hexagonal ice and liquid water”, *Journal of the American Chemical Society* **2014**, *136*, 3395–3399.

[76] R. Staub, M. Iannuzzi, R. Z. Khaliullin, S. N. Steinmann, "Energy decomposition analysis for metal surface–Adsorbate interactions by block localized wave functions", *Journal of Chemical Theory and Computation* **2018**, *15*, 265–275.

[77] W. Humphrey, A. Dalke, K. Schulten, "VMD: visual molecular dynamics", *Journal of molecular graphics* **1996**, *14*, 33–38.

[78] B. G. Lippert, J. Hutter, M. Parrinello, "A hybrid Gaussian and plane wave density functional scheme", *Molecular Physics* **1997**, *92*, 477–488.

[79] T. D. Kühne, M. Iannuzzi, M. Del Ben, V. V. Rybkin, P. Seewald, F. Stein, T. Laino, R. Z. Khaliullin, O. Schütt, F. Schiffmann, et al., "CP2K: An electronic structure and molecular dynamics software package-Quickstep: Efficient and accurate electronic structure calculations", *The Journal of Chemical Physics* **2020**, *152*, 194103.

[80] J. VandeVondele, J. Hutter, "Gaussian basis sets for accurate calculations on molecular systems in gas and condensed phases", *The Journal of chemical physics* **2007**, *127*, 114105.

[81] S. Goedecker, M. Teter, J. Hutter, "Separable dual-space Gaussian pseudopotentials", *Physical Review B* **1996**, *54*, 1703.

[82] M. Krack, "Pseudopotentials for H to Kr optimized for gradient-corrected exchange-correlation functionals", *Theoretical Chemistry Accounts* **2005**, *114*, 145–152.

[83] S. Grimme, "Semiempirical GGA-type density functional constructed with a long-range dispersion correction", *Journal of computational chemistry* **2006**, *27*, 1787–1799.

[84] R. Fletcher, *Practical Methods Of Optimization: Vol. 1 Unconstrained Optimization*, John Wiley & Sons, New York, NY, USA, **1980**.

[85] R. S. Mulliken, "Electronic Population Analysis on LCAO-MO Molecular Wave Functions. I", *J. Chem. Phys.* **1955**, *23*, 1833–1840.

[86] T. A. Manz, D. S. Sholl, "Chemically Meaningful Atomic Charges That Reproduce the Electrostatic Potential in Periodic and Nonperiodic Materials", *J. Chem. Theory Comput.* **2010**, *6*, 2455–2468.

[87] T. Manz, N. Limas, "Introducing DDEC6 atomic population analysis: part 1. Charge partitioning theory and methodology.", *RSC Adv.* **2016**, *6 (53)*, 47771–47801.

[88] L.-S. Wang, "Covalent gold", *Phys. Chem. Chem. Phys.* **2010**, *12*, 8694–8705.

[89] D. R. Lide, *CRC handbook of chemistry and physics*, *Vol. 85*, CRC press, Boca Raton, Fla., **2004**.

[90] R. Z. Khaliullin, E. A. Cobar, R. C. Lochan, A. T. Bell, M. Head-Gordon, "Unravelling the Origin of Intermolecular Interactions Using Absolutely Localized Molecular Orbitals", *J. Phys. Chem. A* **2007**, *111*, 8753–8765.

[91] M. Uematsu, E. U. Frank, "Static Dielectric Constant of Water and Steam", *Journal of Physical and Chemical Reference Data* **1980**, *9*, 1291–1306.

[92] E. Abrahams, P. Anderson, D. Licciardello, T. Ramakrishnan, "Scaling theory of localization: Absence of quantum diffusion in two dimensions", *Physical Review Letters* **1979**, *42*, cited By 4770, 673–676.

[93] H. Ocampo, E. Pariguan, S. Paycha, *Geometric and Topological Methods for Quantum Field Theory*, Cambridge University Press, **2010**.

[94] J. Bellissard, *Prog. Math.* **2015**, *309*, cited By 1, 403–426.

[95] D. Fitting, W. Dubé, T. Siewert, "Monitoring the solidification of single-crystal castings using high-energy X-ray diffraction", *JOM* **1999**, *51*.

[96] J. Song, E. Prodan, "Quantization of topological invariants under symmetry-breaking disorder", *Physical Review B* **2015**, *92*, 195119.

[97] T. D. Kühne, E. Prodan, "Disordered crystals from first principles I: Quantifying the configuration space", *Annals of Physics* **2018**, *391*, 120–149.

[98] T. D. Kühne, M. Krack, F. R. Mohamed, M. Parrinello, "Efficient and accurate Car-Parrinello-like approach to Born-Oppenheimer molecular dynamics", *Physical review letters* **2007**, *98*, 066401.

[99] T. D. Kühne, "Second generation Car–Parrinello molecular dynamics", *WIREs Computational Molecular Science* **2014**, *4*, 391–406.

[100] T. D. Kühne, M. Iannuzzi, M. Del Ben, V. V. Rybkin, P. Seewald, F. Stein, T. Laino, R. Z. Khaliullin, O. Schütt, F. Schiffmann, et al., "CP2K: An electronic structure and molecular dynamics software package-Quickstep: Efficient and accurate electronic structure calculations", *The Journal of Chemical Physics* **2020**, *152*, 194103.

[101] J. Bellissard, A. van Elst, H. Schulz-Baldes, "The noncommutative geometry of the quantum Hall effect", *Journal of Mathematical Physics* **1994**, *35*, 5373–5451.

[102] H. Schulz-Baldes, J. Bellissard, "A kinetic theory for quantum transport in aperiodic media", *Journal of statistical physics* **1998**, *91*, 991–1026.

[103] H. Schulz-Baldes, J. Bellissard, “Anomalous transport: a mathematical framework”, *Reviews in Mathematical Physics* **1998**, *10*, 1–46.

[104] G. Androulakis, J. Bellissard, C. Sadel, “Dissipative dynamics in semiconductors at low temperature”, *Journal of Statistical Physics* **2012**, *147*, 448–486.

[105] E. Prodan, “Quantum transport in disordered systems under magnetic fields: A study based on operator algebras”, *Applied Mathematics Research eXpress* **2013**, *2013*, 176–265.

[106] Y. Xue, E. Prodan, “Noncommutative Kubo formula: Applications to transport in disordered topological insulators with and without magnetic fields”, *Physical Review B* **2012**, *86*, 155445.

[107] Y. Xue, E. Prodan, “Quantum criticality at the Chern-to-normal insulator transition”, *Physical Review B* **2013**, *87*, 115141.

[108] J. Song, E. Prodan, “Characterization of the quantized Hall insulator phase in the quantum critical regime”, *EPL (Europhysics Letters)* **2014**, *105*, 37001.

[109] E. Prodan, J. Bellissard, “Mapping the current–current correlation function near a quantum critical point”, *Annals of Physics* **2016**, *368*, 1–15.

[110] E. Prodan, *A computational non-commutative geometry program for disordered topological insulators*, *Vol. 23*, Springer, **2017**.

[111] E. Cances, P. Cazeaux, M. Luskin, “Generalized Kubo formulas for the transport properties of incommensurate 2D atomic heterostructures”, *Journal of Mathematical Physics* **2017**, *58*, 063502.

[112] D. Massatt, S. Carr, M. Luskin, C. Ortner, “Incommensurate heterostructures in momentum space”, *Multiscale Modeling & Simulation* **2018**, *16*, 429–451.

[113] D. Massatt, S. Carr, M. Luskin, “Efficient computation of Kubo conductivity for incommensurate 2D heterostructures”, *The European Physical Journal B* **2020**, *93*, 1–9.

[114] J. Singh, *Physics of Semiconductors and Their Heterostructures*, **1992**.

[115] H. Wondratschek, U. Müller, *International Tables for Crystallography, Vol. A1*, Dordrecht: Kluwer Academic Publishers, **2004**.

[116] D. Ruelle, *Statistical Mechanics: Rigorous Results, Addison*, Wesely Publishing Co., Inc.(1969 and 1989), **1969**.

[117] W. Kohn, L. J. Sham, “Self-consistent equations including exchange and correlation effects”, *Physical review* **1965**, *140*, A1133.

[118] E. Prodan, P. Nordlander, “On the Kohn-Sham equations with periodic background potentials”, *Journal of Statistical Physics* **2003**, *111*, 967–992.

[119] É. Cancès, S. Lahbabi, M. Lewin in XVIIth International Congress on Mathematical Physics, World Scientific, **2014**, pp. 549–557.

[120] S. Lahbabi, PhD thesis, Université de Cergy Pontoise, **2013**.

[121] W. Kohn, L. J. Sham, “Self-consistent equations including exchange and correlation effects”, *Physical review* **1965**, *140*, A1133.

[122] D. M. Ceperley, B. J. Alder, “Ground state of the electron gas by a stochastic method”, *Physical review letters* **1980**, *45*, 566.

[123] G. D. Birkhoff, “Proof of the ergodic theorem”, *Proceedings of the National Academy of Sciences* **1931**, *17*, 656–660.

[124] C. Bourne, E. Prodan, “Non-commutative Chern numbers for generic aperiodic discrete systems”, *Journal of Physics A: Mathematical and Theoretical* **2018**, *51*, 235202.

[125] A. Alavi, D. Frenkel, “Grand-canonical simulations of solvated ideal fermions. Evidence for phase separation”, *The Journal of chemical physics* **1992**, *97*, 9249–9257.

[126] A. Alavi, J. Kohanoff, M. Parrinello, D. Frenkel, “Ab initio molecular dynamics with excited electrons”, *Physical review letters* **1994**, *73*, 2599.

[127] J. Harris, “Simplified method for calculating the energy of weakly interacting fragments”, *Physical Review B* **1985**, *31*, 1770.

[128] W. M. C. Foulkes, R. Haydock, “Tight-binding models and density-functional theory”, *Physical review B* **1989**, *39*, 12520.

[129] N. D. Mermin, “Thermal properties of the inhomogeneous electron gas”, *Physical Review* **1965**, *137*, A1441.

[130] F. R. Krajewski, M. Parrinello, “Stochastic linear scaling for metals and nonmetals”, *Physical Review B* **2005**, *71*, 233105.

[131] C. John, T. Spura, S. Habershon, T. D. Kühne, “Quantum ring-polymer contraction method: Including nuclear quantum effects at no additional computational cost in comparison to ab initio molecular dynamics”, *Physical Review E* **2016**, *93*, 043305.

[132] I. Montvay, G. Münster, *Quantum fields on a lattice*, Cambridge University Press, **1997**.

[133] M. Ceriotti, T. D. Kühne, M. Parrinello, "An efficient and accurate decomposition of the Fermi operator", *The Journal of chemical physics* **2008**, *129*, 024707.

[134] M. Ceriotti, T. D. Kühne, M. Parrinello in AIP Conference Proceedings, *Vol. 1148*, American Institute of Physics, **2009**, pp. 658–661.

[135] E. M. Godfrin, "A method to compute the inverse of an n-block tridiagonal quasi-Hermitian matrix", *Journal of Physics: Condensed Matter* **1991**, *3*, 7843.

[136] D. Richters, T. D. Kühne, "Self-consistent field theory based molecular dynamics with linear system-size scaling", *The Journal of chemical physics* **2014**, *140*, 134109.

[137] W. H. Press, S. A. Teukolsky, W. T. Vetterling, B. P. Flannery, *Numerical recipes: the art of scientific computing. Vol. 2*, Cambridge university press Cambridge, **1992**.

[138] J. B. Kogut, "The lattice gauge theory approach to quantum chromodynamics", *Reviews of Modern Physics* **1983**, *55*, 775.

[139] J. VandeVondele, J. Hutter, "Gaussian basis sets for accurate calculations on molecular systems in gas and condensed phases", *The Journal of chemical physics* **2007**, *127*, 114105.

[140] S. Goedecker, M. Teter, J. Hutter, "Separable dual-space Gaussian pseudopotentials", *Physical Review B* **1996**, *54*, 1703.

[141] M. Krack, "Pseudopotentials for H to Kr optimized for gradient-corrected exchange-correlation functionals", *Theoretical Chemistry Accounts* **2005**, *114*, 145–152.

[142] E. Abrahams, P. Anderson, D. Licciardello, T. Ramakrishnan, "Scaling theory of localization: Absence of quantum diffusion in two dimensions", *Physical Review Letters* **1979**, *42*, 673.

[143] M. Aizenman in *The state of matter: a volume dedicated to EH Lieb*, World Scientific, **1994**, pp. 367–395.

[144] E. Prodan, "Disordered topological insulators: a non-commutative geometry perspective", *Journal of Physics A: Mathematical and Theoretical* **2011**, *44*, 113001.

[145] S. O. Kasap, P. Capper, *Springer handbook of electronic and photonic materials*, *Vol. 11*, Springer, **2006**.

[146] Y. P. Varshni, "Temperature dependence of the energy gap in semiconductors", *physica* **1967**, *34*, 149–154.

[147] K. O'donnell, X. Chen, "Temperature dependence of semiconductor band gaps", *Applied physics letters* **1991**, *58*, 2924–2926.

[148] K. Efetov, *Supersymmetry in disorder and chaos*, Cambridge university press, **1999**.

[149] A. Sproul, M. Green, "Improved value for the silicon intrinsic carrier concentration from 275 to 375 K", *Journal of applied physics* **1991**, *70*, 846–854.

[150] K. Misiakos, D. Tsamakis, "Accurate measurements of the silicon intrinsic carrier density from 78 to 340 K", *Journal of applied physics* **1993**, *74*, 3293–3297.

[151] P. P. Altermatt, A. Schenk, F. Geelhaar, G. Heiser, "Reassessment of the intrinsic carrier density in crystalline silicon in view of band-gap narrowing", *Journal of Applied Physics* **2003**, *93*, 1598–1604.

[152] C. Thurmond, "The standard thermodynamic functions for the formation of electrons and holes in Ge, Si, GaAs, and GaP", *Journal of the Electrochemical Society* **1975**, *122*, 1133.

10 Appendix

10.1 Acknowledgements

First of all, I would like to thank Thomas, who aroused my interest and deepened my knowledge of theoretical chemistry. He was always willing to help and I really appreciated the working environment in the AK Kühne. I had a very joyful time during work and breaks and I want to thank all my colleagues for this. Furthermore, I learned a lot from my second supervisor Markus and I want to thank him for his help with his impressive chemical view of things and his financial support. I am grateful for having both of them as my supervisors and for the opportunity to work on exciting projects with top scientists from UPB, MPIKG and other national and international institutes during my Ph.D. Additionally, I want to thank my private environment, especially my girlfriend Saskia, my family and my close friends, who are very important to me and always support me.

10.2 Publications

[1] R. Walczak, A. Savateev, J. Heske, N. V. Tarakina, S. Sahoo, J. D. Epping, T. D. Kühne, B. Kurpil, M. Antonietti, M. Oschatz, "Controlling the Strength of Interaction between Carbon Dioxide and Nitrogen-rich Carbon Materials by Molecular Design", *Sustainable Energy Fuels* **2019**, *3*, 2819–2827.

[2] T. Clark, J. Heske, T. D. Kühne, "Opposing Electronic and Nuclear Quantum Effects on Hydrogen Bonds in H_2O and D_2O", *ChemPhysChem* **2019**, *20*, 2461–2465.

[3] S. K. Sahoo, J. Heske, S. Azadi, Z. Zhang, N. V. Tarakina, M. Oschatz, R. Z. Khaliullin, M. Antonietti, T. D. Kühne, "On the Possibility of Helium Adsorption in Nitrogen Doped Graphitic Materials", *Sci. Rep.* **2020**, *10*, 5832.

[4] S. K. Sahoo, J. Heske, M. Antonietti, Q. Qin, M. Oschatz, T. D. Kühne, "Electrochemical N_2 Reduction to Ammonia Using Single Au/Fe Atoms Supported on Nitrogen-Doped Porous Carbon", *ACS Appl. Energy Mater.* **2020**, *3*, 10061–10069.

[5] T. D. Kühne, J. Heske, E. Prodan, "Disordered Crystals from First Principles II: Transport Coefficients", *Annals of Physics* **2020**, *421*, 168290.

[6] J. Kossmann, D. Piankova, N. V. Tarakina, J. Heske, T. D. Kühne, J. Schmidt, M. Antonietti, N. Lopez-Salas, "Guanine Condensates as Covalent Materials and the Concept of Cryptopores", *Carbon* **2021**, *172*, 497–505.

[7] S. K. Sahoo, I. F. Teixeira, A. Naik, J. Heske, D. Cruz, M. Antonietti, A. Savateev, T. D. Kühne, "Photocatalytic Water Splitting Reaction Catalyzed by Ion-Exchanged Salts of Potassium Poly(heptazine imide) 2D Materials", *J. Phys. Chem. C* **2021**, *125*, 13749–13758.

[8] J. Heske, R. Walczak, J. D. Epping, S. Youk, S. K. Sahoo, M. Antonietti, T. D. Kühne, M. Oschatz, "When Water becomes an Integral Part of Carbon – Combining Theory and Experiment to Understand the Zeolite-like Water Adsorption Properties of Porous C_2N Materials", *J. Mater. Chem. A* **2021**.

[9] E. Lepre, J. Heske, M. Nowakowski, E. Scoppola, I. Zizak, T. Heil, T. D. Kühne, M. Antonietti, J. Alber, N. Lopez-Salas, "Ni-Based Electrocatalysts for Unconventional CO_2 Reduction Reaction to Formic Acid", *Nano Energy* **2022**.

[10] M. Odziomek, P. Giusto, J. Kossmann, N. V. Tarakina, J. Heske, S. M. Rivadeneira, T. D. K"uhne, S. Mazzanti, O. Savatieiev, M. Antonietti, N. Lopez-Salas, "Red Carbon Derived Materials: Rediscovered Organic Semiconductors", *submitted to Advanced Materials* **2021**.

[11] B. S. Lammers, J. S. Siena, H. Mirhosseini, D. Yesilpinar, J. Heske, N. Lopez-Salas, T. D. Kühne, H. Fuchs, H. Mönig, "Real-space identification of non-noble single atomic catalytic sites within metal coordinated supramolecular networks", *submitted to ACS Nano* **2022**.

[12] J. Heske, S. K. Sahoo, M. Antonietti, T. D. Kühne, "Surprisingly high adsorption affinities of poly(heptazine imide) salts for helium induced by charge separation", *in preparation* **2022**.

[13] J. Heske, M. Antonietti, T. D. Kühne, "Water in nanopores with interacting walls: change of solvent properties and thermodynamics", *in preparation* **2022**.

[14] J. Heske, M. Antonietti, T. D. Kühne, “Competition between adsorbed water and helium inside nanopores of potassium pol(heptazine imide)”, *in preparation* **2022**.

[15] J. Heske, T. D. Kühne, E. Prodan, “Quantifying the liquid-solid transition of silicon via Voronoi tessellation analysis”, *in preparation* **2022**.

[16] J. Heske, J. Gujt, T. D. Kühne, “Importance of nuclear quantum effects on the structure of supercooled water around its liquid-liquid critical point”, *in preparation* **2022**.